Consortium

for

Small-Scale Modelling

Newsletter

April 2012 *No. 12*

Deutscher Wetterdienst

MeteoSwiss

Ufficio Generale Spacio Aero e Meteorologia

ΕΘΝΙΚΗ ΜΕΤΕΩΡΟΛΟΓΙΚΗ ΥΠΗΡΕΣΙΑ

Instytucie Meteorogii i Gospodarki Wodnej

Administratia Nationala de Meteorologie

Agenzia Regionale per la Protezione Ambientale dell Emilia Romagna Servizio Idro Meteo Clima

Federal Service for Hydrometeorology and Environmental Monitoring

Amt für GeoInformationswesen der Bundeswehr

Centro Italiano Ricerche Aerospaziali

Agenzia Regionale per la Protezione Ambientale dell Piemonte

www.cosmo-model.org

Editors: Ulrich Schättler (DWD); Cosmin Barbu (NMA)

Table of Contents

The current issue of the COSMO Newsletter presents results of a selection of many developments related to the activities of our consortium. The articles document not only the achievements of COSMO scientists in diverse areas of COSMO interests but also indicate a fruitful cooperation of the COSMO community with academic institutions. I am personally very pleased of it and I am convinced that such a cooperation and its strengthening will substantially assist in maintaining and reinforcing scientific quality of our research and, finally, the quality of our operational tools and software.

The year 2011 was especially important for our consortium. The COSMO General Meeting, which took place from 5 to 8 September in Rome, was the forum for presentations and discussions on the current work of the consortium; see the presentations at http://www.cosmo-model.org/content/consortium/generalMeetings/general2011/default.htm. During the meeting, the COSMO Standards for Source Code Development and the revised terms of reference for the main COSMO bodies like the Working Group Coordinators (WGCs), Source Code Administrators (SCA), Scientific Project Manager (SPM), as well as Scientific Management Committee (SMC) and Technical Advisory Group (TAG) were approved. The aim of the latter was to clarify the role and responsibilities of the COSMO bodies as well as to harmonize them with the approved coding standards.

The aim of the introduction of the coding standards is to assure the high quality of COSMO software, necessary for current development as well as future maintenance of the COSMO code. You can find the document at http://www.cosmo-model.org/content/model/documentation/standards/default.htm. As expressed by Marco Arpagaus, the former SPM, "Together with the COSMO Science Plan, the Priority Projects, Priority Tasks and Work Package Lists, the COSMO Standards for Source Code Development forms the main pillars of the COSMO development process". With these, we are all very much invited, encouraged and obliged to implement the high COSMO standards into practice. Good luck!

For the next General Meeting, we will meet in Lugano, Switzerland, from 10 to 13 September 2012.

Michał Ziemiański
COSMO Scientific Project Manager

Figure 1: Participants of the 13th COSMO General Meeting in Rome

Horizontal nonlinear Smagorinsky diffusion

M. Baldauf and G. Zängl

Deutscher Wetterdienst, Offenbach, Germany

1 Introduction

The COSMO model uses several diffusion and damping mechanisms to stabilize the dynamical core. One of these is an artificial 4th order hyper-diffusion acting in the horizontal direction. For example in the COSMO-DE (i.e. the COSMO model setup covering mainly Germany together with the most part of the Alpine region with a horizontal grid mesh size of 2.8 km) it is used to smooth the wind velocity components u, v, and w. The strength of the constant hyper-diffusion coefficient lies at about 5% of its possible maximum value (which is defined by the stability constraint). Only in a boundary zone it has a higher value and additionally the other dynamic variables pressure p' and temperature T' (i.e. their deviations from a reference state) are diffused.

In very rare events this artificial hyper-diffusion is not strong enough to prevent the model from a crash by horizontal shear instabilities. This shows that an additional, more physically based diffusion mechanism in the horizontal is needed.

2 Horizontal Smagorinsky Diffusion

The nonlinear diffusion proposed by Smagorinsky (1963) is formally a purely horizontally acting ('harmonic') diffusion. In Cartesian coordinates it may be written as

$$\frac{\partial u}{\partial t} + \vec{v} \cdot \nabla u = \ldots + K_{smag} \Delta u, \tag{1}$$

$$\frac{\partial v}{\partial t} + \vec{v} \cdot \nabla v = \ldots + K_{smag} \Delta v, \tag{2}$$

$$\frac{\partial w}{\partial t} + \vec{v} \cdot \nabla w = \ldots + 0, \tag{3}$$

with the diffusion coefficient

$$K_{smag} = l_s^2 \cdot \sqrt{T^2 + S^2}, \tag{4}$$

$$T = \frac{\partial u}{\partial x} - \frac{\partial v}{\partial y}, \tag{5}$$

$$S = \frac{\partial u}{\partial y} + \frac{\partial v}{\partial x}. \tag{6}$$

This means that K_{smag} contains both parts of the horizontal tension strain T and of the horizontal shearing strain S. Smagorinsky (1993) pointed out that on the sphere additional metric correction terms must be considered in T and S. But those can be neglected for smaller scale model applications and with the main intention to prevent from model crashes by shear instabilities.

The length scale l_s (a sort of a mixing length) can be determined by the following argument: in any case a stability criterion

$$K_{smag} \cdot \Delta t \left(\frac{1}{\Delta x^2} + \frac{1}{\Delta y^2} \right) \leq \frac{1}{2} \tag{7}$$

must be fulfilled. One can approximately set (motivated by numerical efficiency)

$$l_s^2 = \frac{c}{\frac{1}{\Delta x^2} + \frac{1}{\Delta y^2}} \tag{8}$$

with a yet arbitrary 'Smagorinsky-constant' c. Then from stability constraint it follows, that the *dimensionless* diffusion coefficient

$$k_{smag} := c \cdot \Delta t \cdot \sqrt{T^2 + S^2} \tag{9}$$

must fulfill

$$k_{smag} \leq \frac{1}{2}. \tag{10}$$

For example for COSMO-DE with $\Delta x \approx \Delta y \approx 2800$ m and $\Delta t \approx 25$ s and for a shear of $\Delta u = 28$ m/s per grid box this results in $k_{smag} \approx c \cdot \Delta t \cdot \Delta u / \Delta y \approx c \cdot 0.25$.
To get the dimensional value K_{smag} one has to multiply by $\left(\Delta t \cdot \left(\frac{1}{\Delta x^2} + \frac{1}{\Delta y^2} \right) \right)^{-1} \approx 1.6 \cdot 10^5 \ m^2/s$. Smagorinsky (1963) proposes a value of about $c \approx 0.1$. If one uses this diffusion only as a mechanism to reduce shear instabilities without influencing too much the overall model behavior, a value of $c \approx 0.03$ was found as appropriate for COSMO-DE simulations.

To discretize S and T by centered differences in a symmetric way, T is discretized to the scalar position (i, j) whereas S is discretized to the position $(i+1/2, j+1/2)$ ('uv'-position). Afterward they are firstly squared (to prevent from annihilation by negative values) and secondly they are averaged to the u- and v-positions. To avoid a double counting, i.e. that small wavelengths are diffused too strong by both Smagorinsky- and the 4th order (hyper)-diffusion, the dimensionless hyper-diffusion coefficient is subtracted with a weight of 0.5.

This horizontal Smagorinsky diffusion is implemented in the official version COSMO 4.21. There is only one namelist switch (`l_diff_Smag`) to enable or disable it. The two above mentioned parameters are only internal parameters (with the intention that only experienced users should modify them): the Smagorinsky constant `c_smag = 0.03` and the weighting to avoid double counting `weight_K_4th = 0.5`.

3 Case Study

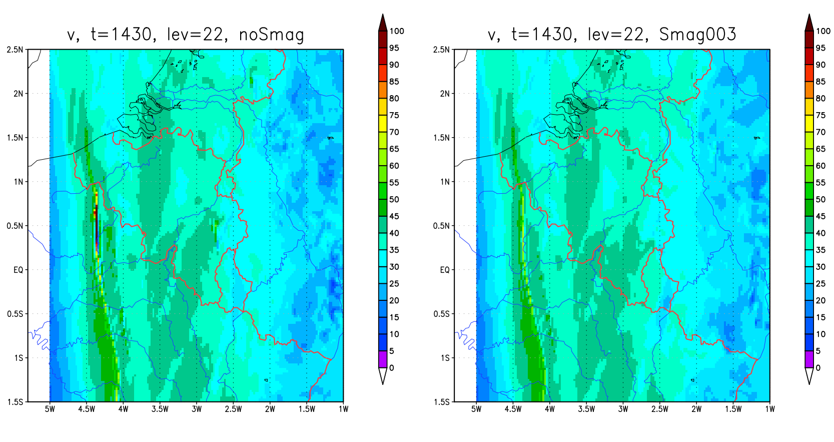

Figure 1: COSMO-DE simulation started at 26. Aug. 2011, 6 UTC: meridional component of wind velocity at level 22 at 20:30 UTC. Left: only linear horizontal hyper-diffusion, right: with additional Smagorinsky-diffusion.

An example which shows the necessity of a more physically based diffusion mechanism is the COSMO-DE at the 26. Aug. 2011. Here both the deterministic run and several runs of the DWD COSMO-DE ensemble prediction system crashed due to a shear instability which occurred in the vicinity of the westerly inflow boundary during the evening. The strong shear can be recognized in Fig. 1 (left) in the meridional wind component v. This strong shear occurred only in two levels but it was sufficient to cause a model abort shortly after this event due to CFL number violation. In contrast, in the simulation with Smagorinsky diffusion (Fig. 1, right) the wind shear is strongly reduced; consequently the model did not crash. Obviously, the Smagorinsky diffusion did not completely destroy the shear along the front. This is not unrealistic, e.g strong shear in the vicinity of so called 'narrow cold frontal rainbands' does occur in reality.

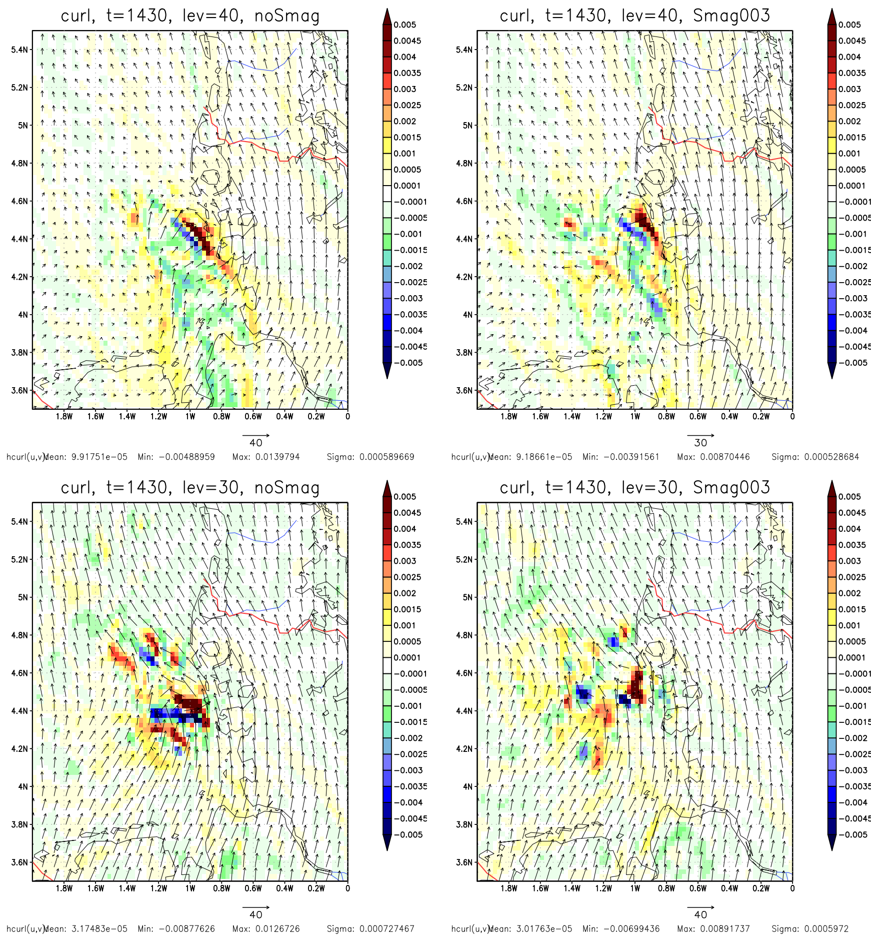

Figure 2: Simulation of 26. Aug. 2011, 6 UTC run, at 20:30 UTC: curl of the horizontal wind field (shaded) and wind velocity (arrows at every third grid position) at about $z \sim 900$ m (top row) and at about $z \sim 3.3$ km (bottom row) above ground. Only horizontal hyper-diffusion (left), and with additional Smagorinsky-diffusion (right).

At about the same time a mesocyclone occurred near the north western coast of Germany. This structure seemed to be realistic, therefore the Smagorinsky diffusion should not destroy such a phenomenon. This is demonstrated in Fig. 2: the runs with additional Smagorinsky diffusion (right) show the mesocyclone with about the same strength and position than the control run (left).

Fig. 3 displays the maximum and volume mean value of the dimensionless diffusion coefficient k_{smag}. The mean value $<k_{smag}> \approx 0.002$ corresponds to a mean value of about $<K_{smag}> \approx 300$ m^2/s.

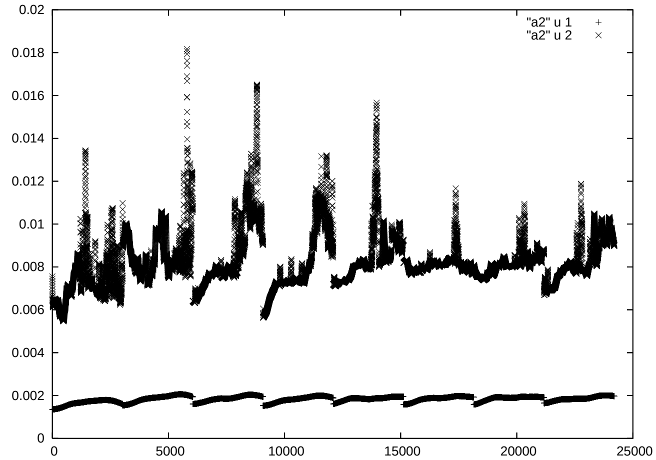

Figure 3: Temporal behavior of maximum (upper curve) and volume mean (lower curve) values of the dimensionless diffusion coefficient k_{smag} for the same simulation.

4 Summary and Outlook

The purpose of this implementation is the stabilization of the dynamical core (and the whole model) against horizontal shear instabilities. The reason for the occurrence of such effects is the lack of a horizontally acting turbulence scheme. The intention of this implementation was to keep the purely vertical turbulence scheme (mainly a Mellor-Yamada type, stage 2.5 scheme with some modifications) and to apply the Smagorinsky diffusion in addition to that. Therefore the 3-dimensional Smagorinsky-diffusion already implemented by Herzog et al. (2002a, 2002b) could not be used (see also the contribution of Langhans et al. (2012) in this COSMO-Newsletter). Moreover for such a stabilization purpose the emphasis lies more on efficiency than on physical accuracy. Therefore no metric terms of the terrain following coordinate were used. Such metric terms were derived for the fluxes and the flux divergence in Baldauf (2005) and can be used for the above mentioned 3D Smagorinsky diffusion (Baldauf, 2006) if the slope of the terrain is not too steep. Therefore, the additional computational costs are moderate with about 1% of the total run time (measured with COSMO-DE on 8 processors on the NEC SX9).

Until now only tests were made for the convection resolving model application COSMO-DE. The verification scores against synoptic observations and against upper air observations for two periods in winter (1.-28. Feb. 2011) and in summer (1.-30. Aug. 2011) were neutral compared to runs without the horizontal Smagorinsky diffusion. Despite this fact, a closer investigation of the influence of any horizontal diffusion to the initiation and development of resolved deep convection would be of interest. It should be further tested if this Smagorinsky diffusion should be applied for the larger-scale model applications, too (e.g. for COSMO-EU with 7 km horizontal grid mesh size).

References

[1] Baldauf, M., 2005: The Coordinate Transformations of the 3-dimensional Turbulent Diffusion in LMK. *COSMO-Newsletter*, No. **5**, 132-140.

[2] Baldauf, M., 2006: Implementation of the 3D-Turbulence Metric Terms in LMK. *COSMO-Newsletter*, No. **6**, 44-50.

[3] Herzog, H.-J., G. Vogel and U. Schubert, 2002: LLM - a nonhydrostatic model applied

to high-resolving simulations of turbulent fluxes over heterogeneous terrain *Theor. Appl. Climatol.*, **73**, 67-86.

[4] Herzog, H.-J., U. Schubert, G. Vogel, A. Fiedler, R. Kirchner, 2002: LLM - the High-Resolving Nonhydrostatic Simulation Model in the DWD - Project LITFASS (Part I: Modelling Technique and Simulation Method) *Technical Report*, No. **4**, Deutscher Wetterdienst, Offenbach, Germany.

[5] Langhans, W., J. Schmidli, and B. Szintai, 2012: A Smagorinsky-Lilly turbulence closure for COSMO-LES: Implementation and comparison to ARPS. *COSMO-Newsletter*, No. **12**

[6] Smagorinsky, J., 1963: General circulation experiments with the primitive equations. *Mon. Wea. Rev.*, **91/3**, 99-164

[7] Smagorinsky, J., 1993: Some historical remarks on the use of nonlinear viscosities, In 'Large Eddy Simulation of Complex Engineering and geophysical Flows'. *Cambridge University Press*, editors: B. Galperin and St. A. Orszag, 3-36.

Tests of TILES/MOSAIC parametrisation in COSMO model

GRZEGORZ DUNIEC[1], ANDRZEJ MAZUR[2]

1: Department for Numerical Weather Forecasts COSMO
2: Institute of Meteorology and Water Management
ul. Podleśna 61, 01 – 673, Warszawa, Polska

1 Summary

In COSMO model (Consortium for Small-Scale Modelling) physical processes occurring between lower atmosphere and upper soil layers were parameterized via soil model TERRA and TERRA/LM (Doms et al., 2007). Since 2009 at the Institute of Meteorology and Water Management (IMGW) two new parameterizations, MOSAIC and TILE, (Ament 2006, 2008 and Ament and Simmer, 2010, Duniec and Mazur 2011) have been tested. These parameterizations have taken into account non-homogeneities of the soil in a single grid. In 2009 and 2010 MOSAIC parameterization has been intensively tested (Duniec, Mazur, 2011), and tests were continued in 2011 with TILE parameterization. Tests were carried out using selected data from days with specific synoptic conditions. Different versions of the model code with both TILE and MOSAIC parameterizations implemented were used for tests, using various numerical and convection schemes.

2 Introduction

Physical processes occurring in the soil and the bottom layer of the atmosphere (in boundary layer of atmosphere), are interlinked. In soil, there is a set of hydrological and thermal processes (Warner, 2011):

- Capillary and gravitational transport of water, drainage of surface and subsurface runoff.
- Vertical transport of water vapor in the atmosphere via convection and molecular diffusion.
- Withdrawal of water in soil by plant roots (trees, grass, etc.).
- Freezing and melting and/or condensation and evaporation of water, release of absorbed latent heat due to these processes.
- Thermal conductivity.
- Precipitable water, water from melting snow, dew which penetrates into deeper layers of soil.
- Evaporation of water from the ground into the atmosphere.
- Heat exchanged between the ground and atmosphere.
- Transport of water in the roots, herbaceous, etc.
- Precipitation on the (covered or not covered - bare-soil) surface with vegetation.
- Drips of water on a surface or other plants.

- Snowfall and its excess on a soil surface covered with and on bare soil.
- Melting and sublimation of snow and frost and any accompanying thermal processes.
- Dew and frost on a soil covered or with vegetation or bare soil, release of latent heat.
- Surface mist (soil covered with vegetation and bare soil).
- Evaporation of water from the surface of the leaves of plants, transpiration, any accompanying thermal processes.

Many factors affects on thermal and hydrological processes in soil. These factors are related to:

a) soil type (clay, sand, silt, mud, sludge, etc., with different physical properties such as thermal conductivity, porosity, etc.),

b) soil cover (water, ice, snow),

c) type of vegetation covering a ground (grass, forest, etc.),

d) spatial distribution of vegetation coverage,

e) type of region (cities, villages, fields, meadows, etc.),

f) season (soil may be frozen, moist, dry, snow-covered etc. due to synoptic situation),

g) physical processes that occur in the lower atmosphere.

Since that these processes occur on a scale smaller than the resolution of model grid they must be parameterized. At present two parameterizations are applied in the COSMO model, namely soil and vegetation models TERRA and TERRA_LM (Doms et al., 2007), that assume that surface of the Earth in a single model grid is uniform. Since 2009 at IMGW two other parameterizations, TILE and MOSAIC, are tested. Both account for ground non-uniformity (Ament, 2006, 2008, Ament and Simmer, 2010, Duniec and Mazur 2011). Tests were carried out for several terms (selected dates). Selection was made on the basis of miscellaneous criteria, namely, season of a year, different conditions of soil - frozen, unfrozen, clamp, loose, etc.), synoptic situation (sunny, foggy, windy, cloudy day etc.), and atmospheric phenomena, (at ground surface, e.g. snow cover). In 2009 and 2010 tests of MOSAIC parameterization were conducted for six selected synoptic terms (Duniec, Mazur 2011) while in 2011 TILE and MOSAIC parameterizations were tested for nine (actually, six previously chosen and three additional) terms.

During tests various versions of model code model were used (4.08 and 4.14 with parameterizations MOSAIC and TILE implemented), with miscellaneous numeric and convection schemes. Approach MOSAIC and TILE is described in the work of (Ament 2006, 2008; see Ament and Simmer, 2011 and Duniec and Mazur 2011).
Following meteorological fields were selected for tests:

- TE2M - air temperature at 2m above ground level.
- TD2M - dew point temperature at 2m agl.
- TSOI - soil temperature at 0 cm.

- U10m - zonal wind component, 10m agl.
- V10m - meridional wind component, 10m agl.
- QV2M- specific water vapor content, 2m agl.
- QVSF - specific water vapor content at surface.
- PR - atmospheric pressure.

Data from nine terms with various soil- and synoptic conditions were selected for analysis, as follows: 01.02.2009, 00 UTC, 22.04.2009, 12 UTC, 22.07.2009, 00 UTC, 16.10.2009, 00 UTC and 06 UTC, 04.11.2009, 12 UTC, 21.11.2009, 06 UTC, 10.01.2010, 00 UTC, 25.02.2010, 00 UTC and 18.11.2010, 00 UTC.

Description of synoptic conditions in 01.02.2009, 22.04.2009, 16.10.2009, 04.11.2009 and 21.11.2009 one can find in (Duniec and Mazur 2011).

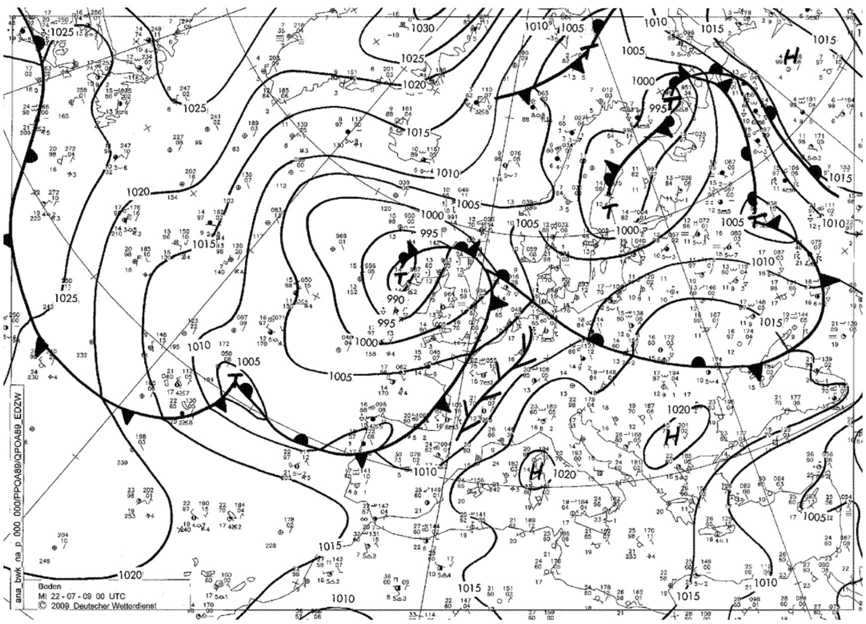

http://www.wetter3.de/fax

Figure 1: Synoptic situation of 22.07.2009, 00 UTC.

Meteorological conditions in 22.07.2009, 00:00 UTC (Fig. 1).
Weather in Western and Central Europe was influenced by fronts related to set of low-pressure centers. Southern Europe was in range of a high pressure center of 1020 hPa over Greece and Sardinia. South of Poland was up under an influence of a warm front associated with the atmospheric low-pressure center of 990 hPa over Ireland. Air temperature from 10.2 C to 20.8C. Wind form 0 to 10m/s over Baltic Sea in over western part of Sudety Mountains.

Meteorological conditions in 10.01.2010, 00:00 UTC (Fig. 2).
Northern Europe was in range of wide high-pressure center of 1040 hPa over southern Scandinavia. Western Europe was under an influence of high-pressure center of 1020 hPa over the Iberian Peninsula. The rest of Europe was in the range of low-pressure centers and atmospheric fronts. Southern Poland was in range of a warm front associated with the low-pressure

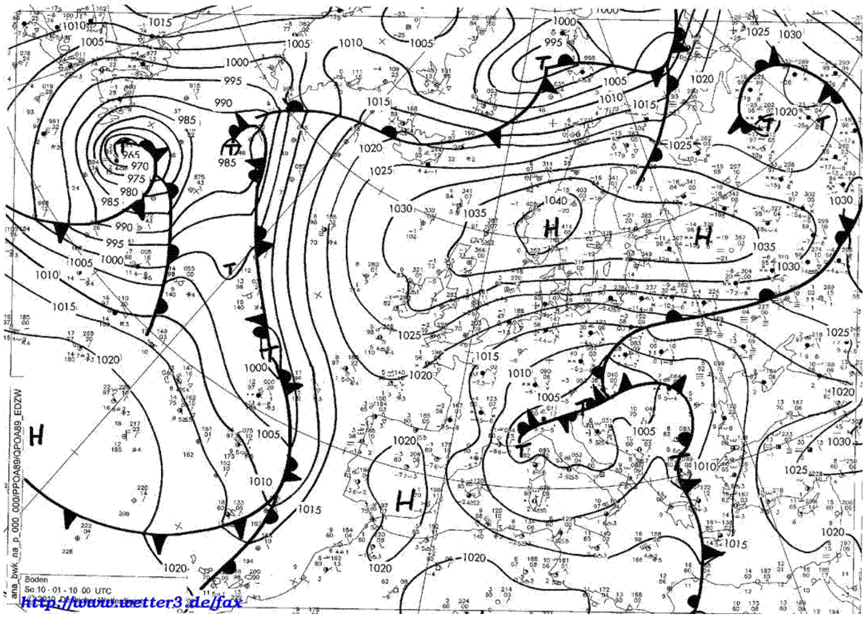

Figure 2: Synoptic situation of 10.01.2010, 00 UTC.

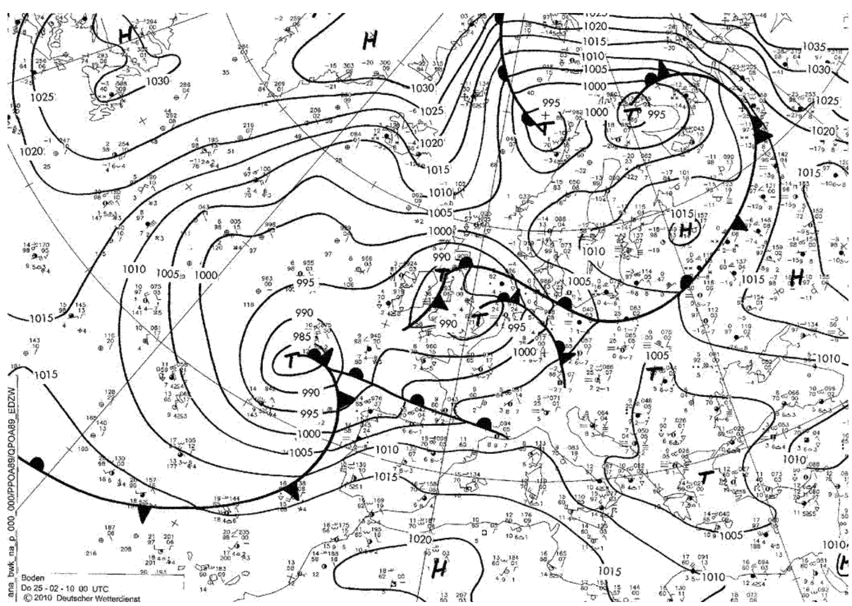

Figure 3: Synoptic situation of 25.02.2010, 00 UTC.

center of 1005 hPa over southern Europe. Wind from 1 m/s (midlands) to 21 m/s over Baltic Sea. Air temperature from -9.2C (north) to 1.9C in south.

Meteorological conditions in 25.02.2010, 00:00 UTC (Fig. 3).
In Western and Central Europe dominated systems of low pressure with atmospheric fronts. Poland was in the zone of warm atmospheric front associated with low-pressure center of 995 hPa over northern Scandinavia. Wind: weak all over the country. Air temperature from approximately -4.0C in mountain region of Poland to 3.5C.

Meteorological conditions in 18.11.2010, 00:00 UTC (Fig. 4).
Low-pressure center of 980 hPa over Ireland prevailed in Western Europe, and an atmospheric

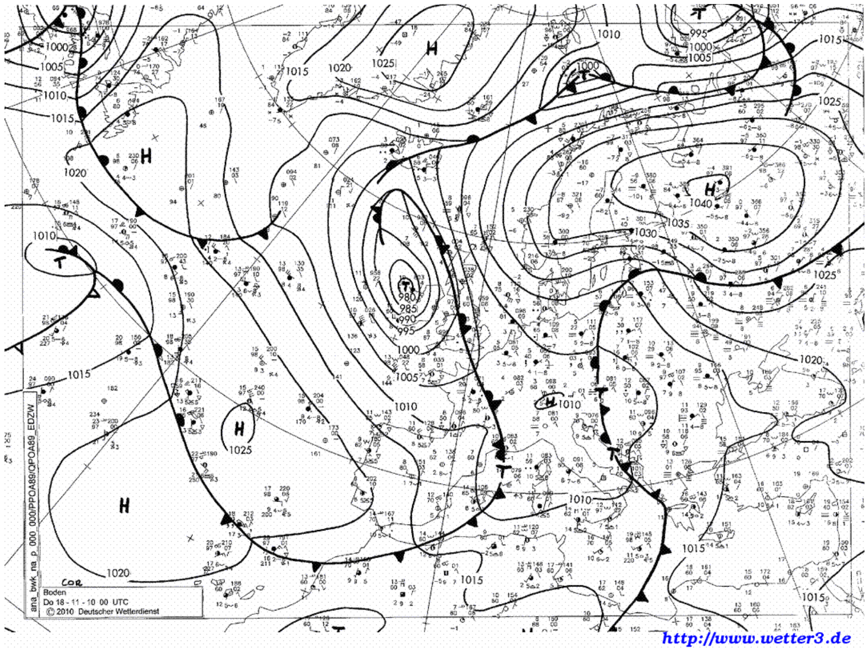

Figure 4: Synoptic situation of 18.11.2010, 00 UTC.

front in Central Europe. In the north-eastern part of Europe occurred high-pressure system with a center of 1040 hPa over the northern Russia. Poland was in the zone of warm front. Wind from 1 m/s to 11 m/s over the Baltic Sea. Air temperature from 3.0C to 9.0C.

3 Methodology

Several versions of COSMO model code were prepared and tested as follows:

- 4.08 - fundamental version of code, COSMO v. 4.08 - MOSAIC parameterization NOT implemented.

- 4.14 - fundamental version of code, COSMO v. 4.14 - TILE parameterization NOT implemented.

- MOSA - code of COSMO ver. 4.08 - with MOSAIC parameterization implemented.

- TILE - code of COSMO ver. 4.14 - with TILE parameterization implemented.

- NSUBS - modified code, TILE parameterization implemented but switched-off.

- SUBS1 - modified code, TILE parameterization implemented, accounting for presence/absence of snow cover in a single grid

- SUBS3 - modified code, TILE parameterization implemented, accounting for presence/absence (more or less 50% of) lake surface

- Three convections schemes were applied for every version as above:

- KAFR - Kain-Fritsch's scheme.

- SHAL - Tiedtke's scheme for shallow convection.

- TIED - regular Tiedtke's scheme.

. . . together with four numerical schemes (Doms et al., 2007):

- HEVI - leapfrog, 3-timelevel HE-VI integration.
- LFSI - leapfrog, 3-timelevel semi-implicit.
- RKN1 - Runge-Kutta, 2-timelevel HE-VI integration, irunge kutta=1.
- RKN2 - Runge-Kutta, 2-timelevel HE-VI integration, irunge kutta=2.

Numerical experiments were carried out for every chosen term using code versions prepared as described above. First, a comparative analysis was performed on three different ways:

1. To compare results obtained for the different versions of the code model COSMO for the same numerical and convection schemes as follows: 4.08 - 4.14, 4.08 - MOSA, 4.08 - TILE (NSUB, SUB1, SUB3), 4.14 -MOSA, 4.14 - TILE (NSUB, SUB1, SUB3), MOSA - TILE (NSUB, SUB1, SUB3), TILE (NSUB - SUB1, NSUB - SUB3, SUB1 - SUB3).
2. To compare results obtained using various numerical schemes but with fixed convection scheme for each version of the model code (e.g. MOSA, convection scheme Tiedtke, different numerical schemes).
3. To compare results obtained using different convection schemes but with fixed numerical scheme for each version of the model code (e.g. MOSA, numerical scheme Runge-Kutta, different convection schemes).

Afterwards correlation coefficient and standard deviation were calculated and analyzed for all possible combinations of numerical and of convection schemes.

4 Results and discussion

The results were divided into two categories, "the best configuration" and "the worst configuration". The first one contained results for which resulting correlation coefficient has the highest value, while the second - lowest value. The highest value of the correlation coefficient indicated that the parameterization either insignificantly or not at all influenced on examined meteorological field, and the smallest value of correlation coefficient suggests a high sensitivity of meteorological field to soil processes parameterization. It should be stressed out that terms "the worst" and "the best" did not reflect in any way a quality of parameterization, but described in a qualitative manner changes (from the most significant to the less ones) which can be seen comparing to reference runs.

The worst results were received from experiment code v. 4.08, 4.14, MOSA, TILE VIEW (SUB1, NSUB, SUB3) of 18 November 2010 for the following combinations: 4.14 - TILE (SUB1), 4.14 - TILE (NSUB), 4.08 - TILE (SUB1), 4.08 - TILE (NSUB), TILE (NSUB) - TILE (SUB3), TILE (NSUB) - TILE (SUB3), TILE (SUB1) -TILE (SUB3), MOSA - TILE (SUB1), MOSA - TILE (NSUB) (Tab. 1, Fig. 5-7).

The best results have been received for numerical experiment using the code v. 4.08 and the MOSA version for February 1, 2009 and 18 November 2010, for all analyzed meteorological fields, and for February 1, 2009 using the TILE version with NSUB and with SUB1. Correlation coefficient was equal to 1 for all convection schemes. It suggests that meteorological fields are insensitive to soil processes parameterization regardless of numerical and of convection schemes applied.

Numerical schemes →	HEVI	LFSI	RKN1	RKN2
Convection schemes ↓	**Comparison of 4.14-TILE-SUB1**			
KAFR	0,9278	0,9300	0,9317	0,9316
SHAL	0,9277	0,9302	0,9315	0,9316
TIED	0,9276	0,9290	0,9312	0,9312
	Comparison of 4.14-TILE-SUB			
KAFR	0,9278	0,9300	0,9317	0,9316
SHAL	0,9277	0,9302	0,9315	0,9316
TIED	0,9276	0,9290	0,9312	0,9312
	Comparison of 4.08-TILE-SUB1			
KAFR	0,9280	0,9302	0,9326	0,9325
SHAL	0,9279	0,904	0,9326	0,9326
TIED	0,9278	0,9294	0,9330	0,9330
	Comparison of 4.08-TILE-SUB			
KAFR	0,9820	0,9302	0,9326	0,9325
SHAL	0,9279	0,9304	0,9326	0,9326
TIED	0,9278	0,9294	0,9330	0,9329
	Comparison of TILE-NSUB-TILE-SUB3			
KAFR	0,9322	0,9341	0,9318	0,9318
SHAL	0,9321	0,9343	0,9317	0,9317
TIED	0,9318	0,9334	0,9314	0,9314
	Comparison of TILE-SUB1-TILE-SUB3			
KAFR	0,9322	0,9341	0,9318	0,9318
SHAL	0,9321	0,9343	0,9317	0,9317
TIED	0,9318	0,9334	0,9314	0,9314
	Comparison of MOSA-TILE-SUB1			
KAFR	0,9280	0,9302	0,9326	0,9325
SHAL	0,9279	0,9304	0,9326	0,9326
TIED	0,9278	0,9294	0,9330	0,9329
	Comparison of MOSA-TILE-NSUB			
KAFR	0,9280	0,9302	0,9326	0,9325
SHAL	0,9279	0,9304	0,9326	0,9326
TIED	0,9278	0,9294	0,9330	0,9329

Table 1: Correlation coefficient (soil temperature, 18.11.2010) for different model versions, convection and numerical schemes.

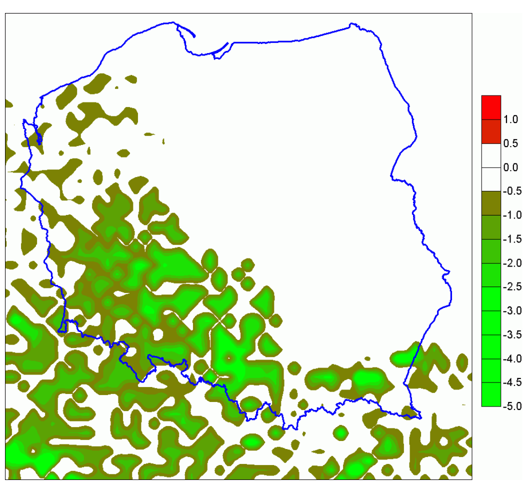

Figure 5: Differences of values of soil temperature at 2m agl., 18.11.2010 r. Comparison between 4.14 - TILE (SUB1), numerical scheme HE-VI, convection scheme Kain-Fritsch.

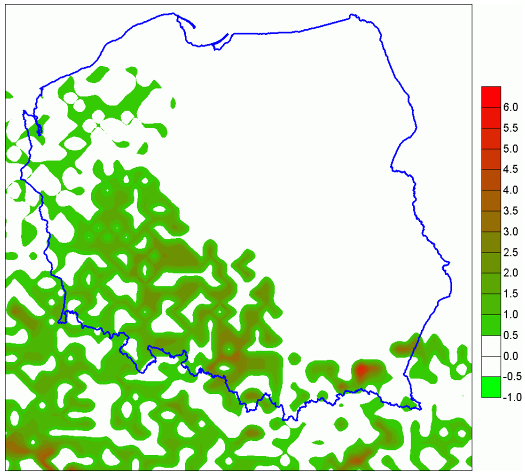

Figure 6: As in Fig. 5. Comparison between TILE SUB1 and SUB3, numerical scheme Runge-Kutta, convection scheme Tiedtke - shallow convection.

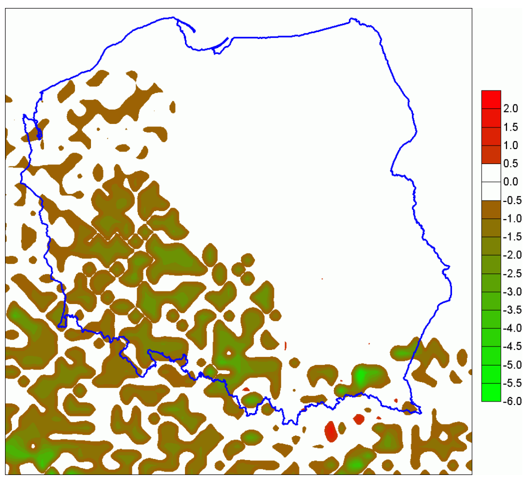

Figure 7: As in Fig. 5. Comparison between MOSA - TILE NSUB, numerical scheme Runge-Kutta 2, convection scheme Tiedtke.

The analysis of data shows that surface temperature is the most sensitive of meteorological field to MOSAIC and/or TILE parameterization (see tables 1-8). Correlation coefficients for this field are the lowest in comparison with correlation coefficients for others. It seemed that synoptic situation of 18.11.2010 was a main reason of it. During this day the entire area of Poland was under an influence of a warm front, which was accompanied by rainfall causing high amount of moist in a surface layer of soil and, subsequently, changes in physical properties of soil (e.g. thermal conductivity). It has caused soil surface temperature to be very sensitive to applied parameterizations. The change of physical properties of soil affected also on heat and moisture fluxes from soil surface to atmosphere and - indirectly -on other meteorological fields such as air temperature, dew point temperature and humidity. A sensitivity of these fields on the parameterizations of soil processes is smaller compared to sensitivity of soil surface temperature. Changing numerical and convection schemes one could not significantly affect results - differences in values of correlation coefficients was in the range of 0.01 to 0.06.

A sensitivity of meteorological fields for MOSAIC and/or TILE parameterization depends on a synoptic situation that affects current weather conditions. When in a given area there are homogeneous synoptic conditions meteorological fields are more sensitive to MOSAIC parameterization with numeric schemes leapfrog and leapsemi. This sensitivity was not observed for Runge-Kutta schemes, regardless of the applied schema types. When there is non-homogeneous set of meteorological conditions it was not stated explicitly which parameterization has a more significant influence on meteorological fields.

In Figures 8-10 and in tables 2 and 3 there are values of correlation coefficients of results obtained for the numerical experiment of 1 February 2009. On that date there were significantly different meteorological conditions. Poland was under the influence of high-pressure with center over mid Russia. There were no precipitation at all and ground surface was covered with snow. Using numeric schemes leapfrog and leapsemi, air temperature at 2m agl. seemed to be the most sensitive to soil parameterizations (to a lesser extent, dew point, sensible heat flux and humidity).

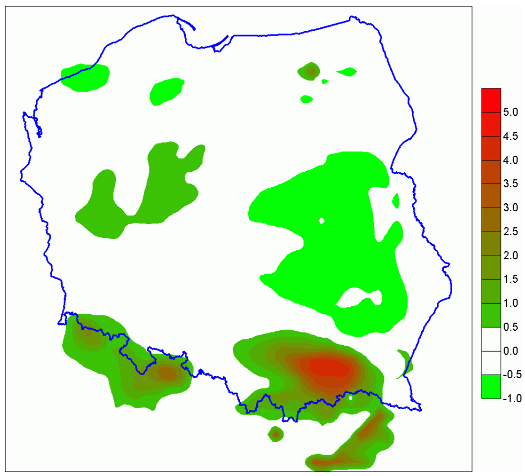

Figure 8: Differences of values of air temperature at 2m agl., 01.02.2009. Comparison between 4.14 - TILE (SUB3), numerical scheme HE-VI, convection scheme Kain - Fritsch.

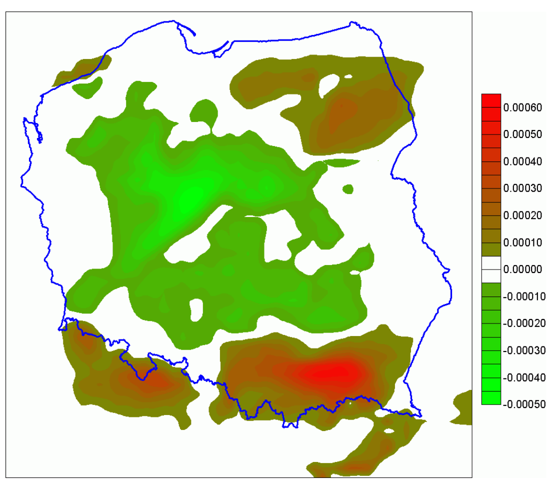

Figure 9: Differences of values of specific water vapor content at 2m agl., 01.02.2009. Comparison between 4.08 - TILE (SUB1), numerical scheme HE-VI, convection scheme Kain - Fritsch.

Numerical schemes →	HEVI	LFSI	RKN1	RKN2
Convection schemes ↓	Comparison of 4.14-TILE-SUB3			
KAFR	0,9696	0,9708	0,9954	0,9954
SHAL	0,9699	0,9708	0,9954	0,9954
TIED	0,9711	0,9711	0,9972	0,9972
	Comparison of 4.14-TILE-SUB1			
KAFR	0,9677	0,9686	0,9986	0,9985
SHAL	0,9683	0,9688	0,9985	0,9985
TIED	0,9679	0,9673	0,9986	0,9986
	Comparison of 4.14-TILE-NSUB			
KAFR	0,9677	0,9686	0,9986	0,9985
SHAL	0,9683	0,9688	0,9985	0,9985
TIED	0,9679	0,9673	0,9986	0,9986
	Comparison of 4.08-TILE-SUB3			
KAFR	0,9695	0,9704	0,9939	0,9939
SHAL	0,9697	0,9706	0,9939	0,9939
TIED	0,9710	0,9710	0,9942	0,9943
	Comparison of 4.08-TILE-SUB1			
KAFR	0,9676	0,9684	0,9970	0,9970
SHAL	0,9682	0,9688	0,9970	0,9970
TIED	0,9679	0,9636	0,9960	0,9960
	Comparison of 4.08 - TILE-NSUB			
KAFR	0,9676	0,9684	0,9970	0,9970
SHAL	0,9682	0,9688	0,9970	0,9970
TIED	0,9679	0,9674	0,9960	0,9960
	Comparison of TILE-NSUB - TILE-SUB3			
KAFR	0,9800	0,9765	0,9949	0,9949
SHAL	0,9802	0,9774	0,9949	0,9949
TIED	0,9820	0,9786	0,9965	0,9965
	Comparison of MOSAIC - TILE-SUB3			
KAFR	0,9695	0,9704	0,9939	0,9939
SHAL	0,9697	0,9706	0,9939	0,9939
TIED	0,9710	0,9710	0,9942	0,9943
	Comparison of MOSAIC - TILE-SUB1			
KAFR	0,9676	0,9684	0,9970	0,9970
SHAL	0,9682	0,9688	0,9970	0,9970
TIED	0,9679	0,9674	0,9960	0,9960

Table 2: Correlation coefficient (air temperature, 01.02.2009) for different model versions, convection and numerical schemes.

Numerical schemes →	HEVI-LFSI	HEVI-RKN1	HEVI-RKN2	LFSI-RKN1	LFSI-RKN2	RKN1-RKN2
Convection schemes/fields ↓	Comparison of TILE-NSUB					
KAFR-QV2M	0,9872	0,9713	0,9714	0,9782	0,9782	0,9999
KAFR-TE2M	0,9830	0,9655	0,9655	0,9579	0,9579	0,9999
SHAL-TE2M	0,9845	0,9660	0,9660	0,9578	0,9578	0,9999
TIED-TE2M	0,9823	0,9651	0,9655	0,9658	0,9658	0,9999
	Comparison of TILE-SUB1					
KAFR-QV2M	0,9872	0,9713	0,9714	0,9782	0,9782	0,9999
KAFR-TE2M	0,9830	0,9655	0,9655	0,9579	0,9579	0,9999
SHAL-TE2M	0,9845	0,9660	0,9661	0,9578	0,9578	0,9999
TIED-TE2M	0,9823	0,9655	0,9655	0,9658	0,9658	0,9999

Table 3: Correlation coefficient (for selected meteorological fields in 01.02.2009) TILE version, NSUB and SUB1), for selected convection and numerical schemes.

5 Conclusions

In this article results of tests carried out using a new soil processes parameterizations - MOSAIC and TILE in COSMO model COSMO are presented. Tests were carried out with different convection and numerical schemes to assess how parameterization(s) contributes to a forecast of meteorological fields or which one of them exhibits stronger influence. Statistical analysis was carried out and an analysis of the differences between the results obtained with parameterizations MOSAIC or TILE switched on and off. Results were divided into two groups. The first group includes results with the highest correlation coefficient (so called "the best case"), and the other - results with lowest correlation coefficient ("the worst case"). Best case suggests that the parameterization MOSAIC or TILE does not affect (almost at all) the forecast. The "worst case" is an opposite situation, describing strong influence of parameterization an forecast.

The analysis shows that: (a) synoptic situation that determines a weather in a given area, is also a main factor determining an influence of parameterization of soil processes on meteorological field(s). The manner of this influence would be a topic of on-going tests at IMGW; (b) MOSAIC parameterization has a more significant influence on meteorological fields in the case of homogeneous meteorological conditions prevailing in the area of interest and (c) in the case of "heterogeneous" weather, resulting in a diversification of physical characteristics of the soil - such as variations in the coverage of the snow surface of the soil - one cannot explicitly specify a schema for parameterization of the processes of soil that would have more significant influence on a meteorological field. At the moment detailed work on this issue is in progress.

References

[1] Ament, F., 2006: Energy and moisture exchange processes over heterogeneous land - surfaces in a weather prediction model. *PhD thesis*

[4] Doms, G. and U. Schattler, 2002: A Description of the Nonhydrostatic Regional Model LM, *Part I: Dynamics and Numerics*, DWD.

[3] Doms, G., and J. Forstner, E. Heise, H. - J. Herzog, M. Raschendorfer, T. Reinhardt, B. Ritter, R. Schrodin, J. - P.Schulz, G. Vogel, 2007: A Description of the Nonhydrostatic Regional Model LM, *Part II: Physical Parameterization*, DWD.

[4] Schattler, U. and G. Doms, C. Schraff, 2009: A Description of the Nonhydrostatic Regional Model LM, *Part VII: User's Guide*, DWD.

[5] Ament, F. and C Simmer, 2010: Improved Representation of Land - Surface Heterogeneity in a Non - Hydrostatic Numerical Weather Prediction Model (personal communication).

[6] Ament, F., 2008: COSMO_SUBS. MeteoSwiss.

[7] Stensrud, D. J., 2007: Parameterization Schemes - Keys to Understanding Numerical Weather Prediction Models. *Cambridge University Press.*

[8] Cotton, W. R. and R. A. Anthes, 1989: Storm and Cloud Dynamics. *Academic Press*, INC.

[9] Smith, R. K., 1997: The Physics and Parameterization of Moist Atmospheric Convection. *Kluwer Academic Publishers.*

[10] Louis, J. F. , 1979: A parameterizartion model of vertical eddy fluxes in the atmosphere. *Boundary Layer Meteorol.* 17. **187 - 202**.

[11] Tiedtke, M., 1989: A comprehensive mass flux scheme for cumulus parameterization in large scale model. *Mon. Wea. Rev.*, pp. **1779 - 1800**.

[12] Jacobson, M. Z., 2000: Fundamentals of Atmosferic Modeling. *Cambridge University Press.*

[13] www.wetter3.de/fax - synoptic maps.

[14] Mellor, G. and T. Hamada, 1982: Development of a turbulence closure model for geophysical fluid problem. *Rev. Geophys. and Space Phys.*, 20, **851 - 875**.

[15] Mellor, G. and T. Hamada, 1974: A hierarchy of turbulence closure models for planetary boundary layers. *J. Atm. and Space Phys.*, 31, **1791 - 1806**.

[16] Rewut, I. B., 1980: Soil physics (in Polish: Fizyka gleby), PWRiL.

[17] Duniec, G. and A. Mazur, 2011: COLOBOC - MOSAIC parameterization in COSMO model v. 4.8. *COSMO Newsletter*, no. 11, **69 - 81**.

[18] Warner, T. T., 2011: Numerical Weather and Climate Prediction. *Cambridge University Press.*

A Smagorinsky-Lilly turbulence closure for COSMO-LES: Implementation and comparison to ARPS

Wolfgang Langhans[1], Jürg Schmidli[1], and Balazs Szintai[2*]

[1] *Institute for Atmospheric and Climate Science, ETH Zurich, Switzerland*

[2] *Federal Office of Meteorology and Climatology MeteoSwiss, Switzerland*

1 Introduction

Large-eddy simulations (LES) are a powerful tool to study atmospheric turbulence such as found in the convective boundary layer (CBL) or in shear-driven flows. LES turbulence closures have commonly been used also in the cloud-modeling community for kilometer-scale simulations of deep convection (e.g., Klemp and Wilhelmson 1978) and therefore attract an even broader range of scientific researchers. In this work a Smagorinsky-Lilly turbulence model is implemented into COSMO and tested for the neutral and the convective boundary layer. For wall-bounded neutral flows the Smagorinsky-Lilly model performs less accurately (Chow et al. 2005; Pope 2000) compared to more sophisticated RANS closures (e.g., elliptic relaxation models), but its computational efficiency and simplicity is of great advantage (Chow et al. 2005).

The implementation into the COSMO code, which has not been originally designed for LES, is described here. Thereafter, the implementation is tested for idealized neutral (NBL) and convective boundary layer (CBL) flows. Our simulations are compared to the ARPS model (see Xue et al. 2000). The latter has frequently been applied in LES studies (e.g., Chow et al. 2005).

2 Implementation

2.1 Smagorinsky-Lilly turbulence model

The Smagorinsky mixing-length model has been designed to simulate the energy transfer from resolved to unresolved scales across an inertial subrange of locally isotropic three-dimensional turbulence. The resolved motions are separated from residual motions by implicit filtering of the governing equations in space. The residual stress-tensor is defined by a linear eddy viscosity model as

$$\overline{u_i u_j} = \underbrace{-2K_M D_{ij}}_{deviatoric} + \underbrace{\frac{2}{3} e \delta_{ij}}_{isotropic} \qquad D_{ij} = \frac{1}{2}\left(\frac{\partial U_i}{\partial x_j} + \frac{\partial U_j}{\partial x_i}\right) \tag{1}$$

with an eddy viscosity K_M and the filtered (grid-scale) rate of strain D_{ij}. The isotropic part of the stress-tensor related to the subgrid turbulent kinetic energy e is typically small and therefore neglected[1]. Smagorinsky's (1963) original proposal has been adapted by Lilly (1962) to include the effects of buoyancy, such that the eddy viscosity is given as

$$K_M = (c_s l_s)^2 \overline{D} \sqrt{\max\left(0, 1 - \frac{\mathrm{Ri}}{\mathrm{Ri}_c}\right)} \tag{2}$$

*Current affiliation: Hungarian Meteorological Service
[1] This assumption is also applied in other NWP models such as, e.g., ARPS, WRF, or CM1.

with the characteristic filtered rate of strain $\overline{D} = (2D_{ij}D_{ij})^{1/2}$, the Smagorinsky length scale l_s given by Deardorff's proposal as $l_s = (\Delta x \Delta y \Delta z)^{1/3}$, the Smagorinsky constant c_s, a critical Richardson number Ri_c, and a (deformation) Richardson number

$$Ri = \begin{cases} N_m^2/\overline{D}^2 & \text{for saturated air} \\ N^2/\overline{D}^2 & \text{for unsaturated air.} \end{cases} \tag{3}$$

The moist static stability N_m is defined following Durran and Klemp (1982). An option for anisotropic mixing in vertical and horizontal directions has also been implemented. Thereby, two mixing lengths are computed as

$$l_h = (\Delta x \Delta y)^{1/2} \qquad l_v = \Delta z \tag{4}$$

and substituted into Eq. (2) to obtain the corresponding eddy viscosities K_M^h and K_M^v.

The characteristic rate of strain can be rewritten as

$$\overline{D}^2 = 2\{D_{11}^2 + D_{22}^2 + D_{33}^2\} + 4\{D_{12}^2 + D_{13}^2 + D_{23}^2\} \tag{5}$$

and the surface stresses are parameterized using the drag laws

$$\overline{uw}_{surf} = -c_D \rho_{surf} \tilde{u} \sqrt{\tilde{u}^2 + \tilde{v}^2} \quad \text{and} \quad \overline{vw}_{surf} = -c_D \rho_{surf} \tilde{v} \sqrt{\tilde{u}^2 + \tilde{v}^2} \tag{6}$$

with the density at the surface ρ_{surf} and tilde indicating parameters on the lowest model level. This shear stress parameterization using horizontal wind speed appears plausible for flows over weakly sloping surfaces, but for steep slopes the shear stress might be better approximated by the slope parallel wind component.

2.2 Numerical implementation

The deformation tensor is computed in `src_slow_tendencies_rk.f90`. Both normal components and vertical shear components are located at mass-points, while D_{12} is computed at the center of each grid-box's corner (see Fig. 1). Then the eddy viscosities for horizontal fluxes are computed at mass-points from Eq. (2) in `src_turbulence.f90`. For isotropic turbulence an interpolation yields the eddy viscosities for vertical mixing located on half-levels. Optionally, e may be diagnosed from the trace of the deformation tensor.

An implicit discretization is used to calculate (most of) the tendencies. This method is also used for the discretization of the vertical flux divergences in the current operational models, e.g., COSMO-2. However, since the implicit solver was implemented along with a 1D turbulence scheme, the Reynolds-stress divergence is incomplete. In more detail, the mixing tendencies M_u^{TD} and M_v^{TD} appearing in the u- and v-equations, respectively, are simplified by the homogeneous boundary layer approximation, as

$$\begin{aligned} M_u^{TD} &= \ldots - \frac{1}{\rho}\frac{\partial}{\partial z}\tau_{13} = \ldots - \frac{1}{\rho}\frac{\partial}{\partial z}(-\rho 2K_m^v D_{13}) = \ldots - \frac{1}{\rho}\frac{\partial}{\partial z}(-\rho K_m^v(\frac{\partial w}{\partial x} + \frac{\partial u}{\partial z})) \\ &\approx \ldots - \frac{1}{\rho}\frac{\partial}{\partial z}(-\rho K_m^v \frac{\partial u}{\partial z}) \\ M_v^{TD} &= \ldots - \frac{1}{\rho}\frac{\partial}{\partial z}\tau_{23} = \ldots - \frac{1}{\rho}\frac{\partial}{\partial z}(-\rho 2K_m^v D_{23}) = \ldots - \frac{1}{\rho}\frac{\partial}{\partial z}(-\rho K_m^v(\frac{\partial w}{\partial y} + \frac{\partial v}{\partial z})) \\ &\approx \ldots - \frac{1}{\rho}\frac{\partial}{\partial z}(-\rho K_m^v \frac{\partial v}{\partial z}). \end{aligned}$$

Thus, together with the horizontal flux convergences also the missing parts from these tendencies are computed explicitly in `explicit_horizontal_diffusion.f90`. The Reynolds-stresses related to explicit vertical diffusion, given as

$$\tau_{13expl} = -\rho K_m^v \frac{\partial w}{\partial x} \quad \text{and} \quad \tau_{23expl} = -\rho K_m^v \frac{\partial w}{\partial y},$$

are located above the u and v points, respectively, on the model half-levels (see Fig. 1). This splitting of the tendencies into implicit and explicit contributions is problematic at the lowest model level, as the parameterized surface Reynolds-stresses (see above) can not be split. Thus, a zero-gradient lower boundary condition is assumed for the explicit parts of the Reynolds-stresses on the lowest level, such that vertical mixing of u and v results only from the implicit contribution. For all derivatives (deformation, scalar fluxes, flux divergences) metric correction terms may optionally be computed, such that horizontal diffusion can be evaluated in physical space also for sloping model levels.

To ensure numerical stability the horizontal diffusion coefficients are limited by a maximum non-dimensional value of 0.1. This limiter is also applied to the vertical diffusion coefficients used for explicit vertical mixing, but not for the implicit vertical mixing. This threshold is commonly used in mesoscale models (e.g., WRF) and chosen slightly more stringent than the one resulting from linear analysis.

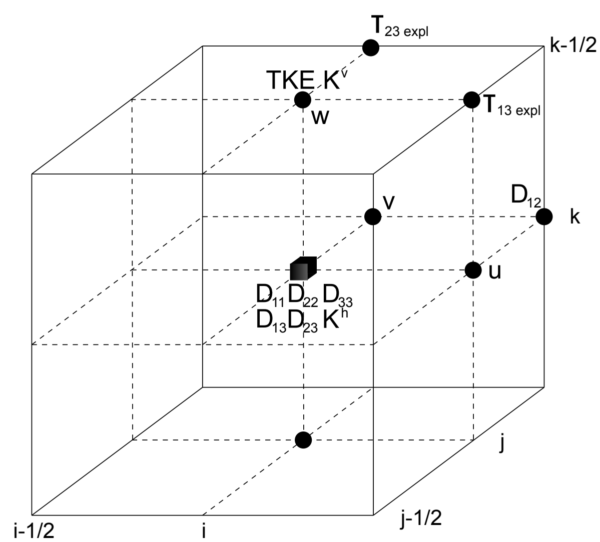

Figure 1: Illustration of the staggering of variables involved within the computation of 3D flux convergences. The mass-point in a grid-box center is indicated by the cube.

3 Simulation of the neutral PBL

The neutral PBL has been intensively studied in the literature (e.g., Andren et al. 1994, Chow et al. 2005, Mirocha et al. 2010). For this type of flow the turbulent scales close to the surface are challengingly small. The forcing is a geostrophic wind in longitudinal-direction driven by a corresponding pressure-gradient. The result for a semi-slip lower boundary condition is a logarithmic wind profile in the surface layer (10-20 % of PBL depth). For a constant eddy viscosity ($K_m^v \neq K_m^v(z)$) the analytical solution of the wind profiles is given by an Ekman-spiral (Stull 1988, pp. 210). The Smagorinsky model is known to over-predict the near-surface stress owing to an under-resolved flow and missing backscatter from the subgrid-scale (Mason and Thompson 1992).

3.1 Model setup

The split-explicit 3rd-order Runge-Kutta time-discretization with explicit 5th-order advection in the horizontal direction and 2nd-order implicit vertical advection is utilized for these simulations. No explicit computational diffusion has been applied. The timestep is 0.125 s, which gives a maximum initial advective Courant number of roughly 0.15. The domain spans $1280 \times 1280 \times 1500$ meters with double periodic lateral boundary conditions. The grid-spacing is $\Delta x = 10$ m in the horizontal directions, while a stretched grid is used in the vertical with a minimum $\Delta z_{min} = 10$ m at the surface and a maximum $\Delta z_{max} = 65$ m at the top. The stretching is given by

$$\Delta z_i = \Delta z_m + \frac{\Delta z_{min} - \Delta z_m}{\tanh(2)} \tanh\{\frac{2}{1-a}(i-a)\} \quad \text{for } i = 1, ke \tag{7}$$

with $\Delta z_m = 0.5(\Delta z_{min} + \Delta z_{max})$, $a = 0.5(1 + ke)$, and $ke = 40$. The total number of nodes is $129 \times 129 \times 41$[2]. A free-slip boundary condition ($\tau_{ij} = 0,\ w = 0$) is applied at the top and the standard dynamic bottom boundary condition is used. The transfer coefficient of momentum c_D is given for a neutral PBL as $c_D = \kappa^2 \ln\{(z_0 + 0.5\Delta z_{min}) z_0^{-1}\}^{-2}$ with a surface roughness length $z_0 = 0.1$ m. The transfer of heat is zero. In agreement with Mirocha et al. (2010) we set $c_s = 0.25$ and $Ri_c = 0.7$.

We initialize our simulations with a dry neutral stratification and an Ekman-spiral for a geostrophic wind $u_G = 10\ \mathrm{m\ s^{-1}}$. The Ekman layer depth equals our domain height. Following the approach of Andren et al. (1994) random perturbations are added to the initial velocities to spin-up a fully-turbulent flow. The maximum magnitude u' of the perturbations decreases from $\pm 0.5\ \mathrm{m\ s^{-1}}$ at the surface to zero at 700 m. The Coriolis force is applied to perturbations from the geostrophic background flow.

3.2 Results

Inertial oscillations with a time period of $2\pi/f \sim 17$ h are expected before a steady state is reached after ~ 80 hours. Andren et al. (1994) defined non-stationarity parameters with a value of one as soon as the steady-state solution is reached. A time-period of 24 hours is simulated here, since the steady-state solution is not of primary interest. Figures 2a,b demonstrate that COSMO-LES is capable of capturing the frequency of these oscillations.

The turbulence closure itself performs as expected. Coherent structures (see Fig. 2c) appear to be of similar structure as those obtained from WRF simulations (Mirocha et al. 2010). Figure 3a shows the averaged wind profile normalized by the (time-averaged) friction velocity $u_* = 0.41$. Chow et al. (2005) found a similar value of 0.44. The wind shear in the surface layer is overestimated with too strong winds in the upper parts of the surface layer. Also shown is the dimensionless wind shear ϕ (see Fig. 3b), which deviates from the expected value of one in the surface layer. These features are well known and characteristics of the Smagorinsky model (e.g., Mason and Thompson 1992; Chow et al. 2005). The splitting of the Reynolds-stresses and the assumptions made for the lower boundary condition appear to have only minor impacts on the wind speed close to the surface. This is reasonable, since close to the surface the dominating contributions to τ_{13} and τ_{23} are the vertical derivatives of the horizontal velocities. The omitted explicit contributions to the near-surface stress seem to be negligible.

[2] Note that three grid lines are used for periodic data exchange at each lateral boundary.

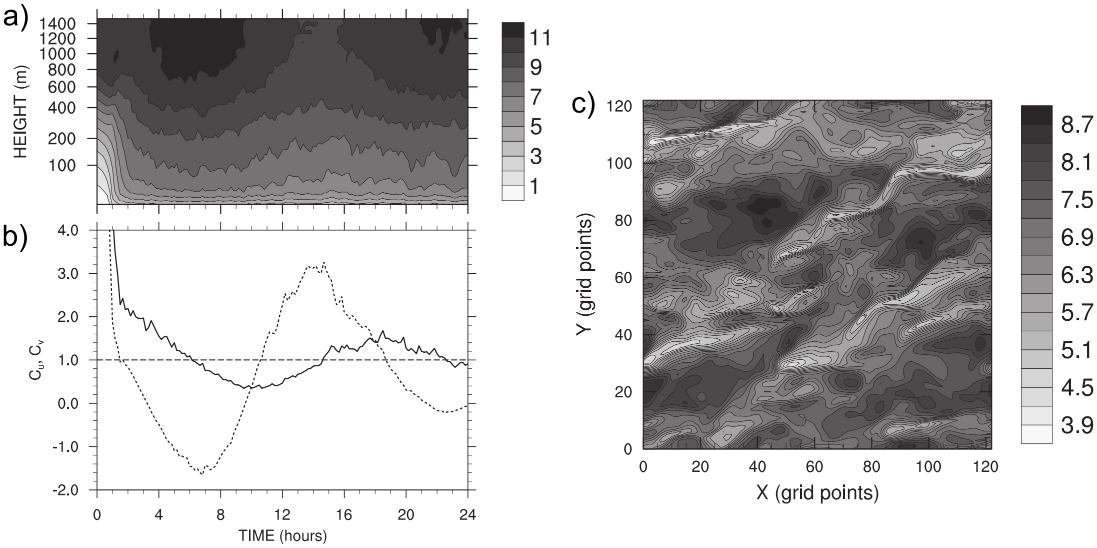

Figure 2: First-order quantities as simulated with COSMO-LES: Time-evolution of (a) mean u-velocity (m s^{-1}) and (b) non-stationarity parameters (solid) C_u and (dashed) C_v and (c) horizontal cross section of u-velocity (m s^{-1}) at 47 meters above ground and after 18 hours. Data output interval in (a,b) is 10 minutes.

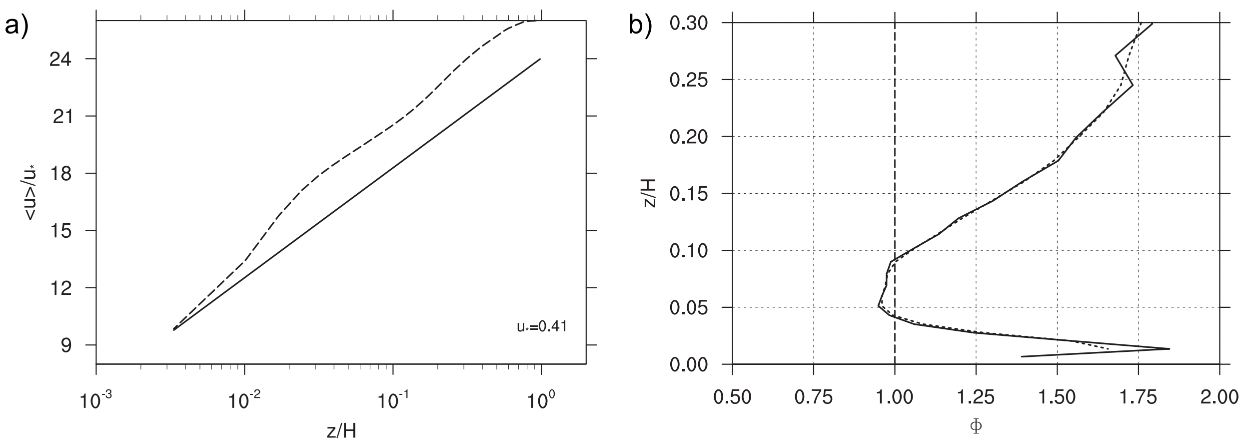

Figure 3: Averaged vertical profiles between 4 and 24 hours: (a) Semi-logarithmic diagram of wind speed normalized by the averaged friction velocity, (b) nondimensional wind shear. The solid line in a) indicates the log-profile obtained from surface layer similarity theory and a 1-2-1 filtered shear profile (dashed curve) has been added in panel b).

4 Simulation of the convective PBL

The convective boundary layer has been the focus of several studies in the past. Nieuwstadt et al. (1993) (abbreviated N93 in the following) shows that LES codes reproduce its characteristics very well. Compared to wall-bounded flows, the characteristic eddy size is determined by the boundary layer depth and can usually be resolved on the grid without the need for excessively small grid-spacings. Moreover, the CBL is less sensitive to the formulation of the lower boundary condition.

4.1 Model setup

The same discretization schemes and boundary conditions are applied as described above. The domain spans 5×5 km^2 in the horizontal and 2 km in the vertical direction. If not mentioned otherwise, the grid-spacings have been chosen in agreement with Moeng et al. (2007), who applied equidistant grid-spacings of $\Delta x = 50$ m and $\Delta z = 20$ m, giving $101 \times 101 \times 100$ grid-points[3]. The large timestep is 0.25 s.

In designing the initial thermodynamic profile we closely follow Moeng et al. (2007) and specify a constant potential temperature of 300 K below $z_{i0} = 1000$ m, a rapid increase by 8 K over an inversion depth of 150 m, and a constant lapse-rate of 3 K km^{-1} above. Other specifications include the Coriolis parameter $f = 10^{-4}$ s^{-1}, the surface roughness length $z_0 = 0.1$ m, and the critical Richardson (Prandtl) number $Ri_c = 0.46$. The surface sensible heat flux is specified by increasing the surface temperature by 5 K compared to the first level and turbulence is initiated by adding random temperature fluctuations between -0.1 and 0.1 on the lowest four model levels.

Runs with $\Delta x = 25$ m are also conducted. For those runs the time step (number of grid-points) is decreased (increased) in proportion. At both grid-spacings different values of c_s are applied such that both the impact of grid-spacing and the impact of increased subgrid-mixing (at constant grid-spacing) can be analyzed (see Tab. 1). Results are compared to one simulation using ARPS with the same initial and grid specifications. ARPS uses a one-equation mixing-length model, which solves an additional equation for e and relates it to an eddy viscosity. The corresponding Smagorinsky constant c_s would be 0.29 in ARPS. Following Mason and Brown (1999) (abbreviated as MB99 in the following) simulations were run for 10000 s and averaged profiles and spectra were computed over the last 4000 s using a data output interval of 12.5 s (and 60 s for ARPS).

4.2 Results

Simulated statistics of the CBL are presented in Tab. 1. The entrainment flux $\langle w'\theta' \rangle_e$ and the convective velocity scale w_* have been scaled with the actual values of the kinematic surface heat flux Q_s and w_{*0}, respectively, before time-averaging. The entrainment flux of COSMO-LES is slightly stronger than in ARPS. All simulations result in stronger entrainment then in previous LESs (see N93), since a strong temperature inversion at the PBL top is used in our simulations. Thus, the entrainment fluxes are similar to simulations using WRF (Moeng et al. 2007) with the same temperature profile. The spread among the normalized velocity scales w_*/w_{*0} is in agreement with results from several models presented by N93.

Name	l_s (m)	c_s	Δx (m)	z_i (m)	Q_s	$\langle w'\theta' \rangle_e/Q_s$	w_{*0} (m s^{-1})	w_*/w_{*0}
50C29	10.7	0.29	50	1049.84	0.1008	-0.2723	1.4874	1.0143
50C32	11.8	0.32	50	1059.07	0.1012	-0.2701	1.4894	1.0165
50C46	17.0	0.46	50	1047.23	0.1040	-0.2418	1.5030	1.0149
25C29	6.7	0.29	25	1061.43	0.1037	-0.2678	1.5016	1.0176
25C46	10.7	0.46	25	1066.23	0.1048	-0.2897	1.5070	1.0172
ARPS	10.7	0.29	50	1101.19	0.1115	-0.2227	1.5385	1.0286

Table 1: Simulation specifications and statistics of the convective boundary layer obtained from COSMO-LES and ARPS for $9 < t/t_* < 15$ (i.e. 321 output values): boundary layer height z_i, surface kinematic heat flux Q_s, scaled entrainment temperature flux $\langle w'\theta' \rangle_e/Q_s$, convective velocity scale w_{*0}, and scaled velocity scale w_*/w_{*0}.

Figures 4a,b show total and subgrid-scale sensible heat flux profiles. A linear decrease of the total heat flux is obtained in all simulations, but the subgrid-mixing results in positive fluxes above the PBL in COSMO-LES. Owing to a slightly higher surface heat flux the boundary

[3] Again, three grid lines were used for periodic exchange at each lateral boundary.

layer height is marginally higher in ARPS (see also Tab. 1). Although 50C29 and 50C32 produce similar subgrid-fluxes as ARPS near the ground, simulations 50C46, 25C29, and 25C46 result in improved COSMO-LES profiles of the total heat flux near the surface. Using $\Delta x = 25$ m the detrainment of heat at the PBL top is still larger than in ARPS.

Variances of the velocity fluctuations are shown in Figs. 4c,d. The subgrid-scale variance has been computed as $2/3e$, with the subgrid energy e estimated for homogeneous turbulence in equilibrium (see Eq. (7) in Moeng et al. 2007). In general, good agreement with ARPS is achieved. Larger c_s result in reduced total variances. At the PBL top 25C29 results in better agreement of $\langle u'u' \rangle$ with ARPS than 50C29. Such differences in $\langle u'u' \rangle$ have also been found by N93 from different formulations of subgrid-mixing.

Third moments of vertical velocity fluctuations are shown in Figs. 4e,f. Increasing c_s with constant $\Delta x = 50$ m (Fig. 4e) reduces the maximum $\langle w'w'w' \rangle$ such that comparable values are obtained for 50C46 and ARPS. In contrast, 25C46 produces stronger $\langle w'w'w' \rangle$ than 25C29 (Fig. 4f). In general the obtained values of both COSMO-LES and ARPS are higher than those found by N93. In contrast to results presented in previous studies no unphysical negative values are found near the surface.

Total and subgrid temperature variances are shown in Figs. 4g,h. Following N93 the subgrid-scale variance is computed as $0.67^{-4}\langle w'\theta' \rangle^2 e^{-1}$. The profiles agree quite well with ARPS. Only the maximum variance close to the PBL top is larger with COSMO-LES. As indicated by N93 this is a consequence of the increased production of variance related to stronger mean temperature gradients. Indeed, we found higher mean temperature gradients close to the PBL top for COSMO-LES (not shown). Note that in comparison to N93's simulations both models reveal by factor ~ 6 larger $\langle T'T' \rangle$, since a strong temperature inversion is used here at the PBL top.

The effects of grid-spacing and subgrid turbulent length scale are further illustrated in Fig. 5, which shows vertical velocity spectra obtained from all simulations. The spectra have been scaled following MB99. Figure 5 demonstrates that COSMO-LES agrees well with ARPS. Particularly, 50C29, 50C32, and 25C46 reveal very similar spectral distributions to ARPS. In agreement with MB99 the filter scale is determined by the subgrid scheme, since larger c_s (thus larger turbulent length scale) results in stronger filtering for the same numerical grid (see Fig. 5a). Figure 5b shows that, compared to 50C29, 25C29 results in more energy at high frequencies, as the filter scale becomes smaller in 25C29. According to Fig. 5b (and in agreement with MB99) the influence of grid-spacing on simulations with identical turbulent length scale (50C29 vs. 25C46) is small. Note that independently of the distance from the surface COSMO-LES exhibits slightly more energy at the very small scales than ARPS. This is likely related to explicit numerical filtering applied only in ARPS, but not in COSMO-LES.

Finally, Fig. 6 shows horizontal cross-sections of the vertical velocity and the potential temperature fluctuation at z=110 m for both 50C29 and ARPS. Both runs produce secondary flows of warm rising air comparable to previous LESs, e.g., Moeng et al. (2007). Distributions from other COSMO-LES runs are shown in Fig. 7. 25C46, which applies the same turbulent length scale as 50C29, but uses a finer grid-spacing, produces similar widths and strengths of the coherent structures. As expected, a larger turbulent length scale (larger c_s) at constant grid-spacing causes enhanced smoothing of the updrafts (25C29 vs. 25C46).

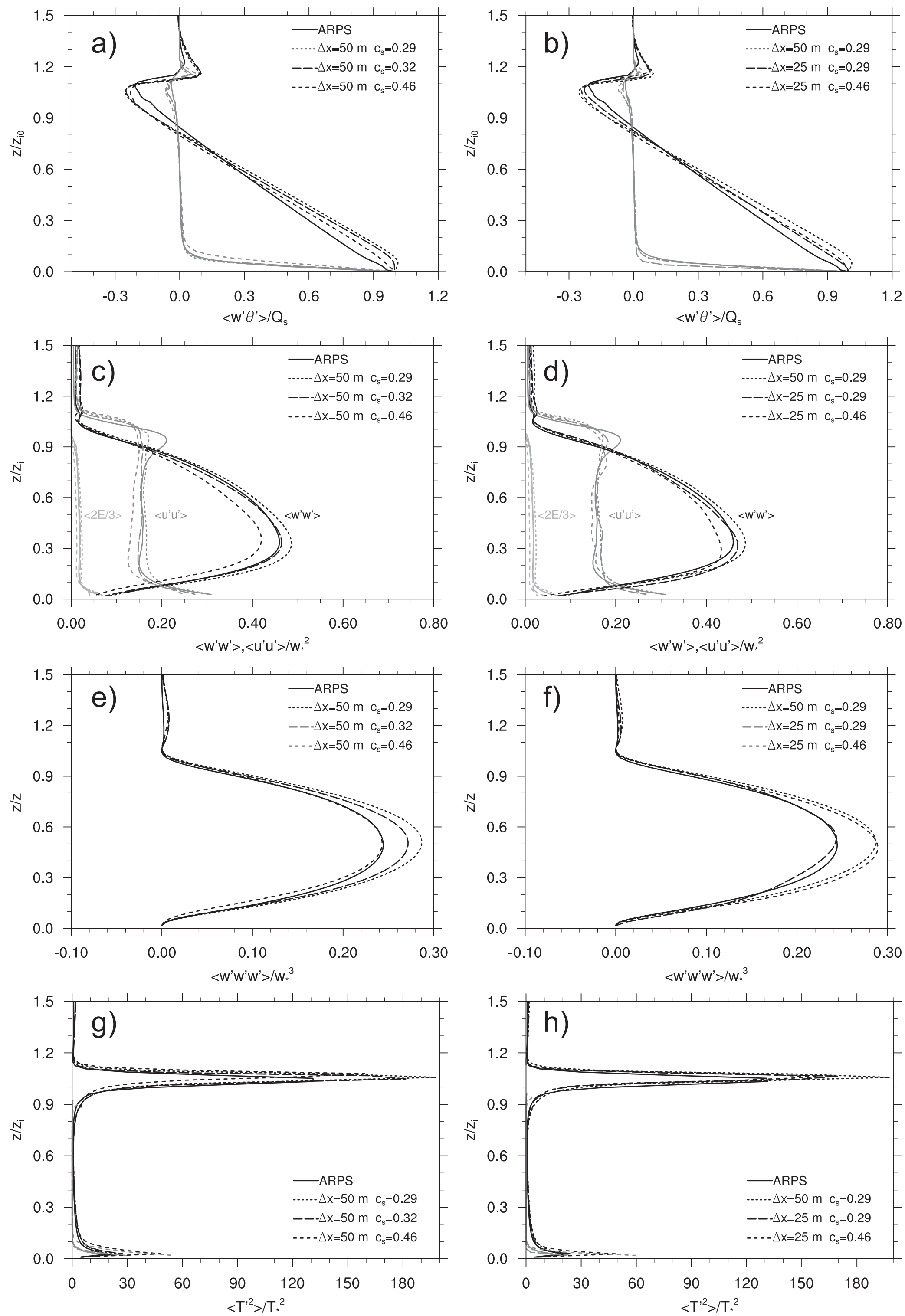

Figure 4: Scaled vertical profiles of domain and time-averaged (a,b) total (black) and subgrid-scale (gray) heat flux, (c,d) w (black), u (dark gray), subgrid-scale (light gray) velocity variances, (e,f) resolved part of third moment of w fluctuations, and (g,h) total (black) and subgrid-scale (gray) temperature variances. Parameters have been scaled by the actual values before averaging. The boundary layer depth z_i is given for each simulation in Tab. 1.

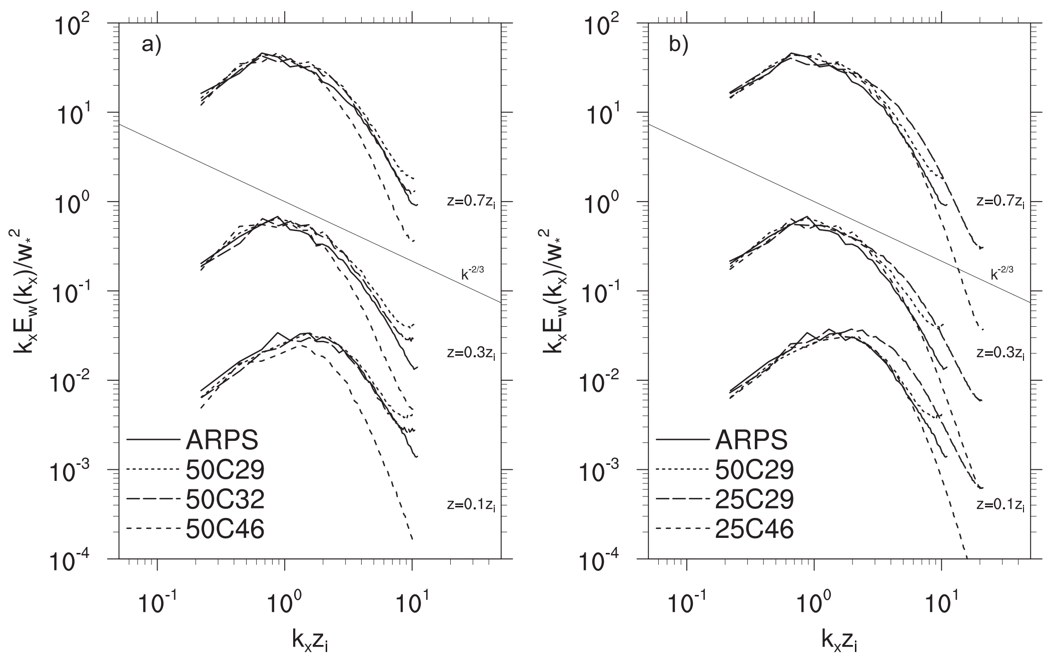

Figure 5: Scaled spectra of vertical velocity at three different levels $0.1z_i$, $0.3z_i$, and $0.7z_i$. Spectra have been computed in x-direction and have been averaged over a time span of 4000 s. The boundary layer depth z_i and velocity scale w_* are both given for each simulation in Tab. 1. Note that the spectral energy has been multiplied by 10 and 1000 at $z = 0.3z_i$ and $z = 0.7z_i$, respectively.

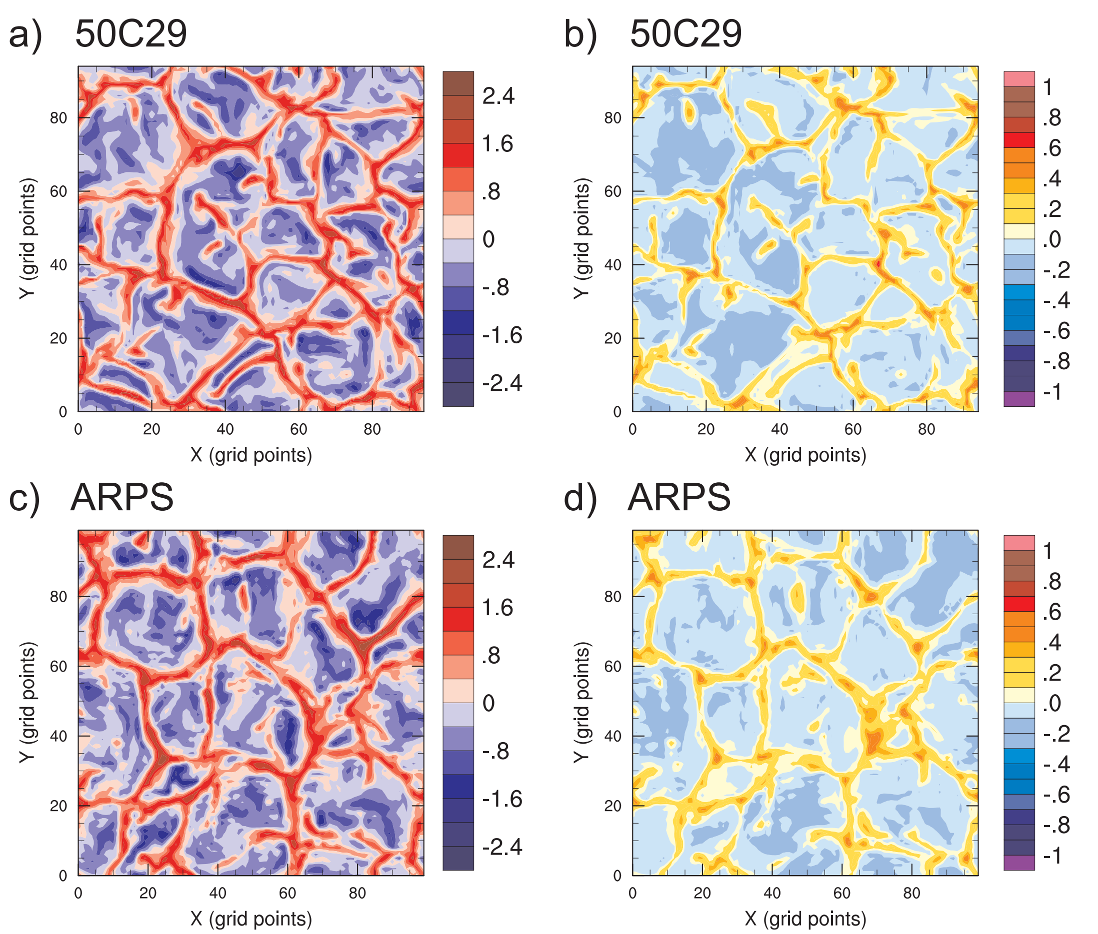

Figure 6: Horizontal cross-sections of (a,c) vertical velocity (m s^{-1}) and (b,d) potential temperature perturbation (K) at $z = 110$ m and after 10000 s from 50C29 and ARPS.

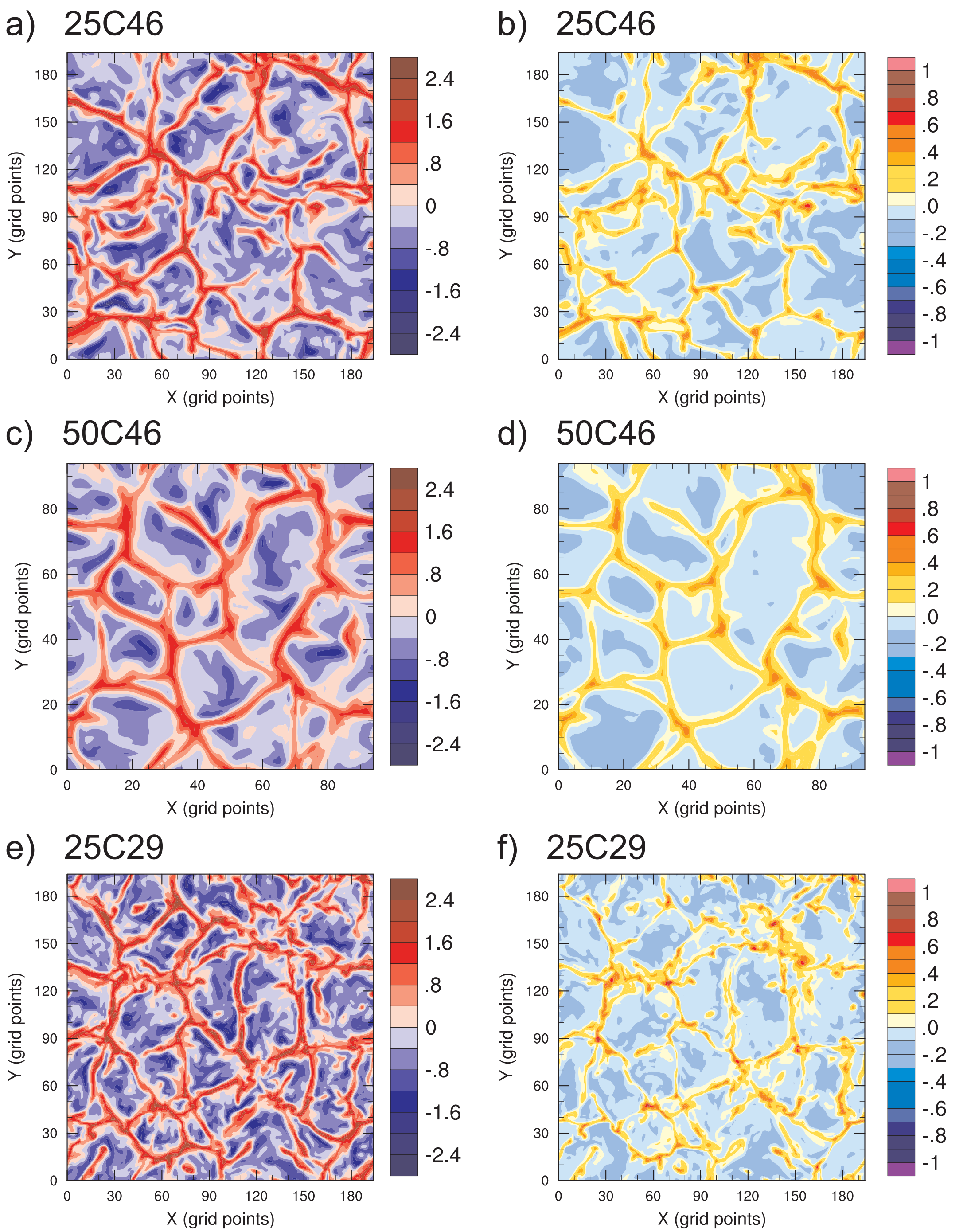

Figure 7: Same as Fig. 6, but from (a,b) 25C46, (c,d) 50C46, and (e,f) 25C29. In 25C46 the same subgrid turbulent length scale l_s is used as in 50C29 (see Fig. 6).

5 Summary and Outlook

A Smagorinsky-Lilly turbulence closure for large-eddy simulations (LES) has been implemented in COSMO. The momentum tendencies had to be split into implicitly and explicitly calculated contributions. Parts of the vertical and all horizontal flux convergences are computed explicitly, while the remaining tendencies from vertical diffusion are solved implicitly. At the lower boundary only the implicitly computed part related to vertical shear of horizontal velocities contributes to the stress. This appears to have little influence on the mean near-surface wind-shear. Simulations of the neutral boundary layer proved that COSMO-LES is capable of reproducing the expected vertical wind-shear as typically obtained from simulations using an eddy viscosity model.

The convective boundary layer as simulated by COSMO-LES has been compared to results obtained with ARPS and to previous studies. A spectral analysis revealed very good agreement of COSMO-LES and ARPS. The simulated vertical profiles of scaled heat flux, velocity and temperature variances, and third moments of the vertical velocity fluctuations demonstrated a general agreement with those references. Only minor deviations to ARPS were found at the very top of the CBL, where larger subgrid-mixing resulted in weak detrainment of heat. Close to the top of the PBL the variances of horizontal velocity were slightly smaller than in ARPS. For smaller grid-spacing ($\Delta x = 25$ m) the variances of horizontal velocity were slightly larger close to the PBL top and the near-surface heat fluxes increased strictly linearly with height.

Future studies would be helpful to address the convergence of COSMO-LES across a larger range of different grid-spacings. A systematic analysis would certainly contribute to an enhanced credibility of COSMO-LES. Although COSMO-LES has also already been used successfully in real-case simulations of deep moist convection, further studies of idealized flows, particularly moist convection, would be helpful to support its credibility to simulate small-scale processes.

References

[1] Andren, A., A.R. Brown, J. Graf, P.J. Mason, C.-H. Moeng, F.T.M. Nieuwstadt, and U. Schumann, 1994: Large-eddy simulation of a neutrally stratified boundary layer: A comparison of four computer codes. *Quart. J. Roy. Meteor. Soc.*, **120**, 1457-1484.

[2] Chow, F.K., R.L. Street, M. Xue and J. H. Ferziger, 2005: Explicit filtering and reconstruction turbulence modeling for large-eddy simulation of neutral boundary layer flow. *J. Atmos. Sci.*, **62**, 2058-2077.

[3] Klemp J.B., R.B. Wilhelmson, 1978: The Simulation of Three-Dimensional Convective Storm Dynamics. *J. Atmos. Sci.*, **35**, 1070-1096.

[4] Mason, P.J. and D.J. Thompson, 1992: Stochastic backscatter in large-eddy simulations of boundary layers. *J. Fluid Mech.*, **242**, 51-78.

[5] Mason, P.J. and A. R. Brown, 1999: On subgrid models and filter operations in large eddy simulations. *J. Atmos. Sci.*, **56**, 2101-2114.

[6] Moeng, C.-H., J. Dudhia, J. Klemp and P. Sullivan, 2007: Examining two-way grid nesting for large-eddy simulation of the PBL using the WRF model. *Mon. Wea. Rev.*, **135**, 2295-2311.

[7] Mirocha J.D., J.K. Lundquist and B. Kosović, 2010: Implementation of a nonlinear subfilter turbulence stress model for large-eddy simulation in the Advanced Research WRF model. *Mon. Wea. Rev.*, **138**, 4212-4228.

[8] Nieuwstadt, F.T.M., P.J. Mason, C.-H. Moeng, and U. Schumann, 1993: Large-Eddy simulation of the convective boundary layer: A comparison of four computer codes. *8th Symposium on Turbulent Shear Flows*, Springer-Verlag.

[9] Pope, S.B., 2000: *Turbulent flows*, Cambridge University Press, pp. 770.

[10] Xue, M., K. K. Droegemeier, and V. Wong, 2000: The Advanced Regional Prediction System (ARPS) - A multiscale nonhydrostatic atmospheric simulation and prediction tool. Part I: Model dynamics and verification. *Meteor. Atmos. Physics*, **75**, 161-193.

Post-processing COSMO output for improved wind forecasts

Conor Sweeney, P. Lynch, P. Nolan and J. Courtney

Meteorology & Climate Centre, University College Dublin, Ireland

1 Introduction

Ireland has a large number of wind farms, which have supplied an average of 15% of system demand over the last year, and have peaked to supply up to 50% of demand (EirGrid), as shown in figure 1. The amount of electricity delivered by wind farms is due to increase, with more wind farms under construction. The government has set an ambitious target of 40% of electricity to be supplied from renewables by 2020. The majority of this is due to come from wind energy.

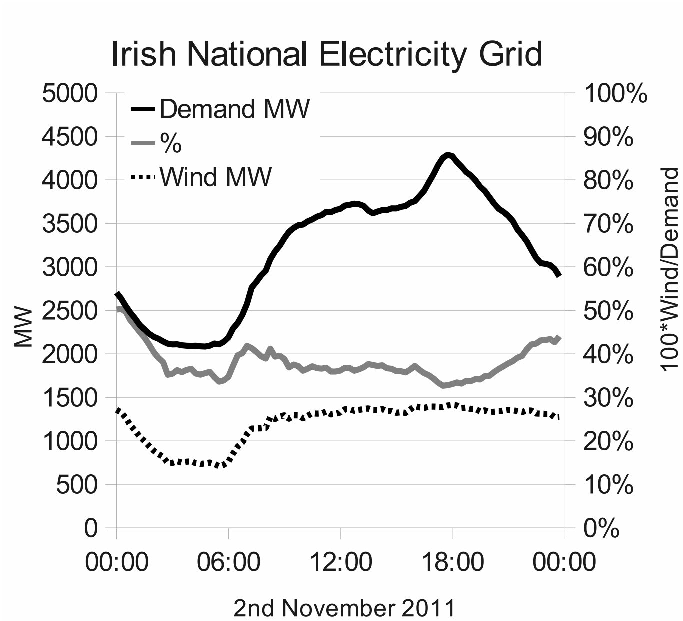

Figure 1: Total grid demand (MW), wind generation (MW), and percentage (100*wind/demand) for the Irish grid (data from EirGrid)

Although wind energy has the benefit of being environmentally friendly, it has the disadvantage of being difficult to integrate efficiently into the national electricity grid. Unlike traditional generators, the wind can not be turned on or off at will.

To help with this potentially costly problem of managing a large amount of wind energy on the grid, there is a keen interest in developing methods to accurately predict when the wind will blow, and how much electricity will be generated.

It is common practice for a forecast office to issue a forecast based, amongst other things, on the output of a numerical weather prediction model (like COSMO!). Even the best model, however, cannot produce a perfect forecast. Some of these forecast errors are difficult to overcome, but others may be due to some systematic process. It is these systematic errors that we hope to reduce by applying post-processing methods to COSMO.

2 Post-Processing Methods

We wanted to consider some simple methods for post-processing COSMO forecasts. Ideally, the methods should require only a short training period, so that they could adapt quickly to changes in COSMO (new versions), as well as changes to the observing networks (new and/or retired stations). The methods used were as follows:

- The **Kalman filter** (Crochet, 2004, Louka et al., 2008) and **Artificial Neural Networks (ANN)** (Salcedo-Sanz et al., 2009). We investigated how the methods used in these recent studies would improve our forecasts, and how they would compare to some simple methods.
- **Short-term bias-correction forecasts (STB)** simply calculated the average error (forecast speed minus observed speed) over the previous 30 days (called the training period), and applied this to the forecast. This, as with the other methods, was done separately for each station location.
- The **linear least-square corrected forecast (LLS)** calculated the linear expression that minimized the least-square-error of the fit between the forecast wind speed and the observed wind speed over the training period, and used this to correct the forecast.
- The **directional-bias forecast (DIR)** tried to take into account the fact that the wind speed error may be different in one direction than another. For example, a nearby hill that is not resolved by the model may act to reduce the wind speed for one direction, but increase it for another direction. The DIR forecast considered all of the wind speed errors and their corresponding wind directions over the training period. The errors were averaged in 30° bins by their directions, and the current forecast wind direction was then used to select the error correction to apply to the forecast wind speed, giving the DIR forecast wind speed.

3 Forecast and Verification

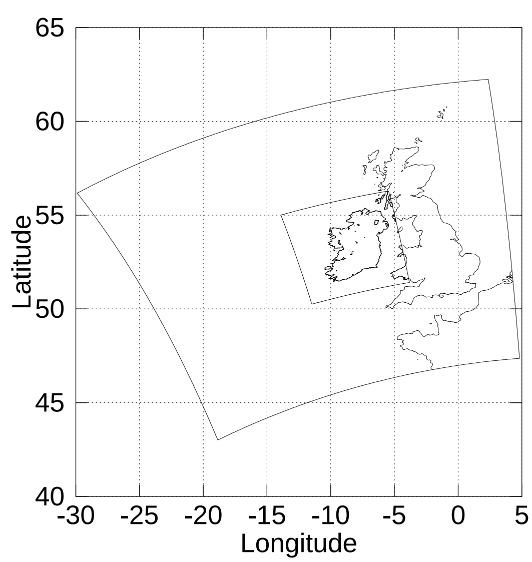

Figure 2: Domains for the 7 km and 3 km COSMO forecasts

We ran 48-hour COSMO forecasts at horizontal resolutions of 7 km and 3 km over a two year period (June 2008 to May 2010). The domains used are shown in figure 2. We used the ECMWF IFS T799L91, which has a horizontal grid spacing equivalent to 25 km, to drive the 7 km forecasts, which then drove the 3 km forecast.

We compared the 10 m wind to observations at 7 stations around Ireland. Using the simple skill scores of bias and root mean square error (RMSE) over the two year period, we found that the post-processing methods produced forecasts with better skill scores than the unprocessed COSMO model output. The LLS, DIR and ANN forecasts gave the best reductions in errors, but *no single method consistently outperformed the others.*

We decided, therefore, to investigate methods to combine the post-processed forecasts to produce a more accurate forecast. We did this using a simple method that assigned weights to each forecast based on its recent skill score, and combined the forecasts using these weights. This combined forecast produced skill scores that were *always equal to or better than* any of the input forecasts.

4 Summary and Outlook

Post-processing the COSMO model output reduces forecast error. Post-processing methods are adaptive, as they are always produced using data from the last 30 days. They are automatic, in that they need no tuning parameters. They are also very computationally efficient; all of the methods used here were run on a standard desktop computer.

By combining a stream of post-processing methods, a forecast can be produced that matches, or exceeds, the skill score of any of the input forecasts. More information on the methods used is available in Sweeney et al.(2011a, 2011b).

The next project we are working on involves taking these post-processing methods, and applying them to an ensemble of forecasts. Much work has already been done with ensembles in the COSMO community (Montani et al. 2010), and we hope that post-processing will be able to help reduce errors in probabilistic forecasts.

This research has a direct application in the wind energy community, as it allows cost/loss decision-making models to be run. These can be used by the electricity grid operator, for example, to decide how much money to spend on reserve capacity for a given time. They could also be used by wind farm operators, to allow them to decide on an optimal bid price for wind energy on an open market.

References

[1] Crochet, P., 2004: Adaptive Kalman filtering of 2-metre temperature and 10-metre wind-speed forecasts in Iceland. *Meteorological Applications*, **11**, 173-187.

[2] Eirgrid Monthly Statistics, available from EirGrid website: *http://www.eirgrid.com.*

[3] Louka, P., Galanis, G., Siebert, N., Kariniotakis, G., Katsafados, P., Pytharoulis, I., Kallos, G., 2008: Improvements in wind speed forecasts for wind power prediction purposes using Kalman filtering. *Journal of Wind Engineering and Industrial Aerodynamics*, **96**, 2348-2362.

[4] Montani A., Cesari D., Marsigli C., Paccagnella T., 2010: Seven years of activity in the field of mesoscale ensemble forecasting by the COSMO-LEPS system: main achieve-

ments and open challenges. *Technical Report*, No. **19**, Available from COSMO website: http://www.cosmo-model.org.

[5] Salcedo-Sanz, S., Pérez-Bellido, Á. M., Ortiz-García, E. G., Portilla-Figueras, A., Prieto, L., Paredes, D., 2009: Hybridizing the fifth generation mesoscale model with artificial neural networks for short-term wind speed prediction. *Renewable Energy*, **34**, 1451-1457.

[6] Sweeney, C. and Lynch, P., 2011a: Adaptive post-processing of short-term wind forecasts for energy applications. *Wind Energy*, **14**, (3):317325.

[7] Sweeney, C., Lynch, P. and Nolan, P., 2011b: Reducing errors of wind speed forecasts by an optimal combination of post-processing methods. *Meteorological Applications*, **doi**, 10.1002/met.294

QPF verification of Italian COSMO-models using different parameters of the precipitation distribution

Maria Stefania Tesini

Hydro meteorological Regional Service ARPASIMC, Bologna, Italy
email: mstesini@arpa.emr.it

1 Introduction

The interpretation of the verification results of precipitation forecasts is often a difficult task because the choice of the verification methods, the reference thresholds or the statistics used to quantify the performance highlights different aspects of the numerical forecast.

In this work the ability of models to represent the shape of the precipitation field within a predefined geographical area, in terms of frequency of exceeding a certain threshold of rain and not in a spatial sense, has been investigated.

The verification methodology applied consists in the comparison of forecast and observation in terms of same parameters of their statistical distribution, evaluated after the precipitation values are aggregated over predefined geographical areas, representing the Italian warning areas for hydro-meteorological events.

Some Italian versions of the COSMO model (COSMO-I7, COSMO-I2, COSMO-ME) and the global model IFS-ECMWF were considered in this study.

The results may provide an interpretation key to a better use of models QPF, especially with respect to high rainfall events.

2 Dataset

Observed precipitation data consisted of more than 1500 rain-gauges made available by the Italian National Department of Civil Protection. The dataset cover almost all the Italian peninsula, (see figure 1(a)) even if it is not homogeneous both in space and time.

In this work we considered only precipitation values accumulated over 24h, starting at 00 UTC from March 2010 to April 2011.

The Italian implementations of the COSMO models involved in the verification are:

- COSMO-I7 (7 Km horizontal resolution performed at Arpa-SIMC)
- COSMO-ME (7 Km horizontal resolution operated at CNMCA)
- COSMO-I2 (2.8 Km horizontal resolution performed at Arpa-SIMC)

The global model IFS-ECMWF(about 16 Km of horizontal resolution), providing the boundary conditions for both the 7 Km COSMO-Models, is also taken into account in this work as a term of comparison to assess the added-value of the higher resolution models.

For all the models the the 24 hours accumulated precipitation at +24h, +48h and +72h for the 00 UTC run has been considered (for COSMO-I2 only +24h and +48h).

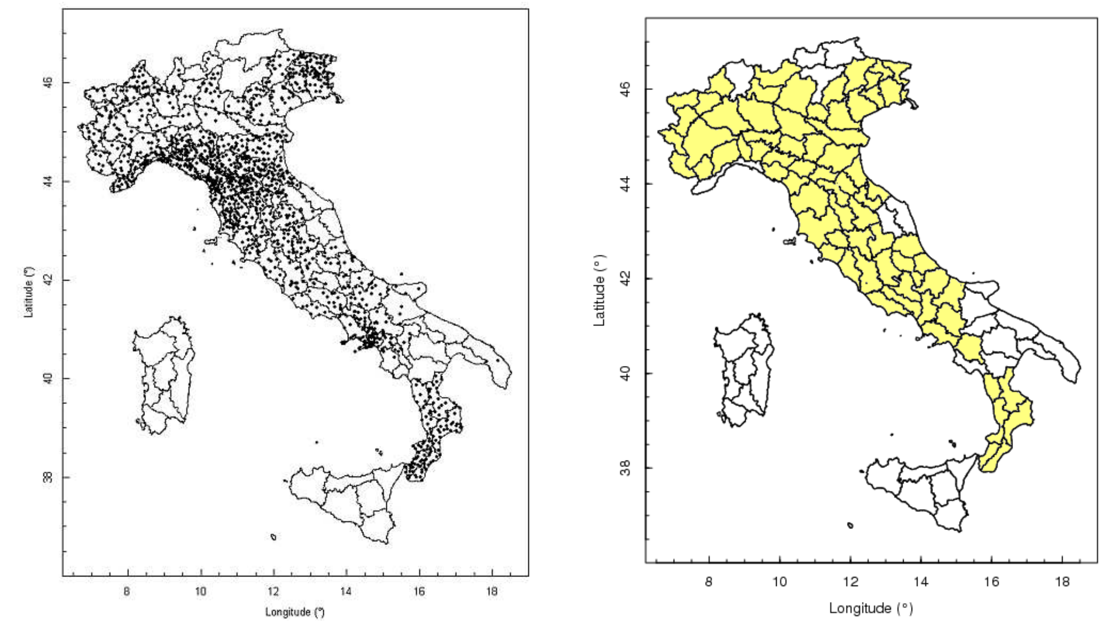

(a) Available rain-gauges (b) Verification areas

Figure 1: Location of available rain-gauges in Italy and geographical areas division

3 Methodology

The verification domain has been divided into about one hundred geographical areas, representing the warning areas of the Italian Civil Protection (see figure 1(b)).

For each day of the verification period and for each area, the maximum value and the median of all the model grid-points that fall in the area, have been computed. Corresponding values have been evaluated also from the observations.

Verification was then performed using a categorical approach: the "yes-no" event was defined according to the condition that the maxima and/or the medians of forecast and observed precipitation distribution exceed a preselected threshold (e.g. maximum greater than 25 mm and median greater than 5 mm in the 24 hours period). Usual quality measures such as Probabilty of Detection, False Alarm Ratio,Threat Score (also known as Critical Success Index) and Bias Score have been derived from the entries of the 2x2 contingency table.

The representativeness of observational data set must be taken into consideration when interpreting results. In fact the choice of the median implies that at least on half of the area the QPF had a value above the reference, regardless of the resolution of the model(even though the points may not be contiguous), while for the observed value this was not always true because the stations are not uniformly distributed over the area. Even when considering the maximum, it is important to remind that the density of stations on the territory was not homogeneous and higher precipitation values could be missed.

4 Results

The results are summarized using a particular type of graphic, the Performance Diagram (Robber,2009), in which it is exploited the geometric relationship between four measures of dichotomous forecast performance: probability of detection (POD), the success ratio (SR, defined as 1-FAR), bias score and threat score (TS, also known as the Critical Success Index). For good forecasts, POD, SR, bias and TS approach unity, such that a perfect forecast lies in the upper right of the diagram. Deviations in a particular direction will indicate relative differences in POD and SR, and consequently bias and TS. An immediate visualization of differences in performance are thus obtained. The influence of sampling variability is estimated using a form of resampling with replacement bootstrapping from the verification data. The 95th percentile range for SR and POD are plotted as "cross-hairs" about the verification point and the variation in bias and CSI is simultaneously displayed. One thousand new samples of the same size as the original are created using the sampling frequencies of observed and forecast "yes" and "no" entries (i.e. the marginal frequencies), and the 25th and 975th accuracy measures are computed from these "climatological" samples to generate the 95th percentile range (description retrieved from the website of WWRP/WGNE Joint Working Group on Forecast Verification Research *http://www.cawcr.gov.au/projects/verification/Roebber/PerformanceDiagram.html*).

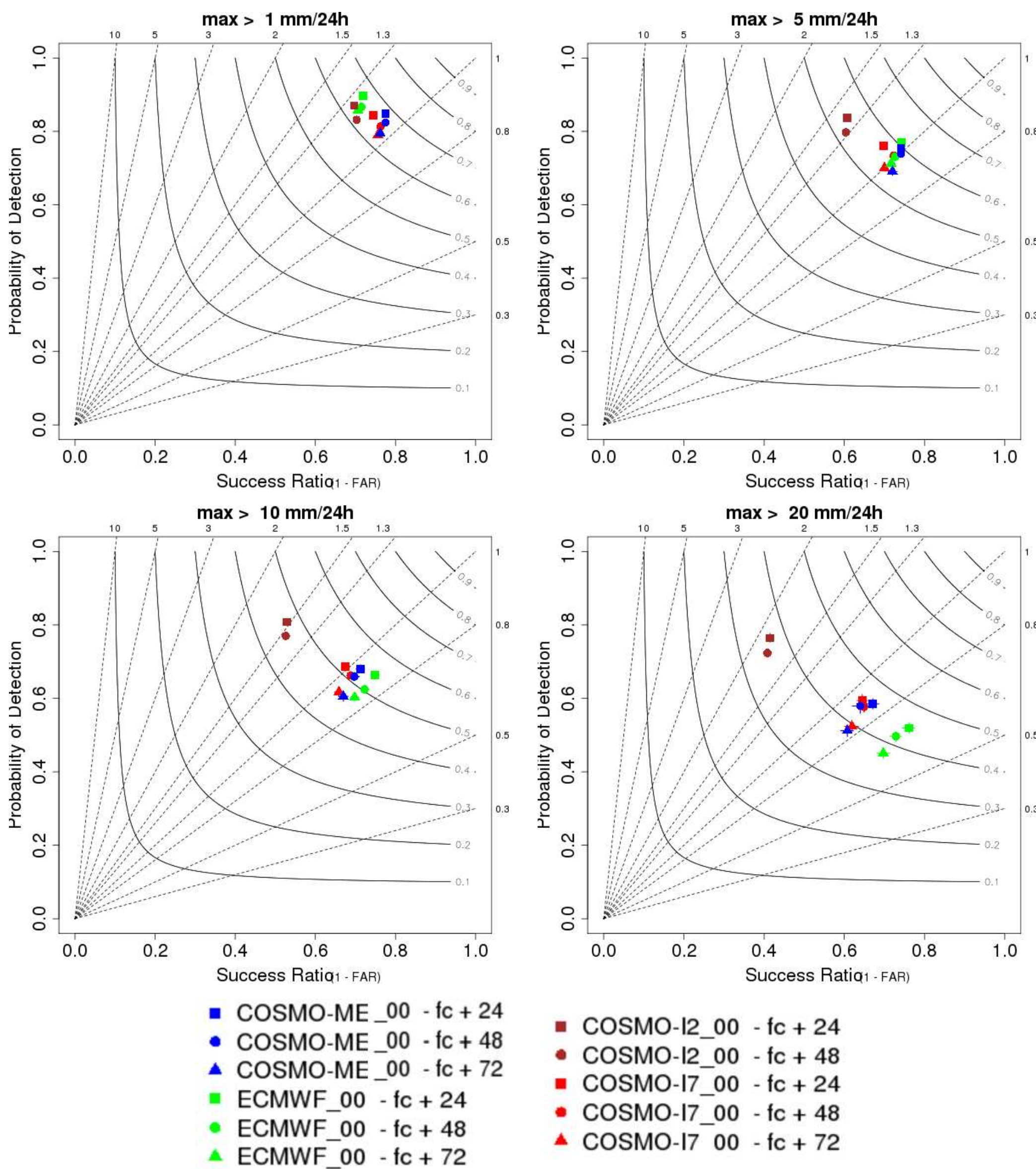

Figure 2: Performance diagrams for the event "maximum value greater than reference thresholds of 1,5,10,20 mm/24h". In the performance diagram are summarized the Success Ratio (1-FAR)in the x-axis, POD in the y-axis. Dashed lines represent Bias Scores with labels on the outward extension of the line, while labelled solid contours are TS. Sampling uncertainty is given by the "cross-hairs", not very visible in this case because the sampling variability is small.

In figure 2 are shown the performance results of models for the event ”maximum value exceeding the reference threshold” for the threshold 1,5,10 and 20 mm in the 24 hours period. At the lower threshold, that means that at least in one point of the area the rain is greater than 1 mm/24h, the threat score of all models is between 0.6 and 0.7, which is definitely a good score, but they show a tendency to overforecast the event. The tendency is more pronounced for IFS-ECMWF and COSMO-I2, which present also a higher number of false alarm, despite a higher POD. Increasing the reference threshold the performances change: ECMWF and the 7 km COSMO models reduce the BS, reaching an unbiased condition, while COSMO-I2 increases the overestimation of the events. The POD of COSMO-I2 is the higher, but the SR decrease. Scores of other models are slightly reduced, although still good, in particular for COSMO-ME. A further increase in the reference threshold to 10 mm/24h and 20 mm/24h shows a general worsening in the POD and TS, but while COSMO-I2 further increases the BS and the number of false alarm, the other models tends to underforecast the event, especially the global model. The difference between the 7 km COSMO models and IFS-ECMWF becomes more pronounced with the increase of the threshold, indicating a greater difficulty for the global model in reproducing relatively high rainfall events.

In figure 3 are shown the results obtained by requiring that two conditions are simultaneously verified. More precisely, the event was defined as ”maximum above 25 mm/24h when the median is greater than a predetermined reference threshold (e.g. 1,5,10,20 mm/24h). The required condition implies that the rain exceeds 25 mm/24h at least in one grid-point/station but also that the precipitation exceeds the specified threshold in half of the grid-points/stations of the area. In this way, taking into account the problems of representativeness of the observational dataset, as previously mentioned, the ability of the models to reproduce some feature of the precipitation distribution over a region (in terms of quantity and not from a spatial point of view) has been investigated. The most salient aspect is that gradually increasing the threshold of the condition on the median, the BS tends to move closer to 1. COSMO-I2 reduces the overestimation of the events while the other models reduce the underestimation of the events, especially IFS-ECMWF. The threat score of the COSMO-I7, COSMO-ME and IFS-ECMWF does not undergo specific changes up to the 10 mm/24h threshold, maintaining approximately the same value with the increase of the reference threshold for the condition on the median, even if improvements in the POD are compensated by deterioration in SR. In the same cases COSMO-I2 reaches TS comparable to that of the other models improving the SR while reducing the POD. It therefore seems that models generally improve the performance in the identification of maximum precipitation when precipitation is spread over much of the area considered. Analyzing the condition of ”maximum and median greater than 25 mm/24h mm/24h greater than 20” (bottom right graph in figure 3) we are in a different situation: COSMO-I2 tends to underforecast events, the scores of all the COSMO model have slightly worsened while IFS-ECMWF behaves better than the other models. So, in the case relatively high and widespread precipitation, higher-resolution models do not seem to add particular value in respect to the global model.

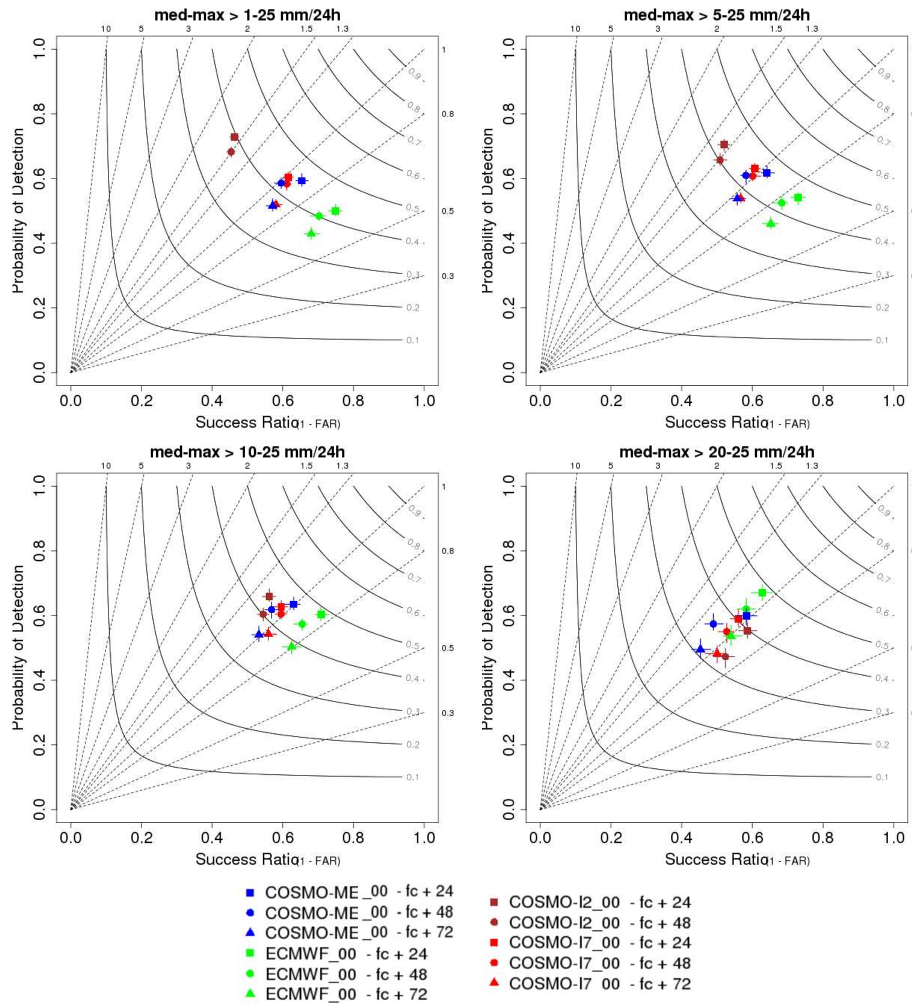

Figure 3: Performance diagrams as in figure 2, but for the event "maximum value greater than 25 mm/24h when the median exceed the reference threshold of 1,5,10 or 20 mm/24h".

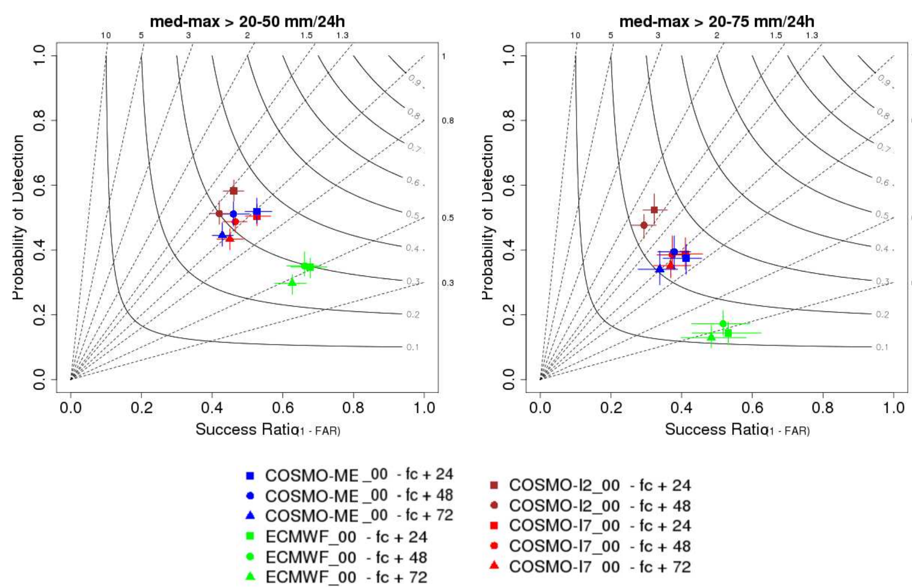

Figure 4: Performance diagrams as in figure 2 , but for the event "maximum value greater than 50 mm/24h and 75 mm/24h when the median exceed the reference threshold 20 mm/24h".

But if the condition on the median is kept fixed and the reference threshold for the condition on the maximum is increased, as shown in the graphs of figure 4, we note that the COSMO models present POD value better than IFS-ECMWF, even if the number of false alarm is large, in particular for COSMO-I2 which also overforecast the events. It should be stressed that the representativeness of the observational data set can be important in this case: the increase in the number of false alarms could depend on the fact that higher precipitation values may have not been actually measured, thereby supporting models that generally underestimates them. We can say that errors of underestimation are surely true while errors of overestimation should be false and need better investigations.

5 Conclusion

In this study we investigated whether the models are able to represent the distribution of precipitation within an area from a quantitative point of view . Some parameters of the forecast and observed precipitation distributions were then evaluated and compared using a categorical approach.

The QPF was first verified by imposing a single condition on the maximum of precipitation then adding a second condition (occurred simultaneously) on the median of the precipitation distributions, in order to select cases of a more widespread rain. In general, the Italian versions of the COSMO model seem to aptly describe the characteristics of the precipitation distribution that have been considered.

The 7 km models (COSMO-I7 and COSMO-ME) show a Bias Score very close to 1 under all the conditions, giving the impression to reproduce the distribution of precipitation in a fairly realistic way. The behavior of the two models is very similar, except the first 24h of forecast where the COSMO-ME is slightly better.

COSMO-I2 is able to capture values of precipitation punctually high, even if it has a large number of false alarms. The overestimations are reduced under the condition that gradually increasing precipitation occur in at least half of the area.

IFS-ECMWF behavior is very sensitive to the reference threshold, especially in detecting the maximum value of the precipitation distribution. When low thresholds are considered the number of events is overestimated and the POD and TS are very good, while for high value of precipitation a strong underestimation of the events and a general worsening in the scores are observed. The global model perform better than the COSMO models in case of widespread and uniform precipitation, but it seems to have some difficulty in the description of the precipitation distribution in case of high maxima (e.g. greater than 50 mm/24h).

It is important to remember that the results may be influenced by the spatial inhomogeneity of the observational datasets, especially in the assessment of the overestimation of the number of events and false alarms.

References

[2] Marsigli,C., Montani,A., Paccangnella,T., 2008: A spatial verification method applied to the evaluation of high-resolution ensemble forecasts. *Meteorol. Appls.*, **15**, 125-143.

[2] Roebber, P.J., 2009: Visualizing multiple measures of forecast quality. *Wea. Forecasting*, **24**, 601-608.

[3] Tesini,MS., Cacciamani,C., Paccagnella,T., 2010: Statistical properties and validation of Quantitative Precipitation Forecast. *COSMO Newsletter*, No. **10**, 45-54.

Description and application of a budget-diagnosis tool in COSMO

Wolfgang Langhans[1], Oliver Fuhrer[2], and Jürg Schmidli[1]

[1] *Institute for Atmospheric and Climate Science, ETH Zurich, Switzerland*

[2] *Federal Office of Meteorology and Climatology MeteoSwiss, Switzerland*

1 Introduction

A budget analysis tool has been implemented into the code of the non-hydrostatic COSMO model in order to diagnose both temperature and moisture tendencies. The implementation allows for the extraction of both physical and dynamical tendencies of either temperature or potential temperature and of moisture scalars. Application of this tool may serve different purposes ranging from numerical developments to process studies and climate science.

A brief description of the retrieval of tendencies is given here and the applied method is exemplified by two simulations. Firstly, an idealized rising warm-bubble test (Wicker and Skamarock 1998) is conducted to explain the underlying temperature tendencies. Secondly, erroneous cold-pool formation in a real-case simulation is studied and the cause for unrealistic cold temperatures will be determined from the budget analysis. As will be demonstrated, the split-explicit time-stepping applied in COSMO complicates the diagnosis of temperature advection tendencies. A further complication is introduced by the COSMO option of solving the heat equation either for temperature or potential temperature. Moisture tendencies related to advection can be obtained much more easily, since the moisture tendencies are numerically solved using discretization schemes without mode-splitting (e.g., a positive-definite scheme).

2 COSMO heat budget

Derived from the first law of thermodynamics the temperature equation solved in COSMO is given as

$$\frac{\partial T}{\partial t} = ADV_T + \frac{1}{\rho c_{pd}}\frac{dp}{dt} + M_L + M_T + M_C + M_{SSO} + M_R + M_{HD} + M_{RLX}. \tag{1}$$

The terms on the right hand side are the heating terms due to advection, pressure changes, latent heating M_L, turbulent flux divergence $M_T = -\frac{1}{\rho c_{pd}}\nabla\cdot\mathbf{H}$, parameterized convection M_C, parameterized drag due to subgrid-orography M_{SSO}, radiative flux divergence M_R, computational mixing M_{HD}, and relaxation at lateral and top boundaries M_{RLX}. The advective tendency is written as

$$ADV_T = \underbrace{-\left[\frac{1}{a\cos(\varphi)}\left(u\frac{\partial T'}{\partial\lambda} + v\cos(\varphi)\frac{\partial T'}{\partial\varphi}\right)\right]}_{HADV_{T'}} - \dot{\zeta}\frac{\partial T'}{\partial\zeta} - w\frac{dT_0}{dz}. \tag{2}$$

Here λ, φ, and ζ are the transformed coordinates. Primes indicate deviations from the model's base-state temperature $T_0(z)$, $\mathrm{HADV}_{T'}$ is the horizontal advection of T', ρ is the density of air, and a is the Earth's radius. Alternatively, a potential temperature equation can be solved in COSMO (namelist options `itheta_adv=1,2`), given as

$$\frac{\partial \theta}{\partial t} = ADV_\theta + \frac{\theta}{T} M_{\sum} \tag{3}$$

$$ADV_\theta = \underbrace{-\left[\frac{1}{a\cos(\varphi)}\left(u\frac{\partial \Phi}{\partial \lambda} + v\cos(\varphi)\frac{\partial \Phi}{\partial \varphi}\right)\right]}_{HADV_\Phi} - \dot{\zeta}\frac{\partial \Phi}{\partial \zeta} - \begin{cases} w\frac{d\theta_0}{dz} & \text{for} \quad \Phi = \theta' \\ 0 & \text{for} \quad \Phi = \theta \end{cases} \tag{4}$$

with $M_{\sum}$ an abbreviation for all diabatic temperature tendencies introduced above. Thereby, advection can be computed for either $\Phi = \theta$ or $\Phi = \theta'$. All temperature tendencies in Eqs. (1) and (3) are evaluated at mass points.

The adiabatic part of the temperature equation is solved using a time-splitting method (Wicker and Skamarock 2002). Thereby, terms related to acoustic and gravity-wave propagation are typically solved implicitly on smaller timesteps. In COSMO the term related to the total derivative of pressure (see Eq. (1)) and the vertical advection of the temperature base-state T_0 (alternatively θ_0) (last terms in Eqs. (2) and (4)) are solved on small timesteps, while the remaining advective tendencies are evaluated on Runge-Kutta substeps (see also Gassmann and Herzog 2007). In case of $\Phi = \theta$ the complete temperature equation is solved on Runge-Kutta substeps without fast-mode contributions. In total three different formulations are available in COSMO to solve the heat equation using Runge-Kutta time-integration (see also Tab. ??). All other M terms are computed as slow processes outside the Runge-Kutta integration.

`itheta_adv`	0	1	2
equation for	T'	θ'	θ
fast-mode	$\frac{1}{\rho c_{pd}}\frac{dp}{dt} - w\frac{dT_0}{dz}$	$-w\frac{d\theta_0}{dz}$	-
slow-mode	$HADV_{T'} - \dot{\zeta}\frac{\partial T'}{\partial \zeta}$	$HADV_{\theta'} - \dot{\zeta}\frac{\partial \theta'}{\partial \zeta}$	$HADV_\theta - \dot{\zeta}\frac{\partial \theta}{\partial \zeta}$

Table 1: Overview of three different available methods (set by namelist switch `itheta_adv`=0–2) for solving the temperature equation in COSMO. For each option the dynamic temperature tendencies computed on small and large timesteps (i.e., Runge-Kutta substeps) are indicated. Note that in any case diabatic tendencies $M_{\sum}$ are computed outside the Runge-Kutta integration.

An implicit Crank-Nicholson discretization is applied in the fast-wave solver. This results in a time-averaged equation for the updated temperature (either T or θ) after one small timestep $\Delta\tau$, given in case of 2nd-order accurate differencing as

$$T_k^{\nu+1} = T_k^\nu + (f_T^n)_k \Delta\tau \tag{5}$$

$$\underbrace{-\frac{p_k^n}{c_{vd}\rho_k^n}(D_h^{\nu+1})_k\Delta\tau + \frac{C_k^{p1}}{c_{pd}\rho_k^n}\left\{\beta^-(w_{k+1}^\nu - w_k^\nu) + \beta^+(w_{k+1}^{\nu+1} - w_k^{\nu+1})\right\}}_{\frac{1}{\rho c_{pd}}\frac{dp}{dt}} \tag{6}$$

$$\underbrace{-\frac{dT_0}{dz}(\beta^-\overline{w^\nu}^\zeta_k + \beta^+\overline{w^{\nu+1}}^\zeta_k)}_{T_0-\text{advection}}. \tag{7}$$

Here $(f_T^n)_k$ corresponds to the slow-mode tendencies at time step n and level k, which are kept constant during all Runge-Kutta stages, and $(D_h^{\nu+1})_k$ is the horizontal divergence. Detailed information on the fast-mode discretization and the notation is given in the COSMO documentation (Doms and Schättler 2002, pp. 64–68). In COSMO the total derivative of pressure consists only of the divergence term (6); the effects from diabatic heating are neglected. In more sophisticated cloud models these effects are included. As mentioned earlier, the advection of the temperature base-state (7) is computed for T' and θ' advection (`itheta_adv`=0,1).

To diagnose the complete advective tendencies the fast-mode advection is accumulated over all small timesteps during the final Runge-Kutta stage and added to the slow-mode advective tendencies. Since the pressure tendency term in (1) is not computed in case of a θ formulation (`itheta_adv`=1–2), the temperature advection can not be obtained from potential temperature advection in these cases. The other way round, in case of T'-advection (`itheta_adv`=0) the potential temperature advection can be diagnosed at the end of each large timestep as the difference of net potential temperature tendency and diabatic tendencies. To summarize, while advective θ tendencies can be retrieved for `itheta_adv=0--2`, T advection is only diagnosable in case of `itheta_adv=0`.

Moreover, for optimal physical interpretation of advective tendencies, the horizontal and vertical components should be related to advection in physical space, not transformed space. Thus, vertical advection is additionally diagnosed each timestep using second-order centered differences in physical space.

3 COSMO moisture budget

COSMO includes several bulk microphysics parameterizations for grid-scale precipitation. The most complex single-moment formulation (Reinhardt and Seifert 2006) distinguishes between the specific humidity q_v, cloud water q_c, cloud ice q_i, rain water q_r, snow q_s, and graupel q_g, in total six budget equations. To keep the amount of output small, the budget tool diagnoses only the tendencies of two classes of hydrometeors: precipitating $(q_r + q_s + q_g)$ and non-precipitating hydrometeors $(q_c + q_i)$. Together with the budget of water vapor q_v, three moisture budgets are diagnosed and all involved tendencies are evaluated at mass points. For each class q_x the budget equation can be written as

$$\frac{\partial q_x}{\partial t} = ADV_{qx} + Q_L + Q_T + Q_C + Q_{HD} + Q_{RLX} \tag{8}$$

with advection ADV_{qx}, microphysical exchange processes (including sedimentation) Q_L, turbulent transport Q_T, parameterized convection Q_C, computational mixing Q_{HD}, and relaxation at the domain boundaries Q_{RLX}. All tendencies are computed as slow tendencies outside the RK-dynamics. Thus, the diagnosis of the moisture advection tendencies is not plagued by the complexity introduced by the split-explicit method in case of temperature. Note that COSMO does not compute subgrid-turbulence tendencies for precipitation hydrometeors (thus $Q_T = 0$). The 3D advective tendencies result from either a Semi-Lagrangian (Staniforth and Côté 1991) or a positive-definite (Bott 1989) discretization. As for temperature, truly vertical advection is diagnosed each timestep.

4 Rising bubble test

To illustrate the retrieval of advective tendencies for the three different types of temperature advection a rising warm-bubble simulation is conducted here in two dimensions. The setup closely follows the description given by Wicker and Skamarock (1998). The domain is 20×10 km^2 large and a uniform grid-spacing of 100 m is applied. The long timestep is 2 s and neither computational nor subgrid turbulent diffusion is used. If not mentioned otherwise, horizontal and vertical advection are discretized using a 5th-order upstream scheme and the model's base-state temperature profile equals a dry neutral stratification with $\theta = 300$ K. The initial thermodynamic conditions are prescribed by a potential temperature disturbance, given as

$$\theta' = 2\cos^2\left(\frac{\pi L}{2}\right) \quad \text{with} \quad L = \sqrt{\left(\frac{x - x_c}{x_r}\right)^2 + \left(\frac{z - z_c}{z_r}\right)^2}, \tag{9}$$

that is added to the dry neutrally stratified atmosphere ($\theta = 300$ K). The disturbance with radius $x_r = z_r = 2$ km is placed at $x_c = 10$ km and $z_c = 2$ km.

Results are analyzed after 1000 s, when the bubble has risen to the center of the domain. The potential temperature and vertical velocity distributions (see Figs. 1a,d) are hardly dependent on the formulation of temperature advection (not shown). All three formulations result in maximum vertical velocities of 14.6 m s^{-1} and maximum θ' perturbations of 2 K and are therefore very similar to results presented using other numerical codes (Wicker and Skamarock 1998; Bryan and Fritsch 2002). However, as a side note, a 2nd-order implicit Crank-Nicholson scheme, which is commonly applied within COSMO for vertical advection, significantly deteriorates the bubbles characteristics (see Figs. 1b,e). A recently developed 3rd-order implicit discretization (see Baldauf 2009) yields considerable improvements (see Figs. 1c,f).

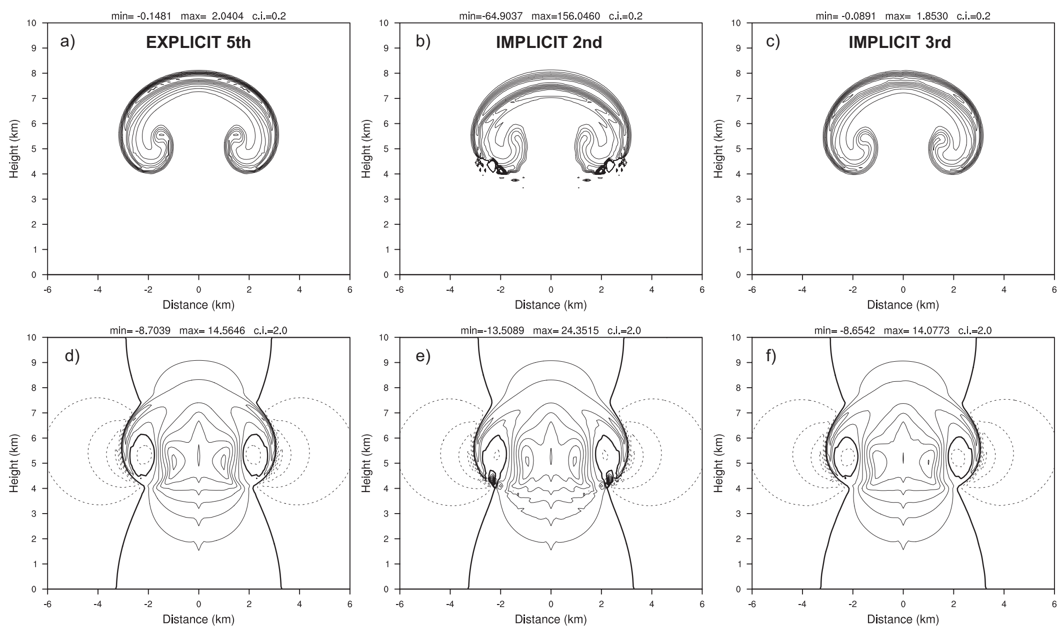

Figure 1: Results of the dry bubble simulation after 1000 s using T'-advection (`itheta_adv=0`): (a–c) Potential temperature perturbation contoured every 0.2 K, (d–f) vertical velocity contoured every 2 m s^{-1}. Vertical T'-advection is computed using (a,d) a 5th-order explicit, (b,e) a 2nd-order implicit scheme, and (c,f) a 3rd-order implicit scheme.

In the following the diagnosis of *potential* temperature tendencies with help of the new implementations is described. Figure 2a shows the net potential temperature tendency, which results from 3D potential temperature advection (see Fig. 2b). Since for this setup the base-state is isentropic the fast-mode tendencies would be zero not only for `itheta_adv=2`, but also for `itheta_adv=1`. The estimated tendencies for vertical advection of θ appear meaningful (see Fig. 2d), as the difference between 3D advection and estimated vertical advection (see Fig. 2e) yields a reasonably good agreement with the actually computed tendencies from horizontal advection, which have also been extracted here (see Fig. 2c).

Finally, the temperature tendencies are studied using `itheta_adv=0`. For the given base-state with $N_0 = 0$ s^{-1} ($\frac{dT_0}{dz} = gc_{pd}^{-1}$) the net temperature tendency (see Fig. 3a) is determined solely

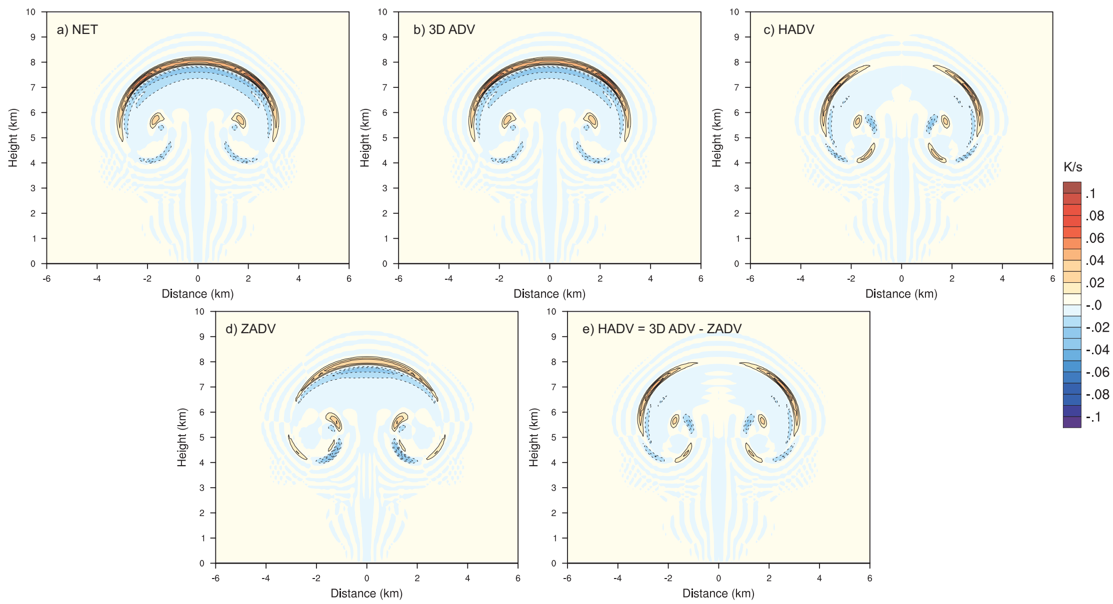

Figure 2: Potential temperature tendencies (K s^{-1}) obtained after 1000 s using θ-advection (`itheta_adv=2`): (a) Net tendency, (b) 3D advection, (c) horizontal advection, (d) estimated vertical advection, and (e) horizontal advection diagnosed as the difference between full advection and estimated vertical advection.

from advection computed on the Runge-Kutta substeps. The tendencies stemming from the fast-mode solver are negligibly small, as temperature changes due to expansion (see Fig. 3c) and due to base-state advection balance each other in adiabatic ascent to a very high degree. Due to this compensation the sum of total advection and pressure forcing (see Fig. 3e) equals the slow-mode advection without base-state advection (see Fig. 3d). Figure 3f indicates that the total advection is primarily determined by vertical advection. Tendencies from horizontal temperature advection (not shown) are similar to horizontal advection of θ (see Fig. 2c).

A second simulation using a base-state of $N_0 = 0.01$ s^{-1} (not shown) further illustrates the partitioning of fast-mode tendencies into base-state advection and pressure forcing. Since for this setup the temperature profile deviates more strongly from its base-state, the magnitude of the T'-advective tendencies evaluated on Runge-Kutta substeps increases and the fast-mode equilibrium with the pressure forcing is disturbed correspondingly.

5 “Cold-pool” case study

Potential applications of the budget diagnosis tool are manifold. It can be used to further the physical understanding of a specific weather or climate phenomenon as well as to aid model development and problem solution. Here, we present an example of its application to the investigation of the formation of unrealistic cold-pools in steep valleys.

On 11 October 2009 the 12 UTC operational COSMO-2 model run crashed because of a runaway cold-pool in a steep Alpine valley which developed near-surface temperatures below 140 K. Similar events have been observed before and at other locations, but generally the unrealistically low near-surface temperature recovers to normal values after some time. Grid points affected by cold-pools are consistently located within a steep valley which is oriented almost perfectly along the N-S or S-W grid lines. The grid point which exhibits cold-pools most frequently is situated in the Saaser valley and corresponds to a local depression with no outflow (see Fig. 4a).

The 06 UTC COSMO-2 forecast of 5 May 2009 also developed a strong cold-pool in the

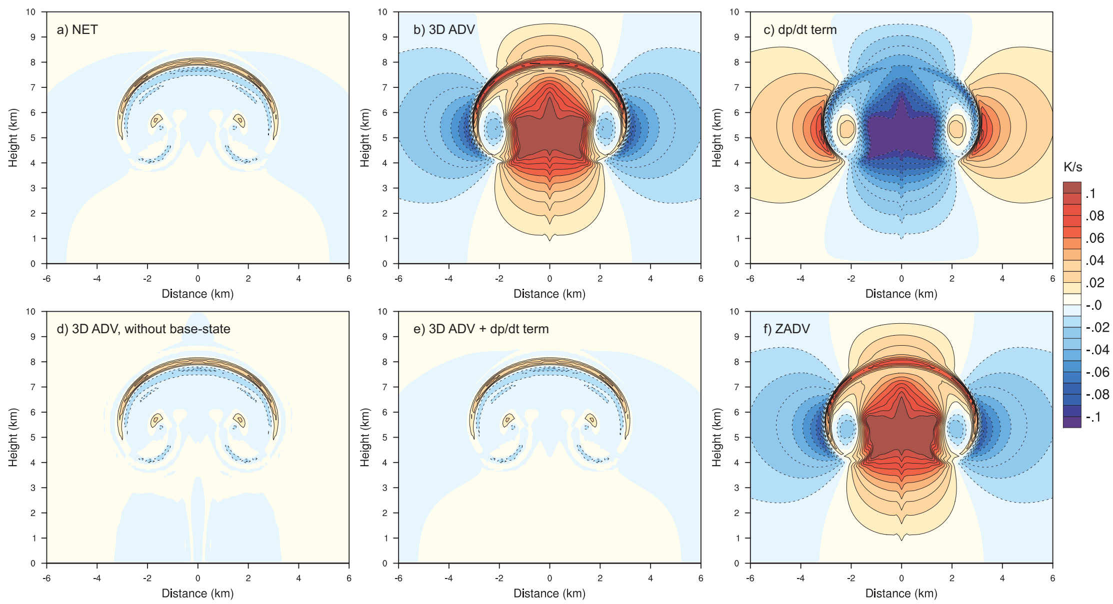

Figure 3: Temperature tendencies (K s^{-1}) obtained after 1000 s using T'-advection (`itheta_adv=0`): (a) Net tendency, (b) 3D advection, (c) $\frac{1}{\rho c_{pd}} \frac{dp}{dt}$ fast-mode term, (d) 3D advection without base-state advection, (e) sum of (b) and (c), and (f) estimated vertical advection.

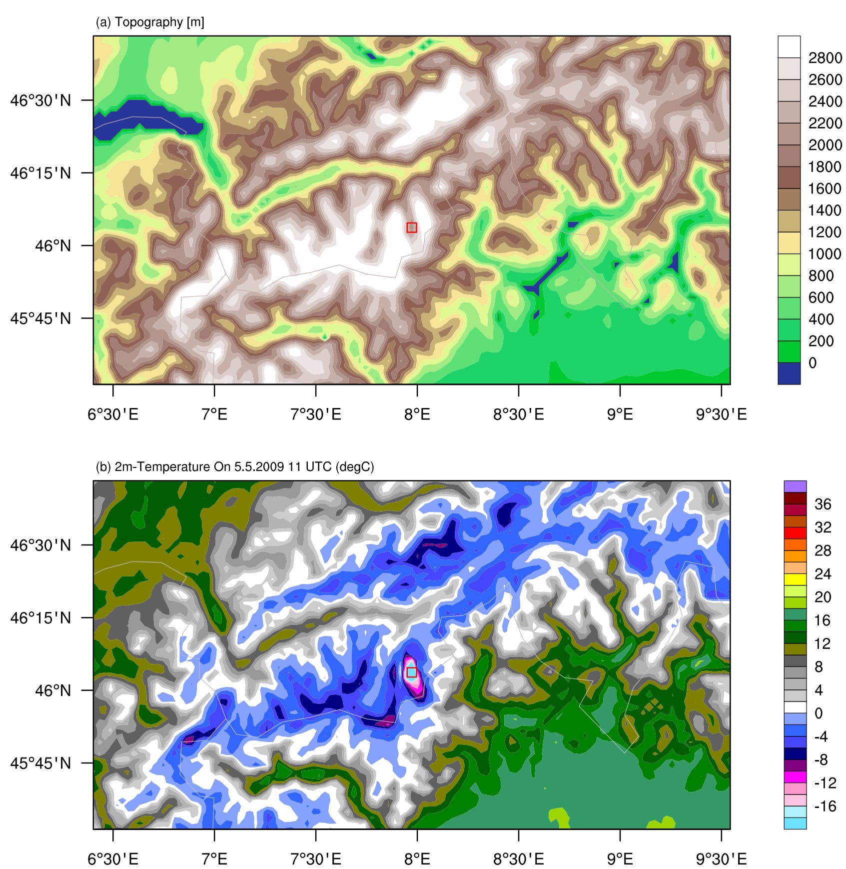

Figure 4: Overview of (a) model topography and (b) 2m-Temperature in °C on 1100 UTC 5 May 2009 after 5 h into the forecast. The grid point with strongest cold-pool development is indicated by a red box.

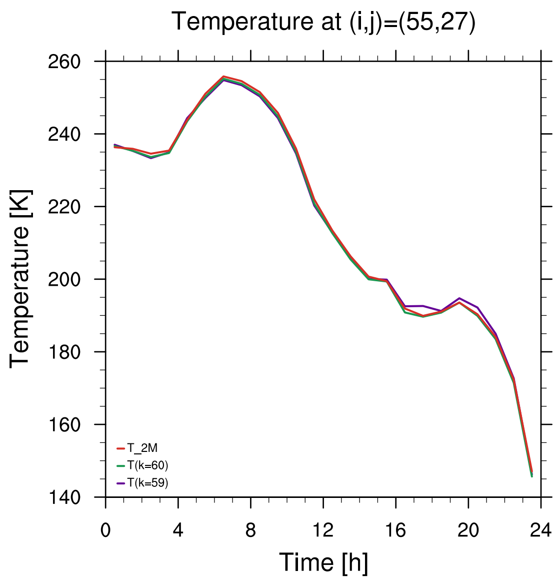

Figure 5: Time series of temperatures at 2 m and on the lowest two model levels (T60, T59).

Saaser valley and is further investigated here. For this event the model did not crash but the cold-pool was unusually persistent and present in over 30 consecutive COSMO-2 forecasts. After 5 h of forecast time (i.e., at 11 UTC) the 2m-temperature distribution (see Fig. 4b) shows a region of unrealistically cold temperatures ($T_{2m} < 243$ K) centered around the lowest valley grid point. Over the course of the simulation temperatures fall below 150 K (see Fig. 5). Later into the simulation, the cold air which accumulated in the Saaser valley spilled into the Rhone valley and deteriorated the forecast quality over a large area.

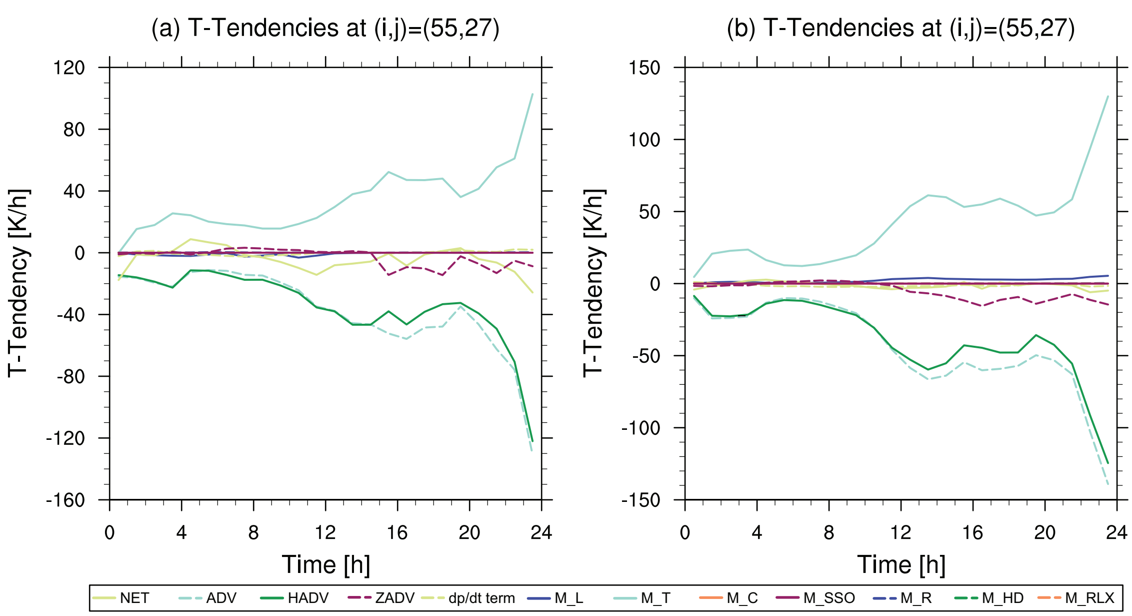

Figure 6: Time series of hourly T-tendencies as determined by the budget diagnosis tool. The budgets are shown for (a) the grid point with lowest temperature and (b) an average over 5x5 grid points around the grid point with lowest temperature.

Further analysis indicates that the forcing responsible for the decreasing temperature does not stem from the surface heat flux, but results from atmospheric cooling that affects the

Earth's surface (not shown). In order to further investigate the source of the forcing, the budget diagnosis tool has been switched on and the simulation repeated. All components of the temperature equation Eq. (1) are shown as hourly averages in Figure 6a. The values shown correspond to the grid point exhibiting the lowest temperatures. The component due to vertical advection (ZADV) has been computed as the difference of the total advective tendency (ADV) and the tendency due to horizontal advection (HADV). The latter results in strong cooling and turbulent diffusion (M_T) counteracts this by mixing with warmer air from higher levels. With the help of the budget diagnosis tool, other processes such as radiative cooling, microphysics, etc. can be excluded from being responsible for the strong cooling. Averaging the tendencies over 5x5 horizontal grid points indicates that this result is robust (see Fig. 6b). Thus, there is a clear indication that in certain topographic configurations the horizontal advection of temperature may introduce a strong spurious forcing leading to the development of cold-pools. This hypothesis is supported by the fact that limiting the temperature advection (`ltadv_limit = .true.`) prevents the cold-pool formation, and that implementing the alternative advection of temperature introduced with model version 4.19 strongly inhibits it.

6 Summary

A budget diagnosis tool has been implemented into COSMO. The implementation allows for the retrieval of heating and moistening rates as computed numerically in the code. Detailed information about the underlying dynamical and physical processes or numerical discretizations can be obtained by studying these tendencies. All tendencies may either be written as instantaneous or as time-averaged quantities. Applications may cover a wide range from model development to process studies at weather and climate scales. Besides the examples provided in this document, the tool has already been applied successfully to study the Alpine heat and moisture budget (Langhans et al. 2011a,b).

References

[1] Baldauf, M. and W. C. Skamarock, 2009: An improved third order vertical advection scheme for the Runge-Kutta dynamical core. *8th International SRNWP-Workshop on Non-Hydrostatic Modelling.*, [Available online at http://www.dwd.de/modellierung].

[2] Bott, A., 1989: A positive definite advection scheme obtained by nonlinear renormalization of the advective fluxes. *Mon. Wea. Rev.*, **117**, 1006–1015.

[3] Bryan, G. H. and J. M. Fritsch, 2002: A benchmark simulation for moist nonhydrostatic numerical models. *Mon. Wea. Rev.*, **130**, 2917–2928.

[4] Doms, G. and U. Schättler, 2002: A description of the nonhydrostatic regional model LM: Part I: Dynamics and Numerics. *Tech. rep.*, [Available online at http://www.cosmomodel.org].

[5] Gassmann, A. and H.-J. Herzog, 2007: A consistent time-split numerical scheme applied to the nonhydrostatic compressible equations. *Mon. Wea. Rev.*, **135**, 20–36

[6] Langhans, W., J. Schmidli, and C. Schär, 2011a: Mesoscale impacts of explicit numerical diffusion in a convection-permitting model. *Mon. Wea. Rev.*, doi:10.1175/2011MWR3650.1

[7] Langhans, W., J. Schmidli, and C. Schär, 2011b: Bulk convergence of cloud-resolving simulations of moist convection over complex terrain. *J. Atmos. Sci.*, submitted.

[8] Reinhardt, T. and A. Seifert, 2006: A three-category ice-scheme for LMK. Tech. rep. *COSMO newsletter*, **6**, 115–120 pp. [Available online at http://www.cosmo-model.org].

[9] Staniforth, A. and J. Côté, 1991: Semi-lagrangian integration schemes for atmospheric models - A review. *Mon. Wea. Rev.*, **119**, 2206–2223.

[10] Wicker L. J. and W. C. Skamarock, 2002: Time-splitting methods for elastic models Using forward time schemes. *Mon. Wea. Rev.*, **130**, 2088–2097.

[11] Wicker L. J. and W. C. Skamarock, 1998: A time-splitting scheme for the elastic equations incorporating second-order Runge-Kutta time differencing. *Mon. Wea. Rev.*, **126**, 1992–199.

A Note on the Direct Comparison of Synthetic Satellite Images from COSMO Model with MSG Products

Avgoustoglou Euripides

Hellenic National Meteorological Service

1 Introduction

The meteorological satellite observations provide a substantial and extensive source of data for comparison with numerical weather prediction models (Refs. Reichert et al. 2004, Reichert et al. 2005, Reichert et al. 2006). We examine the synthetic satellite images produced by the COSMO model, version 4.11 (COSMO_4.11) in reference to Meteosat 9 (MSG) data. These data are available on real time at HNMS and are manipulated through SYNESAT software for operational use. In particular, the infrared of 3.9 μm and 10.8 μm as well as the water-vapor channels of 6.2 μm and 7.3 μm were considered. Furthermore, the model low, medium, high and total cloud covers are directly compared with the corresponding MSG products produced by the Meteorological Products Extraction Facility Algorithms (MPEF).

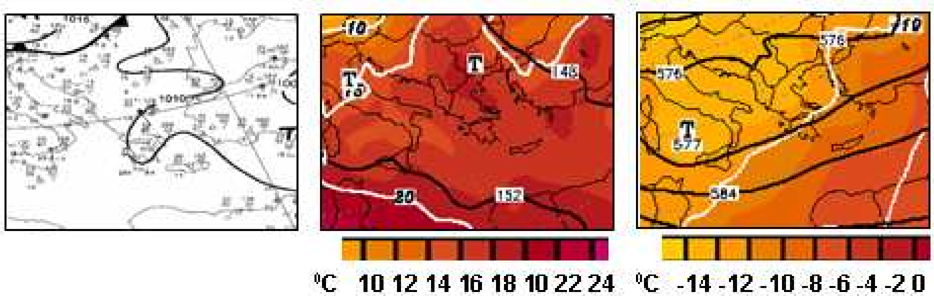

Figure 1: Surface (left), 850 Hpa (medium) and 500 Hpa (right) analysis on August 31 2011 at 00 UTC ©Deutscher Wetterdienst.

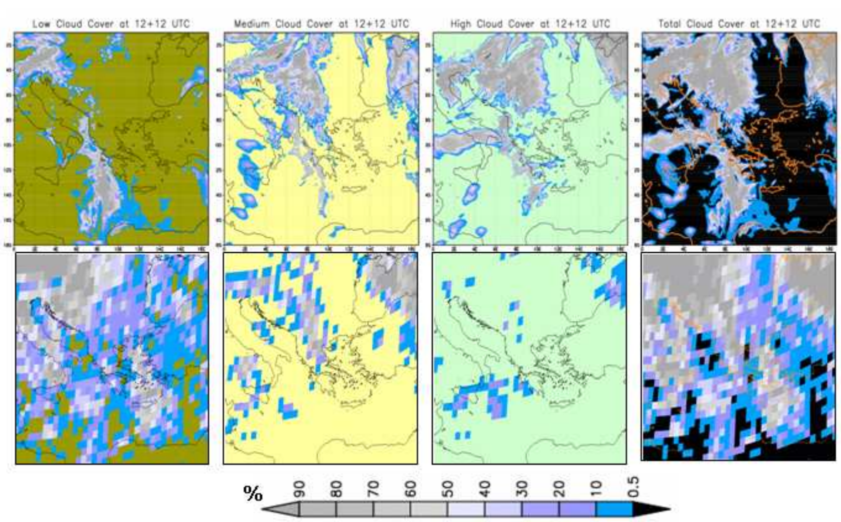

Figure 2: Cloud cover on August 31 2011 at 00 UTC from COSMO model (upper row) in reference to the corresponding satellite (MPEF) figures (lower row ©EUMETSAT). The first, second, third and fourth columns refer to low, medium, high and total cloud cover respectively.

2 Case Study

A 36-hour period was considered, starting from 12 UTC of August 30 2011. The boundary conditions came from three-hour, forty-level analysis intervals based on GME and with horizontal grid of 0.5^0 ($\sim$ 50 Km). The horizontal grid size of COSMO model run was 0.0625^0 ($\sim$ 7 Km) and the integration time step was 30 secs. The run was based on the default sub-grid statistical cloud scheme based on relative humidity. The domain under consideration is the wider Balkan Area with Greece at its center.

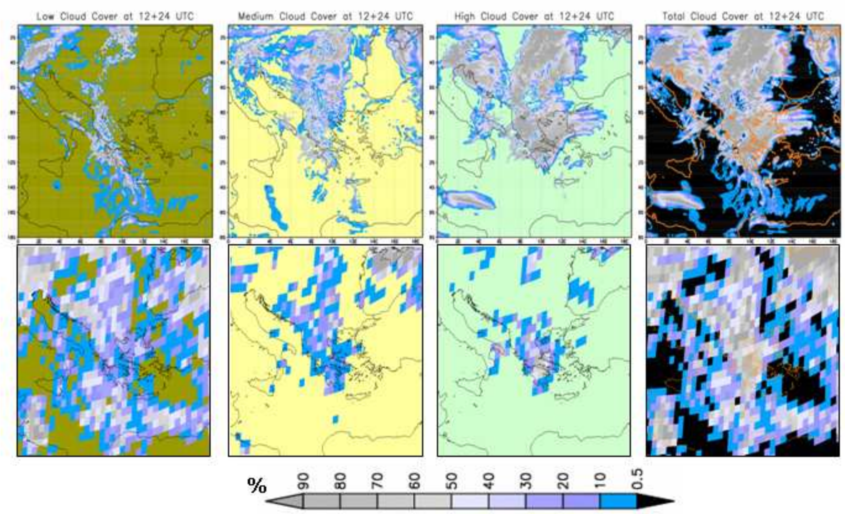

Figure 3: Cloud cover on August 31 2011 at 12 UTC from COSMO model (upper row) in reference to the corresponding satellite (MPEF) figures (lower row ©EUMETSAT). The first, second, third and fourth columns refer to low, medium, high and total cloud cover respectively.

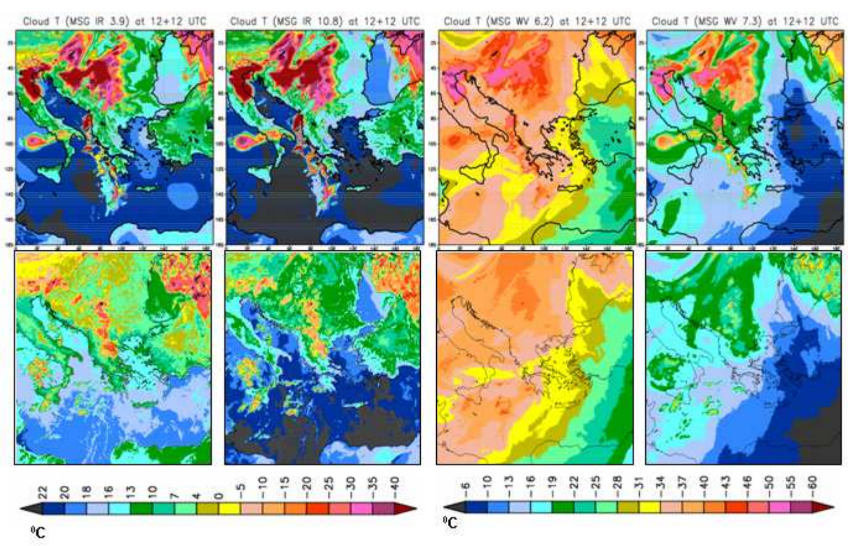

Figure 4: Cloudy brightness temperatures for artificial satellite images on August 31 2011 at 00 UTC from COSMO model (upper row) in reference to the corresponding MSG satellite figures (lower row) ©EUMETSAT. The first, second, third and fourth columns refer to 3.9 μm, 10.8 μm, 6.2 μm and 7.3 μm channels respectively.

From the synoptics standpoint (Fig. 1), the 500 Hpa geopotential analysis chart shows a relatively weak west south-west wind field over the region. This feature, combined with the almost homogeneous mean sea level pressure field of 1010 hPa associated with an extended weak barometric low over the east led to an extensive cloud cover over the whole domain.

Regarding low cloud cover (Fig. 2 and Fig. 3), it is underestimated by the the model with respect to cloud analysis, especially over marine areas. The situation is reversed for high cloud cover which is overestimated by the model, mainly over land. The very good agreement for middle cloud cover between the model and cloud analysis "hides" these differences to a degree , mainly for high clouds, leading to good agreement for the total cloud cover. However, over the areas where the low clouds preponderate the model performance looks quite modest. The above situation is highlighted in the comparison of cloudy brightness temperatures between MSG and synthetic satellite images created by COSMO model (Fig. 4 and Fig. 5). In the infrared channels, the MSG images show lower cloudy brightness temperatures than the corresponding synthetic satellite images over the marine areas and higher cloudy brightness temperatures over most of the land areas. It is worth observing however that this trend regarding the mainland of Greece is not followed in Fig. 4.

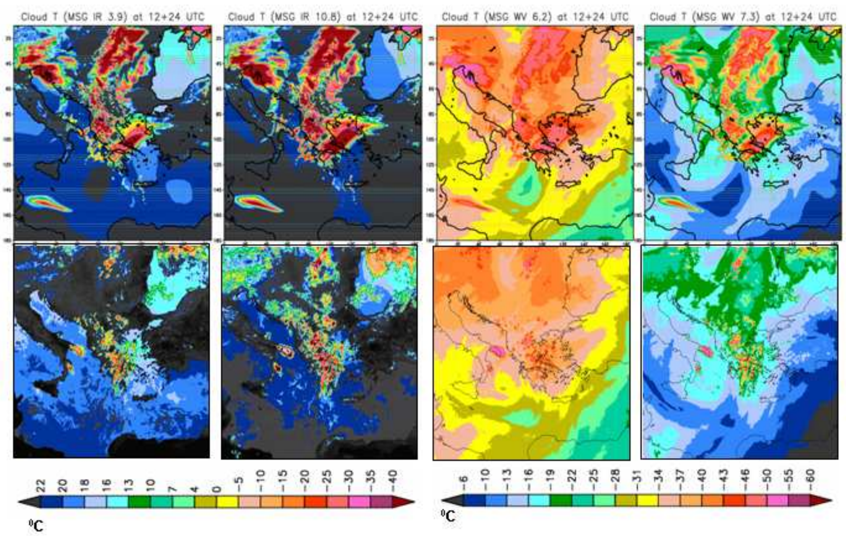

Figure 5: Artificial satellite images on August 31 2011 at 12 UTC from COSMO model (upper row) in reference to the corresponding MSG satellite figures (lower row) ©EUMETSAT. The first, second, third and fourth columns refer to 3.9 μm, 10.8 μm, 6.2 μm and 7.3 μm channels respectively.

3 Summary and Outlook

The possibility for direct comparison of cloud cover and synthetic satellite images of COSMO model with the corresponding remote sensing products is a valuable feature towards both the validation of the model but also for research purposes. In particular, the evaluation of different cloud schemes through the availability of these products (Refs. Avgoustoglou2011) is currently under progress.

References

[1] Reichert, B. K., C. Träger, and J. Asmus, 2004: Automatic Monitoring of NWP Fields Using Synthetic Satellite Images. EUMETSAT Meteorol. *Sat. Conf.*, EUMETSAT, Darmstadt, Germany, **371-376**.

[2] Reichert, B. K., C. Träger-Chatterjee, and J. Asmus, 2005: Using synthetic satellite images for automatic monitoring of NWP fields: operational applications. *EUMETSAT Meteorol. Sat. Conf.*, EUMETSAT, Darmstadt, Germany, **67-74**.

[3] Reichert, B. K., C. Träger-Chatterjee, and J. Asmus, 2006: How can synthetic satellite images from NWP models help in operational forecasting? *EUMETSAT Meteorol. Sat. Conf.*, EUMETSAT, Darmstadt, Germany, **72**.

[4] Avgoustoglou E., 2011: Investigation Of Different Parametrizations Of The Mixed Liquid-ice Sub-grid Statistical Cloud Scheme Over Greece. Presentation available at *www.cosmo-model.org/content/consortium/generalMeetings/general2011/wg3a.htm.*

Comparative Evaluation of High Resolution Numerical Weather Prediction Models COSMO-WRF

Bogdan Alexandru MACO, Mihaela BOGDAN, Amalia IRIZA,
Cosmin Dănuţ BARBU, Rodica Claudia DUMITRACHE

National Meteorological Administration
Sos. Bucuresti- Ploiesti, nr.97, Bucharest, Romania

1 Introduction

The COSMO-Model is a nonhydrostatic limited-area atmospheric prediction model, designed for both operational numerical weather prediction and various scientific applications on the $meso-\beta$ and $meso-\gamma$ scale. The COSMO-Model is based on the primitive thermo-hydrodynamical equations describing compressible flow in a moist atmosphere. Model equations are formulated in rotated geographical coordinates and a generalized terrain following height coordinate. A variety of physical processes are taken into account by parameterization schemes.

The purpose of this paper is to present the results of the comparative evaluation of the quality of high resolution weather forecasts from numerical weather prediction models COSMO - 2.8km (Consortium for Small Scale Modelling) and WRF - 3km (Weather Research and Forecast model).

The numerical weather prediction model COSMO - 2.8km is currently being run at the National Meteorological Administration once a day, at 00 UTC. WRF is a non-hidrostatic numerical weather prediction model developed by NCEP (National Centre for Environmental Prediction) in collaboration with the international meteorological comunity. In order to compare the performance of the two models, the WRF model was implemented at the 3km resolution and integrated with 00 UTC data for a test period. The integration domains of the two models cover the entire Romanian territory (COSMO-2.8km 361×291 grid points and WRF-3km 261×191 grid points, see figure 1).

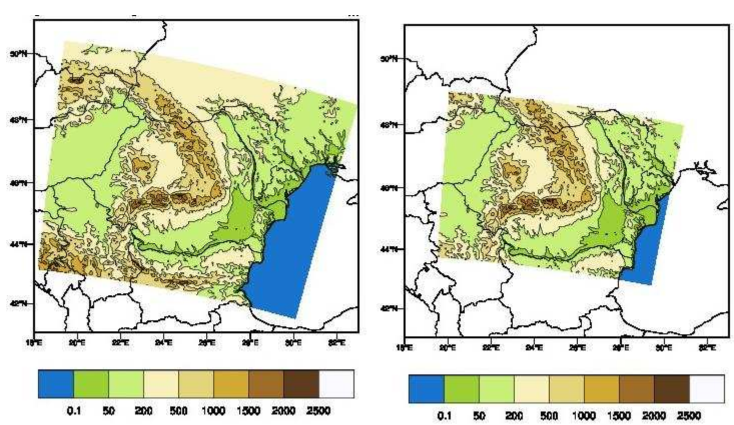

Figure 1: Model domains: COSMO-2.8km (left) and WRF-3km (right).

Both models were integrated for the test period with the same initial and boundary conditions from the output of the COSMO-7km model. In standard configuration, the WRF model uses initial and boundary conditions from the GFS global model (Global Forecast System). In order to use the output of the COSMO-7km model for the run of WRF model, a series of interpolation methods from rotated latitude / longitude grid into regular latitude / longitude grid were necessary. For these procedures, the post-processing software tool “Fieldextra” was used. “Fieldwxtra” is a generic tool to manipulate numerical weather prediction model data and gridded observations, developed by MeteoSwiss. Post-processing of the WRF-model output was made using the ARWpost software package.

The test period for which the numerical weather forecasts of the two models were compared is AUGUST 2011.

2 Parameters Evaluation

In order to point out the quality of the numerical weather prediction of the two high-resolution models, statistical scores were computed for different meteorological parameters:

- 2 m air temperature
- mean sea level pressure
- 10 m wind speed

The scores computed were based on forecast - observation differences, using nearest grid point method.

The first step of the evaluation consisted of computing mean error and mean squared error taking into account all synoptic stations in Romania. The second step of the analisys is represented by separating the Romanian meteorological stations in four categories (according to landform altitude):

- stations on the seaside of the Black Sea (7 stations)
- plain stations (88 stations with altitudes under 300 m)
- hillside stations (43 stations with altitudes between 300 m and 800 m)
- mountain stations (25 stations with altitudes over 800 m)

For each of these categories, the same scores were computed as in the previous stage.

For the numerical forecast of 2m temperature (figure 2), both models overestimate values of this parameter for the mountain stations. Moreover, the errors from the WRF-3km model forecast reach up to $4°C$, while the errors from the forecast of the COSMO-2.8km vary between $1°C - 2°C$. The situation differs for seaside stations. The COSMO-2.8km model underevaluates the values for this parameter, the error keeping between $-2°C$ and $0°C$, while the WRF-3km model overestimates these values, with errors of $0°C$ up to $3°C$. For hillside and plain stations, the models have opposite behaviour.

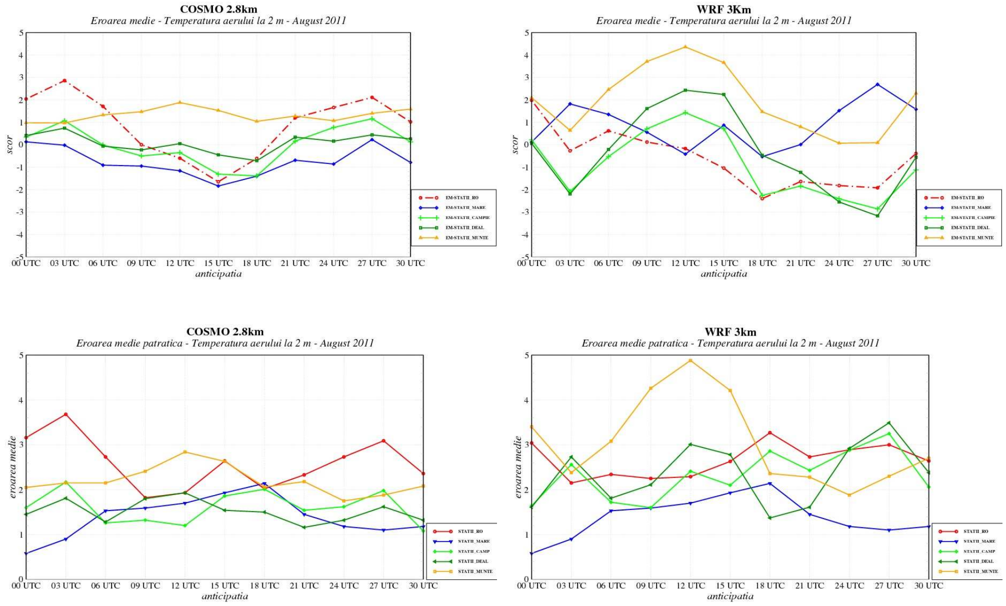

Figure 2: 2 m temperature BIAS score (first row) and RMSE (second row): COSMO-2.8km (left) and WRF-3km (right); seaside stations - blue, plain stations - light green, hillside stations - dark green, mountain stations - orange, all Romanian stations - red.

After comparing the forecast of the two models for mean sea level pressure for the test period, it can be stated that both the COSMO-2.8km model and the WRF-3km model have the same tendency, forecasted values being very close, with errors for both models mostly between -1 and 1 (figure 3).

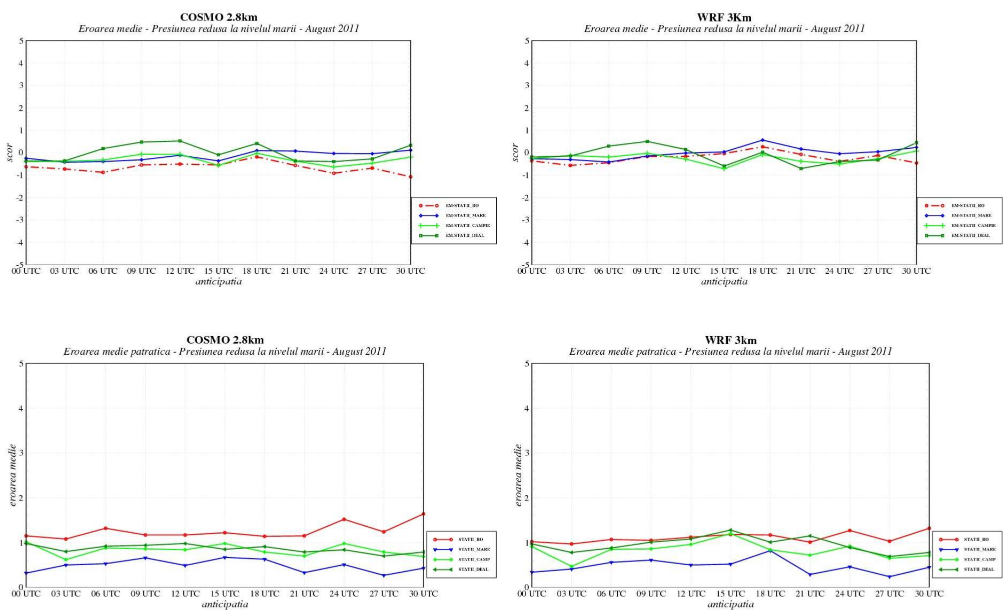

Figure 3: Mean sea level pressure BIAS score (first row) and RMSE (second row): COSMO-2.8km (left) and WRF-3km (right); seaside stations - blue, plain stations - light green, hillside stations - dark green, mountain stations - orange, all Romanian stations - red.

The last analised parameter in this stage of the evaluation is 10 m wind speed (figure 4). In forecasting this parameter for the time inteval 00 UTC - 06 UTC, both models show an important underestimation for mountain stations. In what concerns plain and hillside stations, the forecast errors for both models are between -1 and 1. The WRF-3km model overestimates forecasted values of this parameter for seaside stations, with errors up to 3. Except the initial period (until 06 UTC), the errors from the forecast of this parameter from COSMO-2.8km are very small for all types of stations.

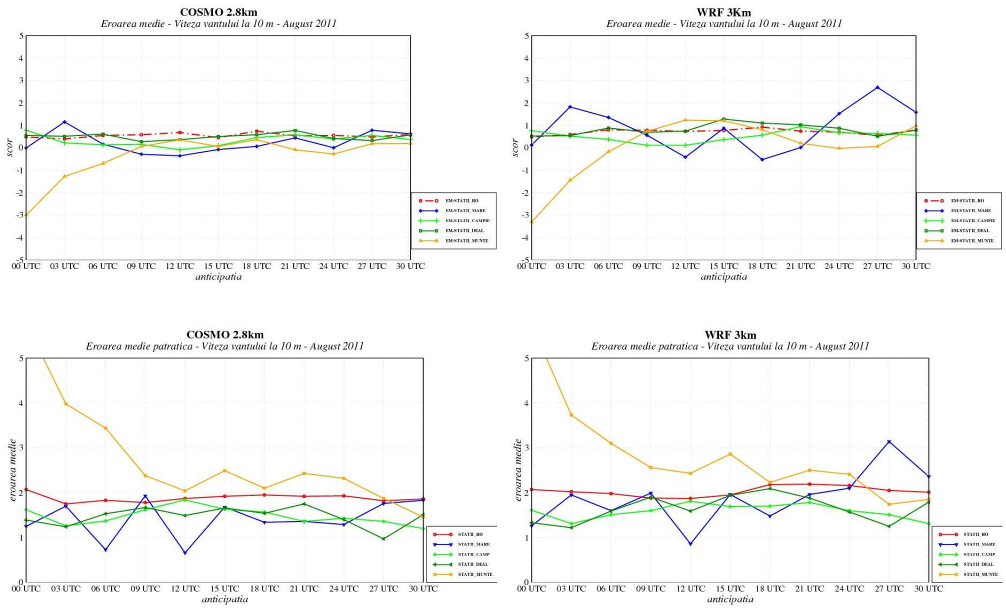

Figure 4: 10 m wind speed BIAS score (first row) and RMSE (second row): COSMO-2.8km (left) and WRF-3km (right); seaside stations - blue, plain stations - light green, hillside stations - dark green, mountain stations - orange, all Romanian stations - red.

3 Case Studies

Because August 2011 lacked precipitations over the are of Romania, two case studies are presented in order to analyse the performance of the two numerical weather prediction models in forecasting this parameter. The two selected case studies were:

- 17^{th} July 2011
- 17^{th} October 2011

In both cases heavy rainfall and strong wind were registered.

17^{th} July 2011

The Icelandic Low moved towards the Center and South of the continent along with a strong high-altitude cyclonic nucleus. Atmospheric circulation in the South-Eastern part of Europe was made on the South-Western, then Southern component, which allowed the inflow of a hot tropical airmass. During the day (06 UTC - 18 UTC), a short wave trough determined cold altitude airmass pulsations West of Romania. This led to an atmospheric instability and the formation of mesoscale structures which were active in the South part of Romania (figure 5).

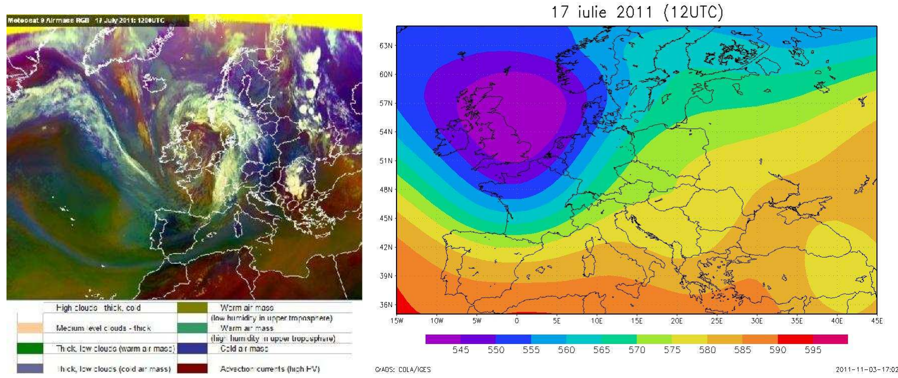

Figure 5: 17 July 2011 - 12 UTC: satellite image (left) and geopotential - 500hPa (right).

The maximum precipitations quantity registered in 24 hours was $127l/m^2$, in the South part of Romania (figure 6 - second row). The COSMO-2.8km model underestimated the quantity, forecasting between $50l/m^2$ and $100l/m^2$, while the WRF-3km model forecasted over $150l/m^2$, overestimating the values of this parameter and placed these quantities North of the area were they were actually registered. Both models overestimated the precipitation quantities in the North-East of Romania (COSMO-2.8km forecasted $25l/m^2$ and WRF-3km $150l/m^2$), where no precipitations were registered. Also, none of the models predicted the precipitations in the South-West region of our country (figure 6).

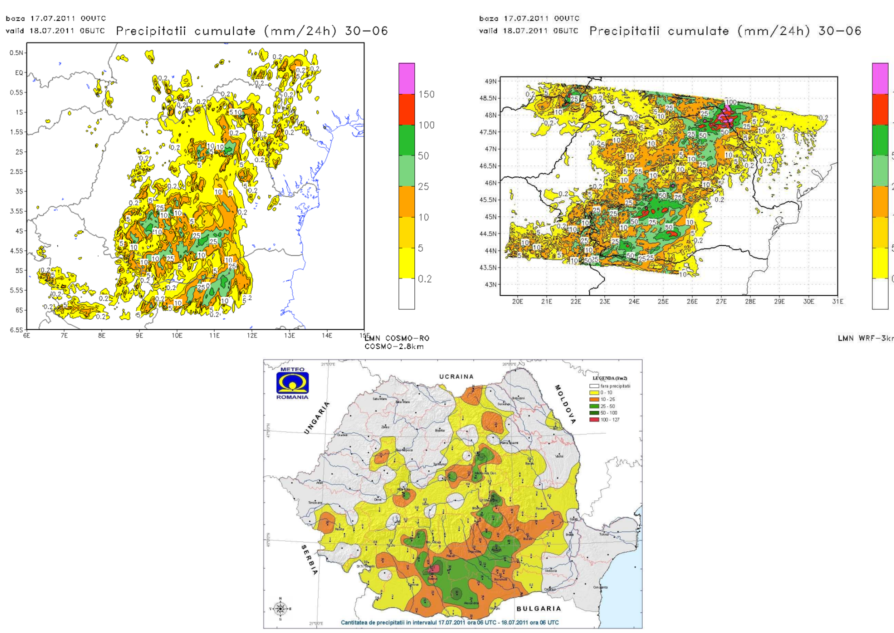

Figure 6: 17 July 2011 - 24 hours cumulated precipitations: COSMO-2.8km (left), WRF-3km (right), Observations (second row).

In order to compare the observations against the model forecast for the 10 m wind speed parameter, synoptic observations from meteorological stations in Romania were processed by interpolation in the grid of the model. Registered 10 m wind speed varied between $7m/s$ and $11m/s$, with wind gusts up to $16m/s$ at one meteorological station (figure 7 - second row). The COSMO-2.8km model predicted the wind speed values accurately and placed them correctly, forecasted values varying between $10m/s - 12m/s$ (figure 7). The WRF model run at the 3km spatial resolution did not forecast the wind intensifications.

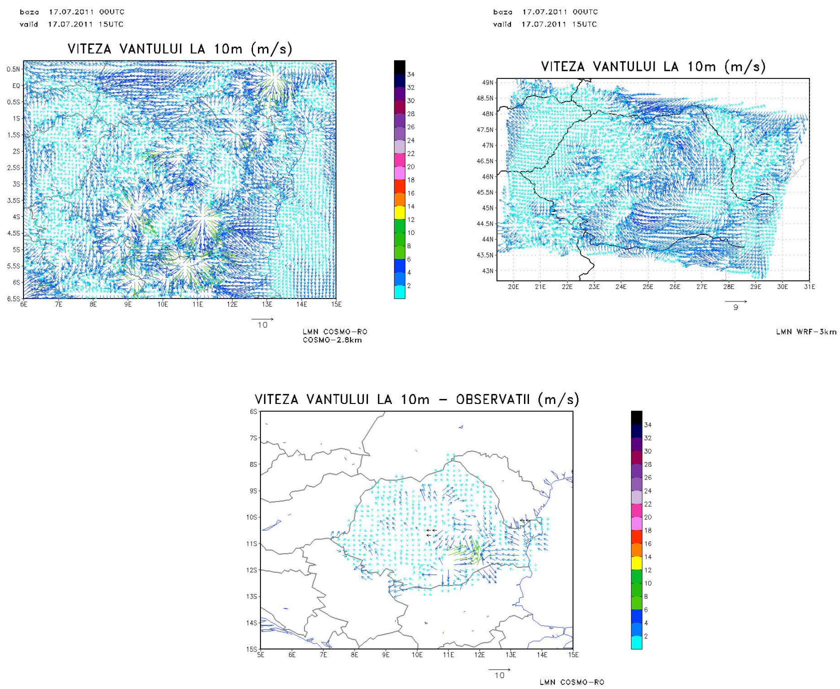

Figure 7: 17 July 2011 (00 UTC + 15 hours) - 10m wind speed: COSMO-2.8km (left), WRF-3km (right), Observations (second row).

17^{th} October 2011

The mediterranean originated cyclone evolved on a transbalcanic trajectory towards the South-Western region of the Black Sea. The warm surface of the sea contributed to the reactivation of this cyclone. In the altitude, a quasi-stationary low pressure altitude nucleus was observed, centered over the South of Romania and North of Bulgaria. The low pressure nucleus in the altitude was powered with cold air, which determined the intensification of the surface cyclone (figure 8). This atmospheric activity led to heavy rainfall in the South of the Romanian seaside and strong wind gusts that reached up to $70km/h$ - $80km/h$.

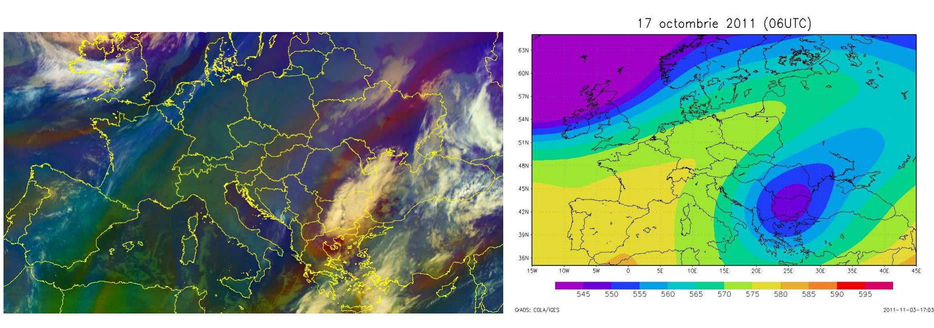

Figure 8: 17 October 2011 - 06 UTC: satellite image (left) and geopotential - 500hPa (right).

Both the COSMO-2.8km model and the WRF-3km model overestimated the precipitations in the South-East of Romania. In the South part of the Romanian seaside, up to $103l/m^2$ were registered in 24 hours (figure 9 - second row). These quantities were correctly estimated by both models (figure 9).

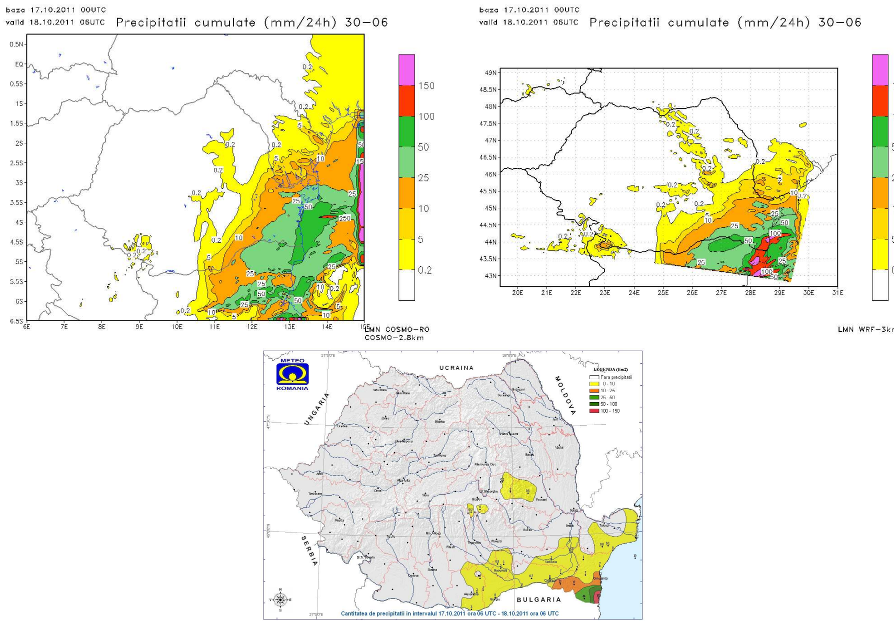

Figure 9: 17 October 2011 - 24 hours cumulated precipitations: COSMO-2.8km (left), WRF-3km (right), Observations (second row).

Concerning 10 m wind speed, observations values of this parameter were between $16m/s - 25m/s$. Both models forecasted correctly the strong wind in the are of the Romanian seaside (figure 10 - second row). The two models estimated values up to $24m/s$ for this parameter for the analysed period of time. Compared to the COSMO-2.8km model, the WRF-3km model overestimated 10 m wind speed values East of the seaside, forecasting values up to $18m/s$, while values from observations only reached up to $8m/s - 10m/s$ (figure 10).

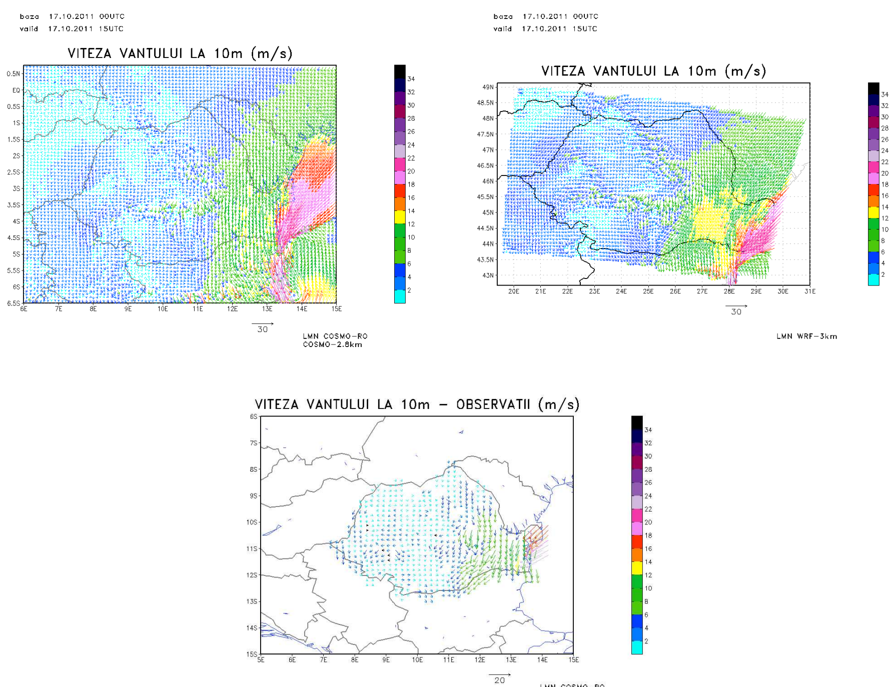

Figure 10: 17 October 2011 (00 UTC + 15 hours) - 10m wind speed: COSMO-2.8km (left), WRF-3km (right), Observations (second row).

4 Summary and Outlook

As a result of the analisys of computed statistical scores, it was decided that the results of the two high-resolution numerical weather prediction models are comparable. For the parameters selected in this evaluation, differences are noticeable depending on forecast times and altitude levels as follows.

For mean sea level pressure, both models offer correct estimates of this parameter, with small mean errors (between -1 and 1), with a tendency to underestimate values for most forecast times taken into account.

Forecasting 2 m temperature displays mostly an opposite behaviour of the two models (except for mountain stations). We also note that mean errors of the forecast from the WRF-3km model for this parameter are greater than the ones from the COSMO model run at the 2.8 km resolution.

Apart from underestimating 10 m wind speed values at mountain stations in the first forecast period, both models give a good forecast for this parameter, with small mean error values. For the WRF-3km forecast of 10 m wind speed, mean error values are slightly greater.

In the analysed cases with heavy rainfall, the high-resolution COSMO and WRF models estimate the precipitation area correctly, but the WRF-3km model has slightly higher over-estimates of this parameter.

References

[1] Stanski, H.R., and L.J. Wilson, W.R.Borrows, 1989: Survey of Common Verification Methods In Meteorology, WWW, *Technical Report*, No. **8**, WMO/TD.,No. 358.

[2] http://www.cawcr.gov.au/projects/verification/

[3] http://www.cosmo-model.org/content/model/documentation/core/default.htm

[4] http://www.mmm.ucar.edu/wrf-WRF-ARW

Selected COSMO-2 verification results over North-eastern Italian Veneto

A. M. Rossa[1], F. Domenichini[1], and B. Szintai[2]

[1] *Centro Meteorologico di Teolo, Via Marconi 55, I-35037 Teolo* [2] *Hungarian Meteorological Service, P.O. Box 38, H-1525 Budapest, Hungary*

1 Introduction

The regional meteorological service of the north-eastern Italian region Veneto, the Centro Meteorologico di Teolo (CMT) is part of the Regional Agency for Environmental Protection and Prevention of Veneto (ARPAV). The CMT run a dense network of automatic weather stations (AWS), counting some 200 over the entire territory, a good part of which are transmitted in near real time. Also, in 2005 a network of planetary boundary layer (PBL) profilers was installed, more precisely four passive microwave radiometers (MWR) and four SODARs [1]. These observations are used to verify the COSMO-2 over the Veneto territory, which can be thought of as a domain roughly split in four parts with distinct climatological characteristics, i.e. going from south to north (Fig. 1) there is the plain, the flat Po Valley portion of Veneto, which spans about two thirds of the area, the prealpine foothills and the prealpine chain, which is a significant barrier for southerly flows, the Val Belluna, a major Alpine valley just north of the prealpine chain, and finally the Dolomite mountains, a high and inner Alpine mountain area.

In this contribution selected verification results of the screen-level temperature, the temperature profiles and the PBL mixing height is given. The data set is described in section 2, the results in section 3, while some conclusions are summarized in the final section.

2 Data sets

Observations used for this analysis were acquired from the CMT AWS network, which totals roughly 200 stations, 109 of which have been used for verification of the screen-level temperature, and 22 for the ten-meter wind over the plain (Fig. 1). Verification of ten-meter wind is still in progress and will be presented in a contribution to follow, as for precipitation, for which the network consists of 161 real time tipping bucket gauges. Given the significantly differing climate zones in Veneto these stations have been grouped in the following sets:

- Dolomiti: 19 mountain stations located in the Dolomite mountains at altitudes between about 600 and 2200 m;
- Val Belluna: 8 stations located in the major Alpine valley Val Belluna just south of the Dolomite mountains and just north of the pre-alpine chain; the altitude of the stations varies between about 300 and 1400 m;
- Prealpi: 25 stations on the pre-alpine chain with altitudes between 100 and 1100 m;
- Plain: 57 stations on the Veneto plain with altitudes generally close to sea-level, occasionally up to about 100 m; for the screen-level wind verification 22 stations, equipped with anemometers at 10 m, i.e. excluding the stations with anemometers at 2 m for agrometeorological purposes;

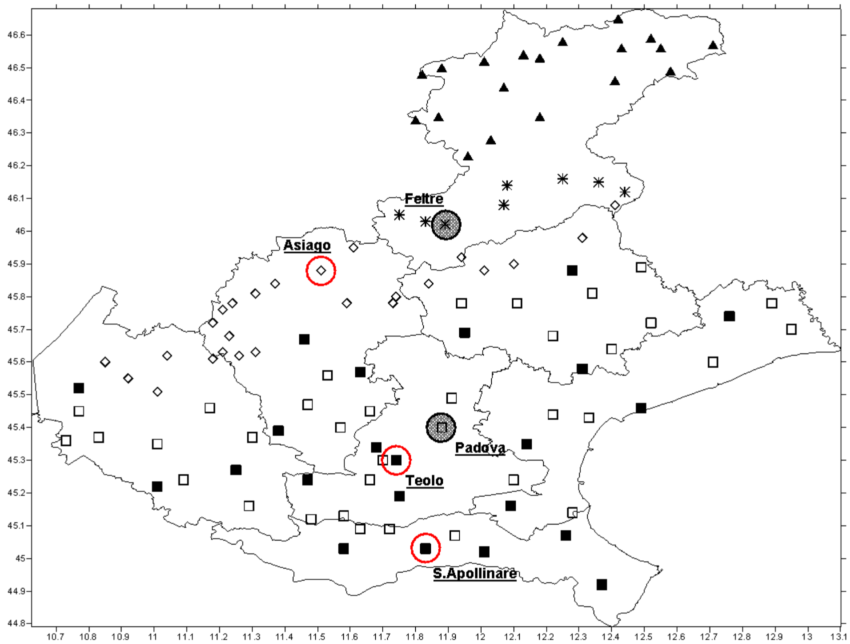

Figure 1: Layout of the ARPAV automatic surface station network desigend to cover the entire region Veneto (political contours). The stations were subdivided in four groups, i.e. high mountain stations (△), the major mountain valley Val Belluna (∗), the prealpine chain (⋄), and the plain (□). The filled squares denote surface stations in the plain with an anemometer at $10\,m$. Selected results for the three circled stations Asiago, Teolo, and S. Apollinare are shown in Fig.3. The two microwave radiometers used for this study are located in the plain in the city centre of Padova and in the Val Belluna in Feltre (shaded circles).

- vertical temperature profiles are verified for two sites, one in Padova, the other in the Val Belluna city of Feltre.

In addition, time series for a hot and cold multi-day period are analyzed for the stations Asiago, located on a high plateau, Teolo, located on the Euganean Hills emerging some $150\,m$ in the middle of the flat plain, and the plain station S. Apollinare.

The verification period comprises the two cold season months January and February 2010, and a the warm season spanning May to August 2011. The overall data availability for the verification period amounts to 97.4 %.

3 Results

Verification results of the screen-level temperature are shown in Fig. 2 for four groups of stations pertaining to the four distinctly different climatic zones of Veneto, i.e. the flat plain, the prealpine chain, the major Alpine valley Val Belluna, and the Alpine Dolomites (Fig. 1). The bias and standard deviation exhibit a clear diurnal cycle with the strongest warm bias during the night. Perhaps surprisingly, both statistical error measures are lowest for the Alpine Dolomites, a mixture of valley, slope and crest stations with bias values around $1.25\,K$ during the night and around or below $0.5\,K$ during the day, with two distinct minima mid morning and late afternoon. The corresponding values for the plain are about twice as high, in the early afternoon more than three times as high reaching $1.8\,K$, the maximum values attained during the night are as high as $3\,K$. For the night hours the two groups Prealpi and Val Belluna are in between the Dolomiti and the Plain groups, while during the daytime the Val Belluna stations show the largest bias reaching $2\,K$. This behaviour is reflected in

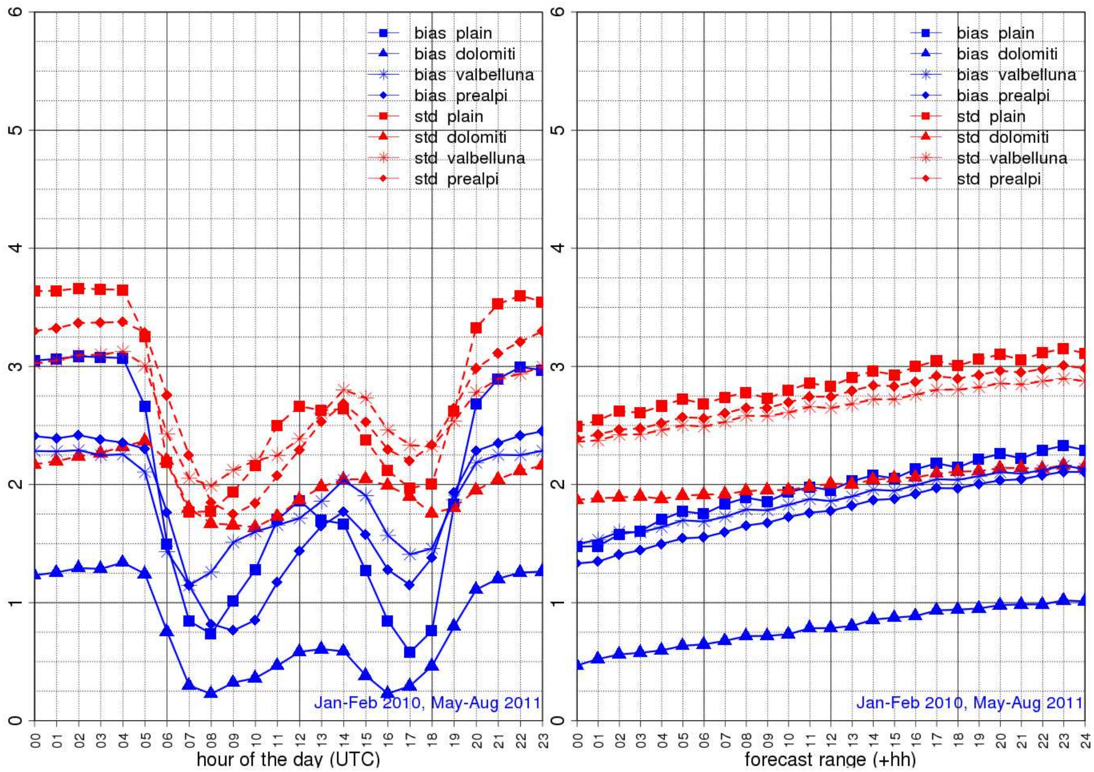

Figure 2: Bias (blue solid lines) and standard deviation (red dashed lines) for the four groups of ARPAV stations (Fig. 1), i.e. for the high mountain (△), the major mountain valley Val Belluna (∗), the prealpine chain (⋄), and the plain (□). The left panel shows the error in dependence on the hour of the day (UTC), while the right panel shows the dependence on the forecast range (+hh). The data set spans two cold and four warm season months.

the standard deviation. The structure of this diurnal cycle of the error is indicative for the model's underestimation of the diurnal temperature excursions, i.e. the warm bias in the minimum and maximum temperature, evidently larger for the night.

The dependence of the error from the forecast range shows a monotonour increase from $0.5\,K$ at $+01\,h$ to $1.0\,K$ at $+24\,h$ for the Dolomites and, again, significantly higher for the plain, where the bias ranges from $1.5\,K$ at $+01\,h$ to $2.3\,K$ at $+24\,h$. The prealpine and the Val Belluna stations have an error very similar to the plain.

Figure 3 illustrates one possible reason for the relatively large statistical forecast errors for three stations (see Fig. 1). Most notably, for the Asiago station (top panels), located on an elevated plain at around $1000\,masl$ on the prealpine chain, the COSMO-2 frequently severely underestimates the nocturnal cooling, sometimes by as much as $10\,K$, both for the heat wave and the cold period. This behaviour is even more pronounced for a nearby station (Marcesina), situated in a shallow basin, and for which the radiative cooling at night can be very significant (not shown). For the cold period the diurnal cycle is underestimated and the highs missed by several Kelvins, while for the heat wave these latter seem slightly overestimated. Note COSMO-2's different behaviour for 17 January, when the passage of an upper-level caused overcast skies over Veneto altered the conditions for the radiativ balance at the surface, the model underestimated the temperature during the night and for most of the day.

This same behaviour is found also for many of the Veneto plain stations as for example

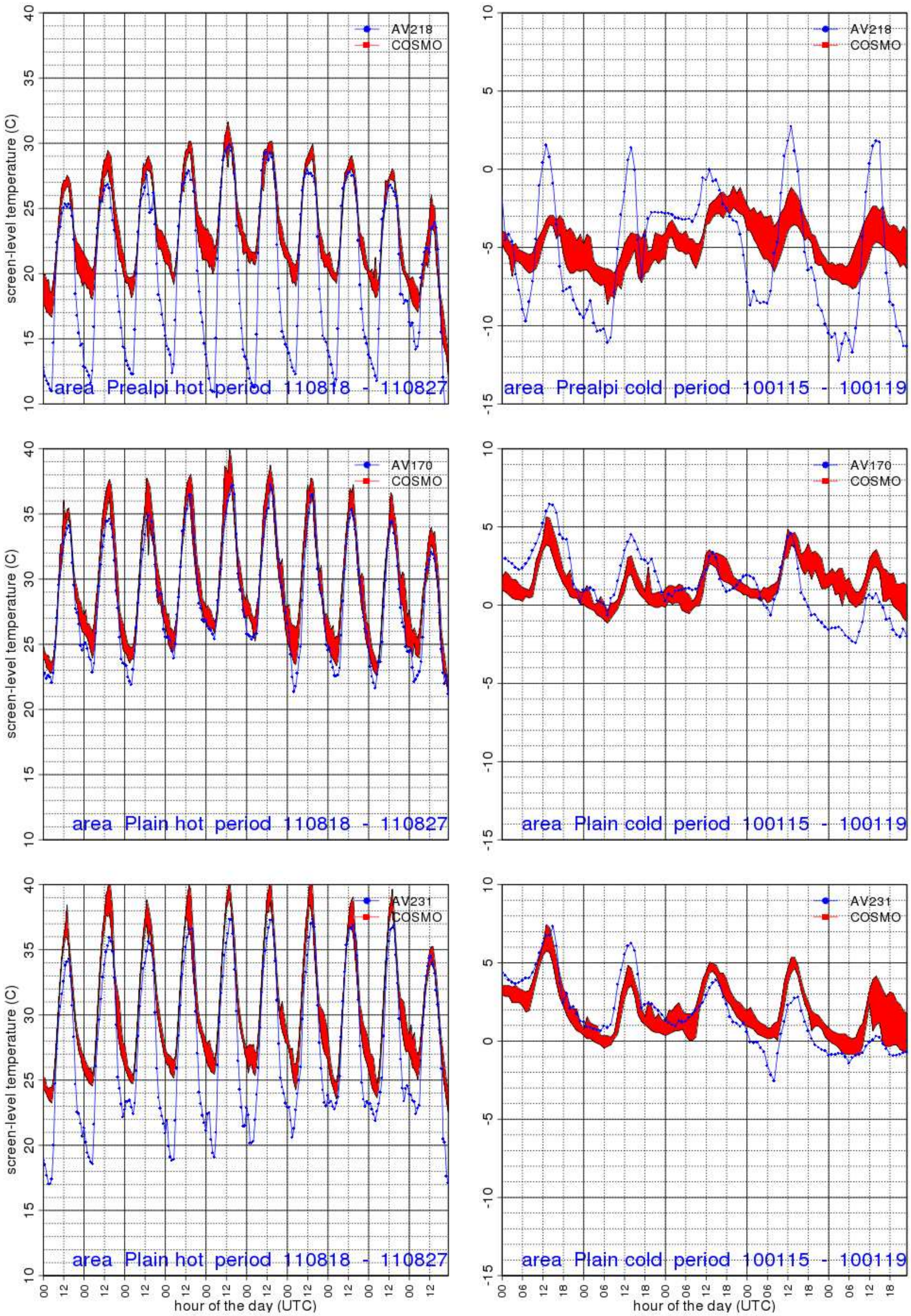

Figure 3: Time series of screen-level temperature observations (blue solid line) and COSMO-2 forecasts (red shading) for the three selected ARPA Veneto stations Asiago (AV218, top panels), Teolo (AV170, mid panels), and S. Apollinare (AV231 bottom panels, see Fig. 1). The left column panel are for the 18-28 August 2011 heatwave, while the right column panels for a period of cold and stable weather 15-19 January 2010. The red shaded area denotes the forecast range for each hour as spanned by the COSMO-2 time-lagged ensemble.

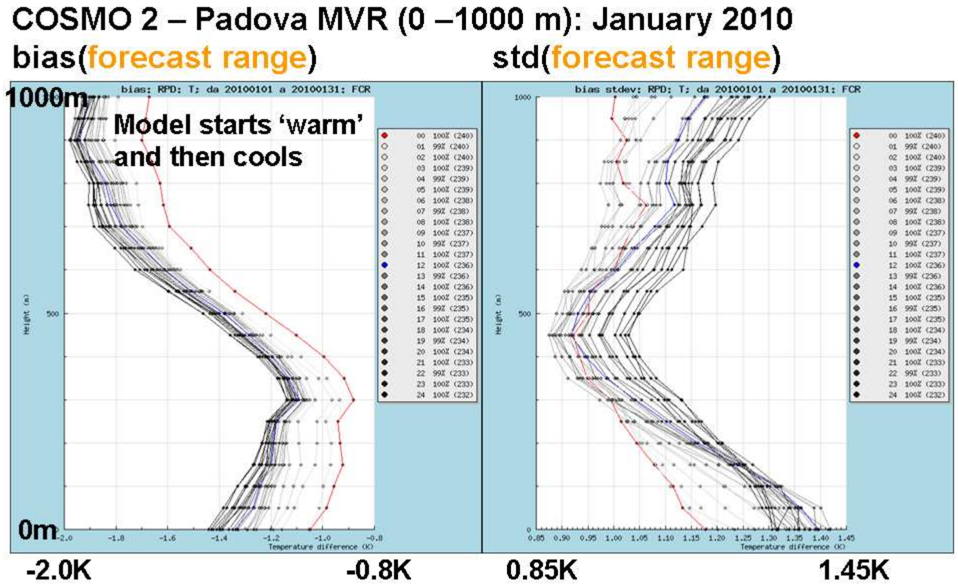

Figure 4: Bias and standard deviation of the COSMO-2 temperature profile against the MWR retrieval for the site Padova as a function of forecast range for the month of January 2010. The vertical axes denote the height above ground, the horizontal axes temperature. The darker the lines the longer the forecast range, while the +00 h line is in red and the +12 h line is in blue. The number in the legend denote percent of nominally available data and number of data pairs.

S. Apollinare (bottom panels), for many plain stations COSMO-2 exhibits a very similar behaviour, i.e. the a clear warm bias in the maximum temperature and an even larger one for the minimum temperature. It is interesting to note that the observed nocturnal cooling is not constant, in that it is more pronounced, for instance, for the nights of 21-24 August, while much less pronounced for the nights of 25-27 August 2011, where the sort of exponential decrease in the observed the temperature after sun down is interrupted. Closer inspection reveals that elevated values of the wind are likely to have induced mixing of the surface layer with the warmer residual layer and thus counteracted the radiative cooling. This process seems not to be reproduced in the model.

For the Teolo station (middle panels), located on the Euganean Hills at about 150 $masl$, COSMO-2 performs very well for the heat wave and decently during the cold period. There are a few stations in the Veneto plain which are located at about 100 $masl$ or a bit more, for which COSMO-2 performs similarly. Apparently, the these stations are not completely immersed in the nocturnal planetary boundary layer of the flat Po Valley, but are rather often part of a mixed or residual layer, which seems to be more adequately represented in the model.

For the station Venice, situated right at the coast in the historical city center, COSMO-2 clearly underestimates the diurnal temperature excursion, which is much smaller on the coast than in the inlands (not shown). Unlike for the other stations examined, for this location the the warm bias is larger for the maximum temperatures than for the minimum temperatures, probably because the for the latter the nocturnal cooling is mitigated by a combined effect of the urban heat island and the Venice Lagoon surrounding the city. The model performed better during the cold and stable period.

Figure 4 shows the verification result of the COSMO-2 temperature profile against the temperature profiles retrieved from the microwave radiometer (MWR) located in the city centre of Padova (Fig. 1) as a function of forecast range. The bias is negative on all levels ranging

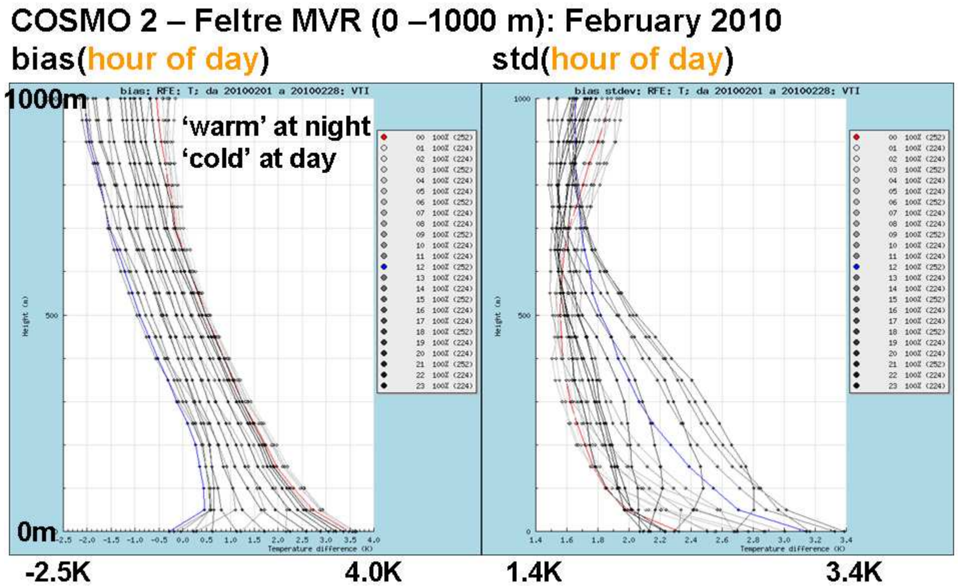

Figure 5: Bias and standard deviation of the COSMO-2 temperature profile against the MWR retrieval for the site Padova as a function of forecast range for the month of January 2010. The vertical axes denote the height above ground, the horizontal axes temperature. The darker the lines the later the hour, while the 00 UTC line is in red and the 12 UTC line is in blue. The number in the legend denote percent of nominally available data and number of data pairs.

from -0.9 to $-2\,K$ and might be related to the urban environment not represented in the model. One can appreciate that the bias is smallest at analysis time and tends to become more negative with increasing forecast range. Also, this progressive cooling of the lowermost part of the profile appears to be particularly rapid in the first few hours of the forecast. The standard deviation exhibits values between 0.9 and $1.4\,K$ where at analysis time larger values are found for levels between 250 and $900\,m$. Also, unlike the bias the standard deviation does not seem to increase monotonically with forecast range, an effect for which an explanation is yet to be found. The same behaviour can be seen for the prealpine valley station Feltre (not shown), except for the fact that the lowermost $250\,m$ of the profile shows a warm bias, at analysis time (red line) up to $350\,m$.

The behaviour of the COSMO-2 temperature profiles as a function of the hour of the day is shown in Fig.5 with values for the bias ranging from $+3.5$ to $-0.3\,K$ and values for the standard deviation ranging from 3.4 to $2.1\,K$ for the lower levels. At higher levels the bias decreases quite steadily and evenly for all hours by $3\,K$ at $1000\,m$ above ground. The standard deviation decreases with height and seems to be smallest for the morning hours. In summary, the model appears to have a tendency to be colder during the day and warmer during the night, visible also for the urban station Padova (not shown).

The mixing height verification is a more subtle issue as this variable is not directly measured, but needs to be estimated, or retrieved. There are several methods on how to do this [see 3, for a comprehensive review], the one used to retrieve the the mixing height from the observations is based on the PBL temperature and wind, and the surface energy balance [2]. The one used for the COSMO-2 is based on evaluating the Bulk Richardson number [5, 4].

Figure 6 shows the results of the COSMO-2 mixing height comparison against the estimats retrieved from observations as a function of the forecast range (left panel) and the hour of the day (right panel) for the month of January 2010. During the night the COSMO-2 tends to have a higher PBL than what is retrieved, i.e. a bias between 40 and $100\,m$, largest

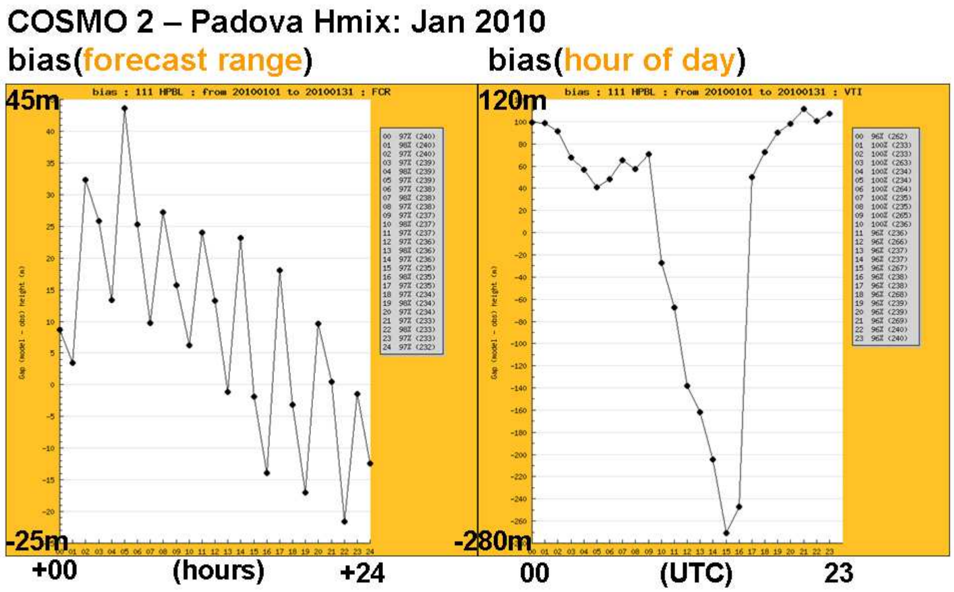

Figure 6: Bias of the COSMO-2 PBL mixing height against the retrieval for the site Padova as a function of the forecast range (left panel) and the hour of the day (right panel) for the month of January 2010. The vertical axes is in meter, the horizontal axis forecast range (+hh) and hour of the day (UTC), respectively. The number in the legend denote percent of nominally available data and number of data pairs.

around mid-night. This may be due to the fact that there is a minimum PBL height in the retrieval algorithm applied on the observations, which is set to $40\,m$ in the absence of mechanical turbulence. This happens in low wind conditions, which are very frequent in the Po Valley. On the other hand, there is a significant underestimation of the PBL height during the day, when starting at sun rise the positive bias changes to negative and peaks at almost $-300\,m$ mid to late afternoon. Results for February 2010 (not shown) show an even larger underestimation up to $-500\,m$.

4 Summary and Outlook

First verification results for the COSMO-2, run at MeteoSwiss, over the north-eastern Italian region Veneto are presented in terms of screen-level temperature, boundary layer temperature profiles and boundary layer mixing heights. The verification period spans two cold and four warm season months for the screen-level temperature, while the boundary layer verification was done for the two cold season months. The main results can be summarized as follows:

- COSMO-2 screen-level forecasts are affected by a clear warm bias for all station groups, with a pronounced diurnal cycle and maximum biases during the night, pinpointing insufficient nocturnal cooling;
- the overall error seems to be smaller for the Alpine stations and is largest for the plain stations, but also for stations on the high plateau of Asiago, where the nocturnal overestimation is most systematic, an effect that might be linked to the boundary layer evolution;
- bias and standard deviation increase monotonously with forecast range by about half a Kelvin;

- the dependence of the COSMO-2 cold season boundary layer temperature profile forecasts on the hour of the day shows a higher bias during the night and a lower bias during the day, i.e. relatively speaking too warm during the night and too cold during the day;

- the COSMO-2 cold season boundary layer temperature profile forecasts show a decreasing bias with forecast range, as if the model cools to quickly; this seems to contradict the screen-level temperature results and no explanation is proposed;

- comparison of COSMO-2 boundary layer mixing height with estimates retrieved from observations indicate a positive bias during the night and a significant negativ bias during the day, i.e. the COSMO-2 boundary layer seems to be too thick during the night and to shallow during the day.

Future verification work should include a more systematic verification of the boundary layer parameters, as well as ten-meter wind and precipitation over the Veneto. Also, more detailed studies of the COSMO-2 boundary layer over the plain portions of the domain would be helpful to understand the significant nocturnal warm bias of the model.

Acknowledgements The following individuals are thankfully acknowledged, i.e. M. E. Ferrario for providing the profiler data, M. Sansone for providing the mixing height estimates, and A. Della Valle for helping with the data processing.

References

[1] M. E. Ferrario and D. Pernigotti and A. M. Rossa and M. Sansone, 2006: Presentation and first assessment of a radiometer network in the Italian region Veneto. *Proceedings of 6th ICUC, International Conference on Urban Climate Gteborg, Sweden, 12 - 16 June 2006*, pp. **288-291**.

[2] Scire, J.S. and Robe, F.R. and Fernau, M.E. and Yamartino, R.J., 2000: A user's guide for the CALMET meteorological model. *Earth Tech*, USA.

[3] Seibert, P. and Beyrich, F. and Gryning, S.E. and Joffre, S. and Rasmussen, A. and Tercier, P., 2000: Review and intercomparison of operational methods for the determination of the mixing height. *Atmospheric environment*, volume 34, no. 7, pp. **1001-1027**, Elsevier.

[4] Szintai, B., 2010: Improving the Turbulence Coupling between High Resolution Numerical Weather Prediction Models and Lagrangian Particle Dispersion Models. *PhD Thesis*, no. 4827, pp. **142**, École Polytechnique Fédérale de Lausanne.

[5] Sørensen, JH and Rasmussen, A. and Svensmark, H., 1996: Forecast of atmospheric boundary-layer height utilised for ETEX real-time dispersion modelling. *Physics and Chemistry of the Earth*, volume 21, no. 4-5, pp. **435–439**, Elsevier.

Comparing COSMO-LEPS and COSMO-SREPS in the short-range.

Chiara Marsigli, Andrea Montani, Tiziana Paccagnella

ARPA-SIMC, Bologna, Italy

1 Introduction

Aiming at the development of an ensemble forecasting system for the short-range, the COSMO Consortium has chosen to explore the validity of a multi-model approach for providing initial and boundary conditions.

This approach has been tested in the experimental COSMO-SREPS system, which receives initial and boundary conditions by few state-of-the art operational deterministic runs. This ensemble has been compared with the operational COSMO-LEPS one, originally designed mainly for a 3-5 days forecast range, based on a dynamical downscaling of the global ensemble of ECMWF (EPS).

Both systems are made up by sixteen integrations of the COSMO model with 7 km horizontal mesh-size and they both benefit also of perturbations applied to the COSMO model itself.

In this paper, the impact of the two different perturbation strategies for boundaries on short-range forecast skill is assessed. This work is part of the COSMO Priority Project CONSENS, which aims at deciding which strategy is better to follow for short-range ensemble forecasting at the mesoscale. The impact of combining the two ensembles in different ways, for the aim of short-range forecasting, is also analysed. Results show that there is a positive effect in adding multi-model-driven members to the COSMO-LEPS ensemble, thus providing a hybrid solution to the problem.

2 Systems and methodology

COSMO-LEPS (COSMO Limited-area Ensemble Prediction System) is the mesoscale limited-area ensemble of the COSMO Consortium, developed by ARPA-SIMC, running since November 2002 (Montani et al., 2003). The ensemble is based on 16 runs of the COSMO model (Steppeler et al., 2003), the non-hydrostatic limited-area model of the COSMO Consortium.

The ensemble is generated as a downscaling of the global ECMWF EPS (Molteni et al., 2001; Marsigli et al., 2001). COSMO-LEPS is currently running at 7 km of horizontal resolution, on a domain covering central and southern Europe (Figure 1), with 40 levels in the vertical.

Being based on the EPS, COSMO-LEPS was designed for providing high resolution probabilistic forecast for the late-short to early-medium range, from day 3 to 5. The time window used for the cluster analysis (from +96 to +120 h) was selected to pursue this aim.

The experimental COSMO-SREPS system (Marsigli et al., 2009) receives initial and boundary conditions by a few state-of-the art operational deterministic runs (IFS, GME, GFS). The forecast range is 48 hours and resolution and domain are the same as for the COSMO-LEPS system.

Two different combinations of COSMO-LEPS and COSMO-SREPS have also been evaluated:

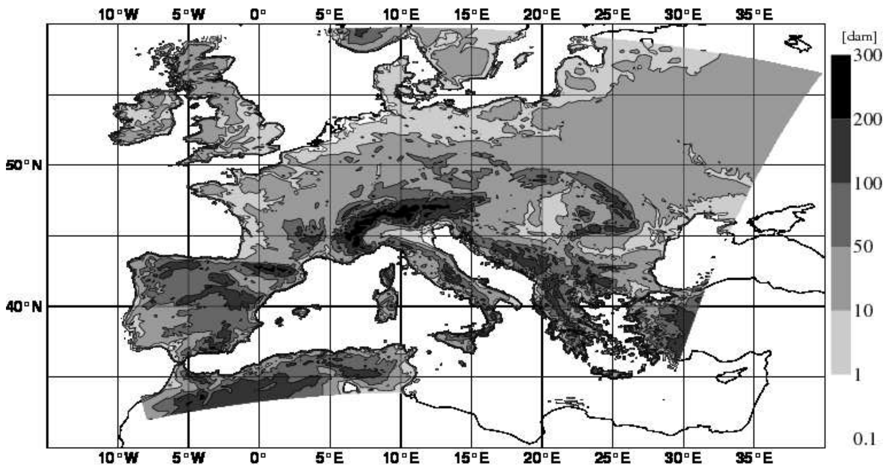

Figure 1: COSMO-LEPS and COSMO-SREPS orography, showing also the domain extension.

- a 20-member ensemble made up of the 16 COSMO-LEPS runs + 4 runs selected from COSMO-SREPS (here referred to as mix20)
- a 16-member ensemble made up by the first 12 COSMO-LEPS runs + 4 runs selected from COSMO-SREPS (here referred to as mix16)

The 4 runs selected from COSMO-SREPS are members 1, 6, 11, 16, which are nested on the 3 different global models (member 1 on IFS, member 6 on GME and member 11 on GFS) plus the control member (nested on IFS but with no physics perturbations). Hence, the maximum possible degree of diversity is allowed in these 4 COSMO-SREPS runs, to represent the impact of the multi-boundary approach.

The performance of the systems has been measured is terms of skill in PQPF (Probabilistic Quantitative Precipitation Forecasting). Verification of short-range precipitation was performed using a dense raingauge network covering northern Italy. This area includes the Italian part of the Alps and the Po Valley, enclosing in a small domain regions with different orography. The verification has been done following the “distributional method” (DIST), developed for the verification of COSMO-LEPS high-resolution precipitation forecasts (Marsigli et al., 2008). It consists of an upscaling of both forecasted and observed fields over boxes of selected size. The upscaling is performed by selecting some parameters of the precipitation distribution, providing a single forecast-observation pair for each box. In this work, only mean and maximum values of the distribution are evaluated and the size of the boxes is 0.5 x 0.5 degrees. If the number of observations in the box is below 5, the box is discarded.

Verification is performed over the winter season 2010/2011, specifically from 20 November 2010 to 28 February 2011.

3 Results

In Figure 2 the Brier Skill Score (left panel) and the area under the ROC Curve (right panel) are plotted as a function of the forecast range for the event “mean of the precipitation exceeding 1 mm/6h”. Both score measures are positively oriented. For a description of the scores, the reader is referred to Wilks (2006).

The COSMO-LEPS score is represented by the solid thick line, while the COSMO-SREPS

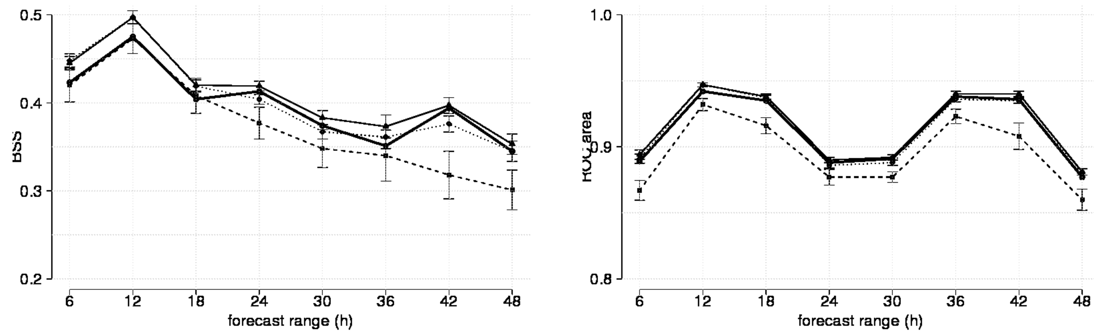

Figure 2: Brier Skill Score (left panel) and the area under the ROC Curve (right panel) are plotted as a function of the forecast range for the event "mean of the precipitation exceeding 1mm/6h". The solid thick line is for COSMO-LEPS, the dashed line is for COSMO-SREPS, the dotted line for mix16 and the solid thin line for mix20.

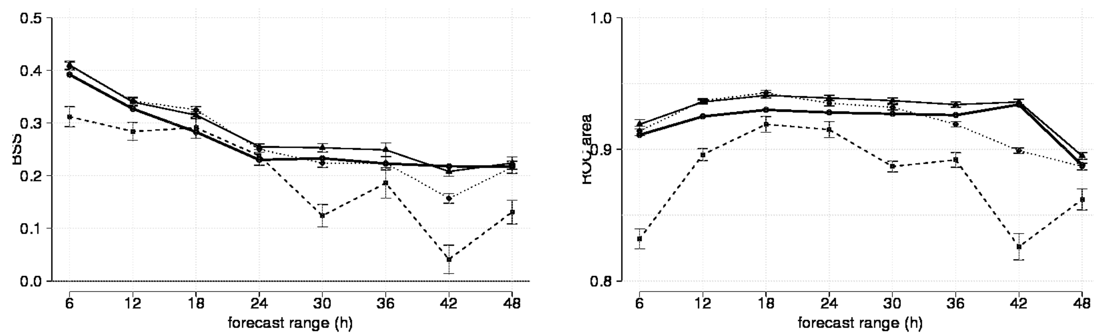

Figure 3: Same as in Figure 2 but for the event "mean of the precipitation exceeding 5mm/6h".

score is represented by the dashed line. The dotted and solid-thin lines refer to the mix16 and to the mix20 ensemble, respectively.

The first important finding is that COSMO-SREPS do not score better than COSMO-LEPS in the short-range. Both scores indicates a better performance of COSMO-LEPS for almost all the forecast ranges. The difference between the two ensembles is even more pronounced for a higher precipitation threshold, namely 5mm/6h, as shown in Figure 3.

The error bars around the red line are obtained with a testing, at 95% of confidence, that the COSMO-SREPS scores differ from the COSMO-LEPS one. The difference is always significant, except for a few forecast ranges for which the two BSS lines overlap.

An inspection of the scores in terms of maximum values of the precipitation distribution show the same behaviour, COSMO-LEPS performing better for (almost) all the forecast ranges (not shown).

The performance of the two combined systems, mix16 and mix20, are also shown in Figures 2 and 3. The mix16 ensemble can be regarded as a version of COSMO-LEPS where 4 members (randomly chosen) are substitute with 4 members driven by a small multi-model global ensemble (3 members + 1 control). Does the use of these 4 members in COSMO-LEPS provide additional skill with respect to using 4 more members driven by EPS?

For the lower threshold (Figure 2) the BSS of mix16 is significantly higher than that of COSMO-LEPS for the first 18 h, then it is comparable. In terms of ROC area, they are comparable from the beginning. For the higher threshold (Figure 3) mix 16 performs significantly better than COSMO-LEPS for the first 24 h in terms of both BSS and ROC area.

From an operational point of view it would be interesting also to quantify the impact to add these 4 multi-model-driven COSMO members to the operational COSMO-LEPS, thus increasing the ensemble size up to 20 members.

The mix20 ensemble performs better than COSMO-LEPS for almost the whole forecast range in terms of both BSS and ROC area for the higher precipitation threshold, and, to a lesser extent, also for the low precipitation threshold, but only in terms of BSS.

As a general result, there is a benefit in adding multi-model driven members for the first day of forecast and this holds even keeping fixed the number of ensemble members.

4 Summary and Outlook

A comparison has been presented between the performance for short-range QPF of two different ensembles based on the COSMO model.

COSMO-LEPS is driven by 16 selected members of the ECMWF EPS, while COSMO-SREPS is driven by 3 operational global model runs. Both initial and boundary conditions are provided by the driving runs. Both systems run at 7 km of horizontal resolution, on the same domain, and have perturbations in the physics parameters.

The main results are here listed:

- generally COSMO-LEPS outperforms COSMO-SREPS
- the multi-model approach for initial and boundary conditions proves valuable even if model with different qualities are used (not shown)
- combining the 16 COSMO-LEPS members with 4 COSMO-SREPS members this 20-member ensemble outperforms both systems
- combining 12 COSMO-LEPS members with 4 COSMO-SREPS members, this 16-member ensemble outperforms COSMO-LEPS for the first day (up to 18 - 30 h)

The multi-model in itself proved valuable, but the 3 IC-BCs perturbations available do not allow the COSMO-SREPS ensemble to get a performance better to a downscaling from a well constructed ensemble like the ECMWF EPS. A more detailed analysis will be presented as a Techical Report.

Acknowledgements: *This work was partially founded by the project MODMET3, supported by the Italian National Civil Protection. The authors wish to thank the COSMO Consortium and ECMWF for the possibility of running the two ensemble suites. We particularly thank Davide Cesari for the support in the ensemble implementation and Paolo Patruno for the technical support.*

References

[1] Marsigli, C., Montani, A., Nerozzi, F., Paccagnella, T., Tibaldi, S., Molteni, F., Buizza, R., 2001: A strategy for High–Resolution Ensemble Prediction. Part II: Limited–area experiments in four Alpine flood events. *Quarterly Journal of the Royal Meteorol. Soc.*, **127**, 2095-2115.

[2] Marsigli, C., Montani, A., Paccagnella, T., 2008: A spatial verification method applied to the evaluation of high-resolution ensemble forecasts. *Meteorological Applications*, **15**, 125-143.

[3] Marsigli, C., 2009: COSMO-SREPS Priority Project "Short Range Ensemble Prediction System (SREPS)": final report. *COSMO Technical Report*, No. **13**, available at http://www.cosmo-model.org/public/techReports.htm

[4] Molteni, F., Buizza, R., Marsigli, C., Montani, A., Nerozzi, F., Paccagnella, T., 2001: A strategy for High–Resolution Ensemble Prediction. Part I: Definition of Representative Members and Global Model Experiments. *Quarterly Journal of the Royal Meteorol. Soc.*, No. **127**, 2069-2094.

[5] Montani, A., Capaldo, M., Cesari, Marsigli, C., Modigliani, U., Nerozzi, F., Paccagnella, T. Patruno, P. and Tibaldi, S., 2003: Operational limited–area ensemble forecasts based on the Lokal Modell. *ECMWF Newsletter Summer 2003*, No. **98**, 2-7.

[6] Montani, A., Cesari, D., Marsigli, C. and Paccagnella, T., 2011: Seven years of activity in the field of mesoscale ensemble forecasting by the COSMO-LEPS system: main achievements and open challenges. *Tellus*, **63A**, 605624.

[7] Steppeler, J., Doms, G., Schattler, U., Bitzer, H.W., Gassmann, A., Damrath, U. and Gregoric, G.: Meso-gamma scale forecasts using the nonhydrostatic model LM. *Meteorology and Atmospheric Physics*, **82**, 75-96.

[8] Wilks, D. S., 2006: Statistical methods in the atmospheric sciences, 2nd Ed. *Academic Press*, New York, **627** pp.

List of COSMO Newsletters and Technical Reports

(available for download from the COSMO Website: www.cosmo-model.org)

COSMO Newsletters

No. 1: February 2001.

No. 2: February 2002.

No. 3: February 2003.

No. 4: February 2004.

No. 5: April 2005.

No. 6: July 2006; Proceedings from the COSMO General Meeting 2005.

No. 7: May 2008; Proceedings from the COSMO General Meeting 2006.

No. 8: August 2008; Proceedings from the COSMO General Meeting 2007.

No. 9: December 2008; Proceedings from the COSMO General Meeting 2008.

No.10: January 2010; Proceedings from the COSMO General Meeting 2009.

No.11: February 2011; Proceedings from the COSMO General Meeting 2010.

No.12: March 2012; Proceedings from the COSMO General Meeting 2011.

COSMO Technical Reports

No. 1: Dmitrii Mironov and Matthias Raschendorfer (2001):
Evaluation of Empirical Parameters of the New LM Surface-Layer Parameterization Scheme. Results from Numerical Experiments Including the Soil Moisture Analysis.

No. 2: Reinhold Schrodin and Erdmann Heise (2001):
The Multi-Layer Version of the DWD Soil Model TERRA_LM.

No. 3: Günther Doms (2001):
A Scheme for Monotonic Numerical Diffusion in the LM.

No. 4: Hans-Joachim Herzog, Ursula Schubert, Gerd Vogel, Adelheid Fiedler and Roswitha Kirchner (2002):
LLM ¯ the High-Resolving Nonhydrostatic Simulation Model in the DWD-Project LITFASS. Part I: Modelling Technique and Simulation Method.

No. 5: Jean-Marie Bettems (2002):
EUCOS Impact Study Using the Limited-Area Non-Hydrostatic NWP Model in Operational Use at MeteoSwiss.

No. 6: Heinz-Werner Bitzer and Jürgen Steppeler (2004):
Description of the Z-Coordinate Dynamical Core of LM.

No. 7: Hans-Joachim Herzog, Almut Gassmann (2005):
Lorenz- and Charney-Phillips vertical grid experimentation using a compressible nonhydrostatic toy-model relevant to the fast-mode part of the 'Lokal-Modell'

No. 8: Chiara Marsigli, Andrea Montani, Tiziana Paccagnella, Davide Sacchetti, André Walser, Marco Arpagaus, Thomas Schumann (2005):
Evaluation of the Performance of the COSMO-LEPS System

No. 9: Erdmann Heise, Bodo Ritter, Reinhold Schrodin (2006):
Operational Implementation of the Multilayer Soil Model

No. 10: M.D. Tsyrulnikov (2007):
Is the particle filtering approach appropriate for meso-scale data assimilation?

No. 11: Dmitrii V. Mironov (2008):
Parameterization of Lakes in Numerical Weather Prediction. Description of a Lake Model.

No. 12: Adriano Raspanti (2009):
Final report on priority project VERSUS (VERification System Unified Survey).

No. 13: Chiara Mirsigli (2009):
Final report on priority project SREPS (Short Range Ensemble Prediction System).

No. 14: Michael Baldauf (2009):
COSMO Priority Project "Further Developments of the Runge-Kutta Time Integration Scheme" (RK); Final Report.

No. 15: Silke Dierer (2009):
COSMO Priority Project "Further Developments of the Runge-Kutta Time Integration Scheme" (RK); Final Report.

No. 16: Pierre Eckert (2009):
COSMO Priority Project "INTERP"; Final Report.

No. 17: D. Leuenberger, M. Stoll, A. Roches (2010):
Description of some convective indices, implemented in the COSMO model.

No. 18: Daniel Leuenberger (2010):
Statistical Analysis of high-resolution COSMO Ensemble forecasts, in view of Data Assimilation.

No. 19: A. Montani, D. Cesari, C. Marsigli, T. Paccagnella (2010):
Seven years of activity in the field of mesoscale ensemble forecasting by the COSMO-LEPS system: main achievements and open challenges.